A Measurement of the Longitudinal-Transverse Interference Structure Function from the D(e,e'p)Reaction

by

Thomas Robert McIlvain

B. S., Psychology
University of Utah
1982

Submitted to the Department of Physics
in partial fulfillment of the requirements for the degree of

Doctor of Philosophy

at the

MASSACHUSETTS INSTITUTE OF TECHNOLOGY

June 1994

Signature of Author _____
Department of Physics
May 24, 1994

Certified by _____
Professor William Bertozzi
Thesis Supervisor

Accepted by _____
Professor George Koster
Chairman of the Graduate Committee

A Measurement of the Longitudinal-Transverse Interference Structure Function from the D(e,e'p)Reaction

by

Thomas Robert McIlvain

Submitted to the Department of Physics
on May 24, 1994, in partial fulfillment of the
requirements for the degree of
Doctor of Philosophy

Abstract

This thesis describes the results of a deuterium electrodisintegration experiment performed at the Bates Linear Accelerator Center. We scattered electrons from deuterium nuclei in a CD_2 target, detecting the scattered electron and the ejected proton in coincidence. By measuring the D(e,e'p)cross section at two different angles of proton emission, with fixed values of the energy transfer, $\omega \approx 109$ MeV, and momentum transfer, $q \approx 400$ MeV/c, we extracted the longitudinal-transverse interference structure function, R_{LT}. R_{LT} is one of the four structure functions that contribute to the unpolarized coincidence cross section. We performed the experiment in the Bates North Hall using the Energy Loss Spectrometer System (ELSSY) to detect electrons and the prototype Out-Of-Plane Spectrometer (OOPS) to detect protons. Electrons of incident energies 576 MeV were scattered at angles of 44^o. Protons were detected in non-parallel kinematics at angles of -64.7^o ($\theta_{pq} \approx 11^o$ 'right' of $\vec{q}$) and -42.9^o ($\theta_{pq} \approx 11^o$ 'left' of $\vec{q}$). In order to maximize the statistical precision of the measurements, the cross sections and the structure function are averaged over a region of 81 to 106 MeV/c in missing momentum, p_m.

We compared the data to several calculations done by H. Arenhoevel. The most interesting physics was seen in the observable A_ϕ, the left-right asymmetry or difference/sum of the cross sections. A_ϕ was the only measured observable with minimal theoretical uncertainty. Thus, the theory-data comparison using A_ϕ was the most telling. A_ϕ was measured with statistical and systematic uncertainties of 12.8% and 10.8%, respectively. At this level of precision, it was concluded that the data showed a preference for the Arenhoevel relativistic full calculation over his non-relativistic full calculation.

Thesis Supervisor: William Bertozzi
Title: Professor of Physics

Dedicated to my wife

Contents

Chapter 1

Introduction

It has been said that the Deuteron is to nuclear physics what the hydrogen atom is to atomic physics. Knowing the potential, both are two-body systems that can yield exact quantum mechanical solutions, at least in the non-relativistic domain. This is one reason that much effort has been invested in understanding the nucleon–nucleon interaction and subnuclear degrees of freedom by calculations and experiments done on the Deuteron.[1]

Though the measured cross section from such experiments can be a test of these calculations, a more detailed test of theory is the extraction of the many structure functions. The experiment described herein was one of the first to measure one or more of these Deuteron structure functions in the coincidence mode. It was the first in a program of electron-proton coincidence experiments on ^{2}H that will be performed using one or more of a new type of proton spectrometer designed to detect protons out of the electron scattering plane. The ultimate goal of the program is to measure each structure or coincidence response function individually at different values of missing momentum and momentum transfer. The fabrication of this spectrometer and several like it was necessary in order to measure all the structure functions, since there are some that require out-of-plane proton detection for their extraction.

This thesis describes the measurement of quasielastic electron scattering from ^{2}H at a momentum transfer of 400 MeV/c. We detected the scattered electron and the knocked-out

[1]The many-body problem (i.e. 3 or more) hinders such efforts with $A > 2$ nuclei, as it does the efforts to investigate the atomic states of $Z > 1$ atoms.

proton in coincidence. To obtain the structure function R_{LT} (the function associated with interference between responses of the nuclear current to the virtual photon's longitudinal and transverse polarizations), we measured the coincidence cross-section D(e,e'p) in the electron scattering plane on both sides of the momentum transfer $\vec{q}$ and at equal angles of proton emission relative to $\vec{q}$. We then took the difference of these two cross sections to get R_{LT}. In this first experiment, data were also taken to enable a separation of R_L and R_T (functions associated with nuclear responses to the longitudinal and transverse photon polarization, respectively) for ^{2}H, as well as to measure R_{LT} for ^{12}C for a range of missing energies.

This chapter summarizes previous progress in electron scattering as it pertains to this experiment, discusses a particular model of the Deuteron, and presents the motivation for performing the current study. Chapter 2 describes the experimental setup and the data acquisition. Chapter 3 details the data analysis. Chapter 4 compares our measurements with model calculations and puts forth conclusions.

1.1 Electron Scattering

Electron scattering consists of aiming a beam of electrons at a target and detecting the electrons that emerge at a particular angle with a particular energy. If only the electron is detected, the scattering is referred to as 'inclusive,' since all possible nuclear final states contribute to the cross section. If other particles are detected in coincidence with the electron, then the process is referred to as 'exclusive,' since only certain nuclear final states contribute to this multi-detector or 'coincidence' cross section. Electron scattering is a powerful tool for studying the nucleus for four main reasons:

1. The interaction is described by Quantum Electro-Dynamics (QED) which means the interaction is well understood and calculable. This is important since the nuclear electromagnetic current, J_μ, is not well understood. Probing with a well known interaction will give a cross section that can be directly related to J_μ, the object of our

investigation.

2. The interaction is relatively weak. This means that the interaction can take place anywhere in the nuclear volume instead of primarily on the nuclear surface as in hadron–nucleus scattering. The weakness of the interaction also reduces the importance of multi-step processes and, at least for light nuclei, allows the interaction to be treated in the one-photon exchange or First Born Approximation.

3. The three-momentum transfer, $\vec{q}$, and the energy loss, ω, of the virtual photon can be varied independently subject only to the restriction that the virtual photon be spacelike ($Q^2 = q^2 - \omega^2 \geq 0$, where Q is the virtual photon four-momentum).[2] This is different from real photon absorption where $q = \omega$. This freedom to vary $\vec{q}$ and ω separately allows us, for each ω, to map out the $\vec{q}$ dependence of the transition matrix elements and hence to determine the spatial distributions of the transition charge and current densities of the nucleus under study.

4. Finally, unlike real photons, virtual photons have both a transverse and a longitudinal polarization component. This means that both current and charge densities can be investigated with electron scattering. Only the transverse or 3–current density $J(\vec{q})$ contributes to the real photon absorption cross section.

There are two main difficulties inherent in electron scattering:

1. A high energy electron radiates in the target. This changes the cross-section and creates the radiative tail. A major problem in inclusive deep inelastic electron scattering is subtraction of the radiative tail coming from elastically and inelastically scattered electrons. In general, either data or theory must be corrected for this effect for valid comparison.

[2] I am using rationalized natural units where $\hbar = c = 1$. I am also using the metric g^{ν}_{μ} where $g^0_0 = -1, g^j_i = \delta_{ij}, (i,j \in \{1,2,3\})$ and $g^i_0 = g^0_i = 0$. Thus, $Q^2 = Q_\mu Q^\mu = q^2 - \omega^2 \geq 0$. In general, 4-vectors will be represented by capital letters and 3-vectors will be represented by small letters (the electron current j_μ is an exception to this rule). Thus Q is a four-vector, Q_μ is the μ^{th} component of that four-vector, $\vec{q}$ is the corresponding three-vector, and q is the magnitude of that three-vector, $q = \vec{q}$.

2. Since the electromagnetic interaction is weak, The cross-sections are small compared to hadron-hadron cross sections. This makes coincidence experiments more difficult to perform due to the greater beam times necessary and other experimental challenges.

For light nuclei ($Z\alpha 1$ where Z is the nuclear charge), electron scattering is well approximated by a one photon exchange (see figure 1.2). The initial and final electron four vectors are $K = (\epsilon, \vec{k})$ and $K' = (\epsilon', \vec{k}')$, and the four momentum transfer is $Q = (\omega, \vec{q}) = K - K'$. $\omega = \epsilon - \epsilon'$ is the energy transfer and $\vec{q} = \vec{k} - \vec{k}'$ is the three-momentum transfer.

In the first Born Approximation, the quasielastic inclusive cross-section (see section 1.2) can be written as

$$\frac{d^3\sigma}{dk' d\Omega_{k'}} = \frac{4\pi}{M_A}\sigma_M \left\{ \frac{Q^4}{q^4} S_L(q,\omega) + \left(\frac{1}{2}\frac{Q^2}{q^2} + \tan^2(\theta_e/2) \right) S_T(q,\omega) \right\} \tag{1.1}$$

where θ_e is the electron scattering angle and σ_M is the Mott cross-section: for scattering a spin$-\frac{1}{2}$ electron from a pointlike infinitely massive charge:

$$\sigma_M = \frac{\alpha^2 \cos^2(\theta_e/2)}{4\epsilon^2 \sin^4(\theta_e/2)} \tag{1.2}$$

S_L and S_T are the longitudinal and transverse response functions for inclusive scattering.

1.2 Exclusive Electron Scattering – (e,e'p)

In inclusive quasielastic electron scattering, shown as the second broad bump in figure 1.1, a nucleon is ejected from the nucleus but only the scattered electron is detected. As previously mentioned, this corresponds to summing over all possible nuclear final states; thus the name 'inclusive'.

In exclusive electron scattering, (e,e'p) , both the scattered electron and the knocked out proton are detected. This gives us more information on the nuclear final state and on the reaction mechanism involved. I will not discuss the details of inclusive electron scattering. For more information on this topic and for a more detailed discussion of the (e,e'p)scattering

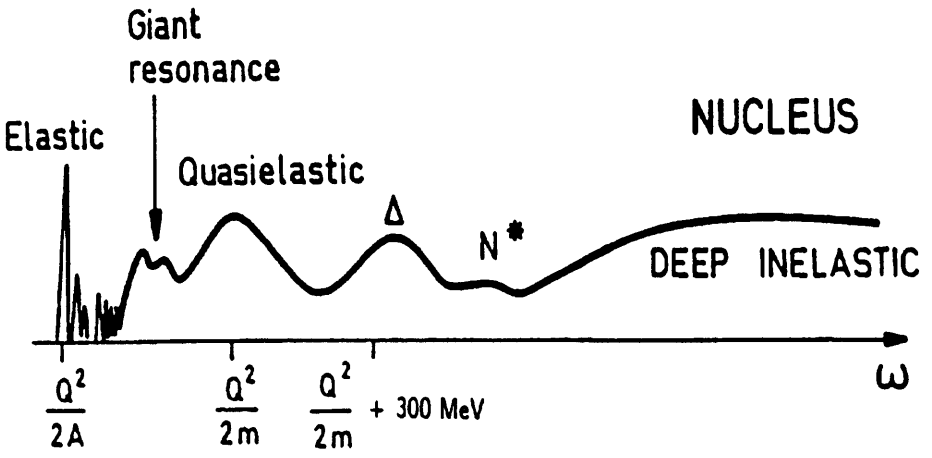

Figure 1-1: A typical inclusive electron scattering spectrum.

formalism, see [1].

1.2.1 Born Approximation

In the Born Approximation, the electron–nucleus interaction Hamiltonian for the diagram in figure 1.2 is [2]

$$\hat{H}_I = e \int \hat{J}_\mu(X)\, A^\mu(X)\, d^4X \ , \tag{1.3}$$

where $\hat{J}_\mu(X)$ is the nuclear electromagnetic current operator ($\hat{\rho}, \hat{\vec{J}}$ and $A^\mu(X)$ is the Möller potential of the electron. A_μ is determined by Maxwell's equations from j_μ, the electromagnetic current of the electron:

$$\left(\nabla^2 - \frac{\partial^2}{\partial t^2}\right) A_\mu(X) = -4\pi j_\mu(X) \ , \tag{1.4}$$

where, for plane wave electrons

$$j_\mu(X) = -ie\bar{u}_{\vec{k}_2} \gamma_\mu u_{\vec{k}_1} e^{iQ\cdot X} \ . \tag{1.5}$$

Electron spin indices have been suppressed for simplicity.

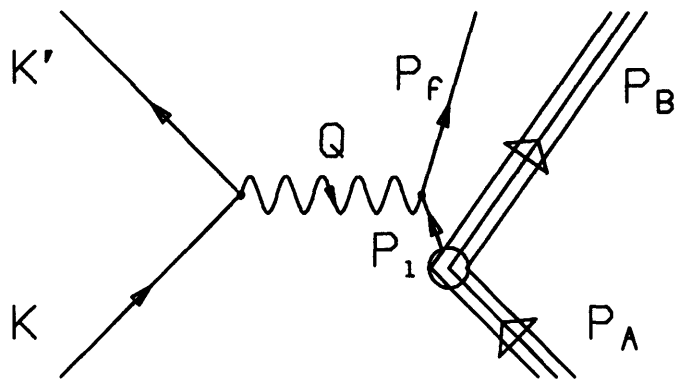

Figure 1-2: One photon exchange diagram for (e,e'p).

The cross-section is proportional to the contraction of the nuclear electromagnetic tensor $\tilde{W}^{\mu\nu}$ with the electron tensor $\eta^{\mu\nu}$.

$$\frac{d^6\sigma}{d\Omega_e d\Omega_p dK_F dp_F} \propto \widetilde{W}^{\mu\nu}\eta_{\mu\nu} \tag{1.6}$$

The electron tensor, $\eta_{\mu\nu}$, is proportional to $j_\mu j_\nu$ while the nuclear electromagnetic tensor $\tilde{W}^{\mu\nu}$ must be composed from the three available four-vectors, Q, P_A, and P_f. [3]

The most general form for $\tilde{W}^{\mu\nu}$ consistent with Lorentz covariance, parity and current conservation has four terms.[3] We can now expand relation 1.6 to obtain

$$\begin{aligned}\frac{d^6\sigma}{d\Omega_e d\Omega_p dE_m d\omega} &= \frac{\sigma_M}{\eta}\left[v_L R_L\left(\vec{q},\omega,\theta_{pq}E_m\right) + v_T R_T\left(\vec{q},\omega,\theta_{pq},E_m\right)\right.\\ &+ v_{LT}R_{LT}\left(\vec{q},\omega,\theta_{pq},E_m\right)\cos\left(\phi_{pq}\right)\\ &+ \left. v_{TT}R_{TT}\left(\vec{q},\omega,\theta_{pq},E_m\right)\cos\left(2\phi_{pq}\right)\right]\end{aligned} \tag{1.7}$$

where θ_{pq} is the angle the outgoing proton makes with respect to $\vec{q}$, ϕ_{pq} is the angle between the electron scattering plane and the $\vec{p}' - \vec{q}$ plane (see fig 1.3), and E_m is the missing energy, $E_m = \omega - T_p - T_B$.

The $v's$ are kinematic factors:

$$\begin{aligned} v_L &= \left(\frac{Q}{q}\right)^4 ,\\ v_T &= \frac{1}{2}\left(\frac{Q}{q}\right)^2 + \tan^2\left(\frac{\theta_e}{2}\right) ,\\ v_{LT} &= -\frac{1}{\sqrt{2}}\left(\frac{Q}{q}\right)^2\sqrt{\left(\frac{Q}{q}\right)^2 + \tan^2\left(\frac{\theta_e}{2}\right)} \end{aligned} \tag{1.8}$$

and

$$v_{TT} = -\frac{1}{2}\left(\frac{Q}{q}\right)^2$$

σ_M is the Mott cross section and η is the target recoil factor.

[3] A fifth term arises if the beam is polarized, and as many as 18 terms are present if the outgoing proton's polarization is measured. For the remainder of this thesis it will be assumed that beam and target are unpolarized.

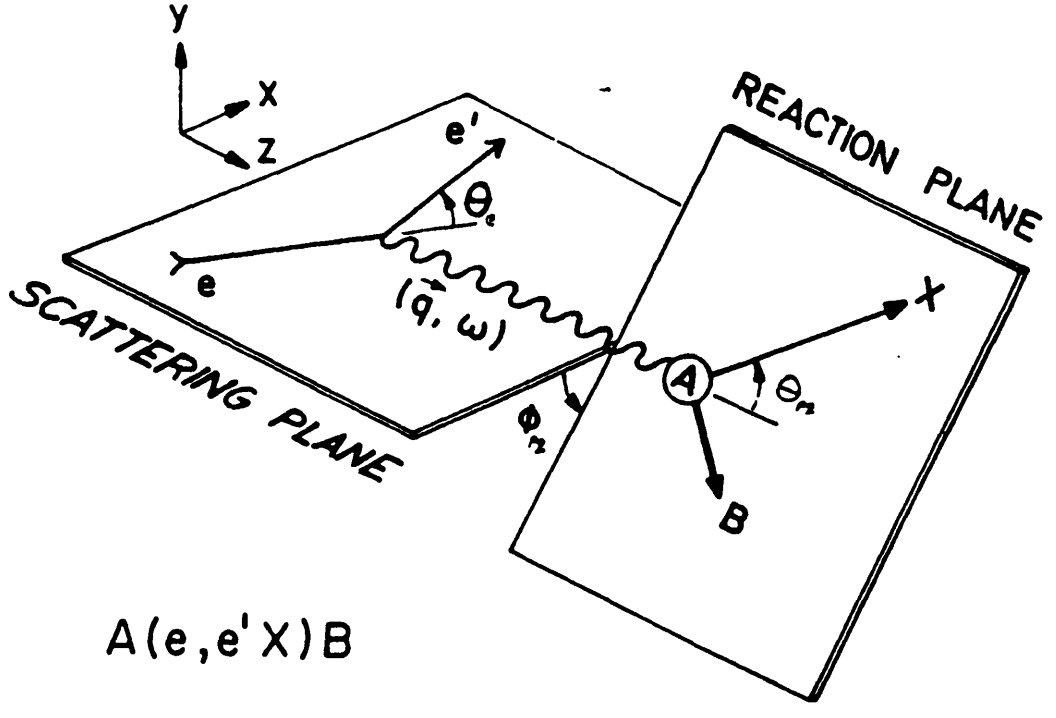

Figure 1-3: Kinematics of the (e,e'p)reaction. The figure is taken from [5].

R_L and R_T are, respectively, the structure functions associated with the longitudinal and transverse components of the nuclear current. R_{LT} is the function associated with interference between the longitudinal and transverse components of the nuclear current. R_{TT} is the function associated with interference between the two transverse components of the current.

DeForest [4] has shown that R_{LT} and R_{TT} are proportional to $\sin(\theta_{pq})$ and thus vanish in parallel kinematics, *ie:* when $\theta_{pq} = 0$. Thus, an R_L-R_T separation experiment is done in parallel kinematics to eliminate contributions of the interference structure functions from the measured cross sections. R_{LT} and R_{TT} also vanish for the case of inclusive electron scattering because of the integration over the outgoing proton.

The nuclear electromagnetic current, $J^\mu = (\rho, J^x, J^y, J^z)$, can be expressed in a spherical basis. Choosing the z-direction along $\vec{q}$, we can write

$$\begin{aligned} J_{fi}(0,\vec{q}) &\equiv J^z_{fi}(\vec{q}) \\ J_{fi}(\pm 1,\vec{q}) &\equiv \pm\frac{1}{\sqrt{2}}\left(J^x_{fi}(\vec{q})\right) \pm \left(J^y_{fi}(\vec{q})\right) \end{aligned} \tag{1.9}$$

where the the subscripts fi refer to the matrix elements evaluated between the initial and final states i and f. The continuity equation for the nuclear current

$$Q_\mu J^\mu = qJ(0,\vec{q}) - \omega\rho(\vec{q}) = 0 \tag{1.10}$$

allows the longitudinal component of the current to be replaced by the charge density. Using this notation, the response functions can be written in terms of the matrix elements of the current:

$$\begin{aligned} R_L &= |\rho_{fi}(\vec{q})|^2 = (q/\omega)^2 |J_{fi}(0,\vec{q})|^2 \\ R_T &= |J_{fi}(1,\vec{q})|^2 + |J_{fi}(-1,\vec{q})|^2 \\ R_{TT} &= 2\mathrm{Re}\{J_{fi}(1,\vec{q})^* J_{fi}(-1,\vec{q})\} \end{aligned} \tag{1.11}$$

and

$$
\begin{aligned}
R_{LT} &= -2\mathrm{Re}\left\{\rho_{fi}(\vec{q})^{*}\left(J_{fi}(1,\vec{q})-J_{fi}(-1,\vec{q})\right)\right\} \\
&= -2\left(q/\omega\right)\mathrm{Re}\left\{J_{fi}(0,\vec{q})^{*}\left(J_{fi}(1,\vec{q})-J_{fi}(-1,\vec{q})\right)\right\} \quad .
\end{aligned}
$$

These results are entirely general within the First Born Approximation. No assumptions other than Lorentz covariance, parity and current conservation have been made about the structure of J_{μ}.

1.2.2 The (e,e'p)Scattering Formalism – PWIA

Inclusive electron scattering indicates that scattering from single nucleons will be the dominant process in the quasielastic region at large energy and momentum transfers (fig. 1.1). The simplest process contributing to (e,e'p)in this region is shown in figure 1.1. This corresponds to the Plane Wave Impulse Approximation (PWIA). The underlying assumptions of PWIA are:

1) The virtual photon, Q, is absorbed on only one nucleon.

2) The nucleon does not interact again.

In order for the (e,e'p)cross-section to factorize, a third assumption, which is valid at high momentum transfer, is included:

3) The struck nucleon, not a spectator nucleon, is detected.

These assumptions are usually coupled with a fourth assumption concerning nuclear structure:

4) The nucleus can be described by an independent particle model.

Under these assumptions, Frullani and Mougey derive the following factorized form for the (e,e'p) cross-section:

$$
\frac{d^{6}\sigma}{d\omega dE_{m}d\Omega_{e}d\Omega_{p}} \sim \sigma_{ep}S\left(\vec{p}_{i},E_{m}\right) \tag{1.12}
$$

where σ_{ep} is the electron–proton cross-section, and $S(\vec{p}_i, E_m)$ is the spectral function. σ_{ep} describes the probability for scattering an electron from a proton where the proton is bound (and therefore off its mass-shell) in the initial state and unbound in the final state. This 'half-off-shell' cross-section cannot be directly measured. Theoretical prescriptions for calculating σ_{ep} exist. For example, there is the so-called 'CC1' prescription of [6].

The spectral function is the joint probability of knocking out a nucleon leaving the residual nucleus with momentum $\vec{p}_B = -\vec{p}_i$ and with excitation energy E_m with respect to the original nucleus. The spectral function is usually interpreted as the probability of finding a proton in the nucleus with initial momentum $\vec{p}_i$ and separation energy E_m. In PWIA S is a function only of $\vec{p}_i$ and E_m. Under assumption 4), the spectral function is diagonal:

$$S(\vec{p}_i, E_m) = \sum_\alpha n_\alpha(\vec{p}_i) f_\alpha(E_m) \tag{1.13}$$

where α are the relevant quantum numbers, $n_\alpha(\vec{p}_i)$ is the probability of finding a proton with quantum numbers α with momentum $\vec{p}_i$ and $f_\alpha(E_m)$ is the probability of finding a proton with quantum numbers α with separation energy E_m. In the Independent Particle Shell Model, the spectral function can be written as:

$$S(\vec{p}_i, E_m) = \sum_\alpha |\sigma_\alpha(\vec{p}_i)|^2 \delta(E_m - E_\alpha) \tag{1.14}$$

where α now refers to single particle orbitals, and $\phi_\alpha(\vec{p}_i)$ is the momentum wave function and E_α is the separation energy of orbital α.

1.2.3 The Special Case of Deuterium

Since Deuterium has only one bound state, with $E_b = 2.2$ Mev, we may write its spectral function as:

$$S_D(\vec{p}_i, E_m) = \rho(\vec{p}_i)\delta(E_m - E_b) \tag{1.15}$$

Using equations 1.12 and 1.15, we can then integrate over E_m to get an expression for the PWIA coincidence cross section involving only a momentum density.

$$\frac{d^5\sigma}{d\omega d\Omega_e d\Omega_p} \sim \rho(\vec{p}_i) \tag{1.16}$$

So we see that, assuming PWIA, we can determine the momentum distribution of Deuterium directly with an (e,e'p)measurement.

Likewise, integrating eq. 1.7 over E_m, we can write the general cross section as

$$\begin{aligned} \frac{d^5\sigma}{d\Omega_e d\Omega_p d\omega} &= \frac{\sigma_M}{\eta}\left[v_L R_L(\vec{q},\omega,\theta_{pq}) + v_T R_T(\vec{q},\omega,\theta_{pq})\right. \\ &+ v_{LT} R_{LT}(\vec{q},\omega,\theta_{pq})\cos(\phi_{pq}) \\ &+ \left. V_{TT} R_{TT}(\vec{q},\omega,\theta_{pq})\cos(2\phi_{pq})\right] \end{aligned} \tag{1.17}$$

This then is our four structure function expression for Deuterium. We notice that the structure functions now depend on three kinematic variables instead of four, since our missing energy is known exactly and is single valued. We may also choose to have the structure functions depend on the missing proton momentum $\vec{p}_m = \vec{p}_f - \vec{q}$ instead of on θ_{pq}, since the former is determined when $\vec{q}$, ω, θ_{pq}, and E_m are known.

1.2.4 Corrections to PWIA

PWIA is a good approximation in the quasielastic region. However, as one gets further away from this region in energy and momentum transfer, PWIA becomes less reliable, and corrections to it become more important. These corrections are diagrammed in figures 1.5-1.8.[4] There are four important corrections that need to be considered.[5]

[4]The diagrams are meant to be illustrative of the processes mentioned and not necessarily to be calculable in QED (i.e. figure 1.6).

[5]I will begin to employ convenient abbreviations extensively from this point on. I'll initially put the abbreviation in parentheses next to its description, and will refer to the process with its abbreviation thereafter. Meson exchange currents will be MEC and etc.

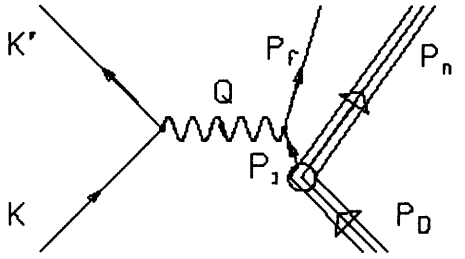

Figure 1-4: Plane wave impulse approximation (PWIA).

1. The exchange or PWIA e–n scattering (figure 1.5). Here we consider the process of PWIA interaction with the neutron followed by detection of the knocked out proton. Remember that we assume same particle detected as knocked out in PWIA (postulate 3 of section 1.2.2). We expect this process to be of small magnitude relative to PWIA e–p scattering due to the small probability of finding a proton in the Deuteron having initial momentum of several hundred MeV, which is what we set our proton spectrometer to see.[6]

2. The final state interaction (FSI) of figure 1.6. Here, the proton interacts with the neutron after absorbing the virtual photon, thus violating postulate 2 of section 1.2.2.

3. The Meson exchange current corrections (MEC), shown in figure 1.7, may also be important. However, MEC is not expected to contribute greatly to the cross section at the quasielastic peak, since this is the region where one-body processes are expected to dominate.

[6]Note that this process implies that, for the detected proton, $p_f = p_i$.

4. Finally, a process related to MEC is the isobar configuration (IC), shown in figure 1.8. Here the photon-hadron vertex contains a Δ form factor or other nucleon excited state. The process may involve a nucleon-isobar transition, or may involve two nucleon isobars in the ground state (one isobar is not possible in a $T = 0$ state, the Deuteron's total isospin in its ground state).

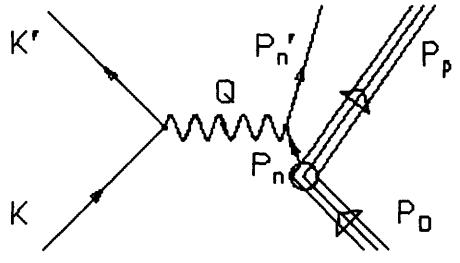

Figure 1-5: PWIA scattering off the neutron.

1.3 Calculations

To connect the cross section with a Deuteron model one must solve for the T-matrix. There are two interactions in the problem, the electron–nucleus interaction previously introduced and the neutron–proton interaction. If one thinks of the problem in terms of perturbation theory, then the transition or perturbing hamiltonian is the electromagnetic one. It then follows that T–matrix is related to J^μ via:

$$\langle f \,|\, \mathbf{T} \,|\, i \rangle \sim \langle f \,|\, J^\mu \,|\, i \rangle \tag{1.18}$$

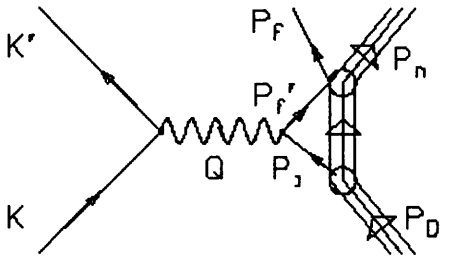

Figure 1-6: Final state interaction (FSI).

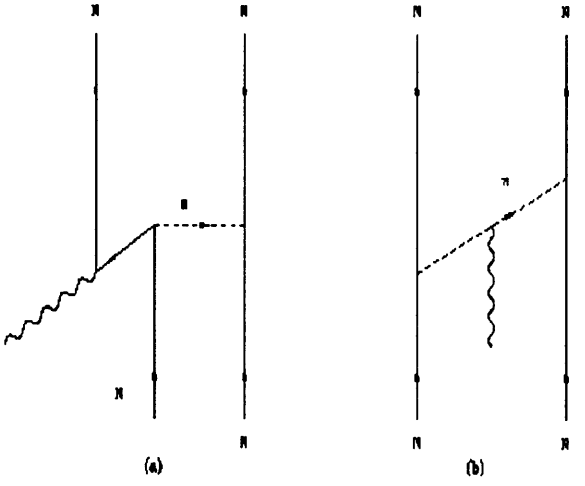

Figure 1-7: Meson exchange processes (MEC). N stands for either neutron or proton.

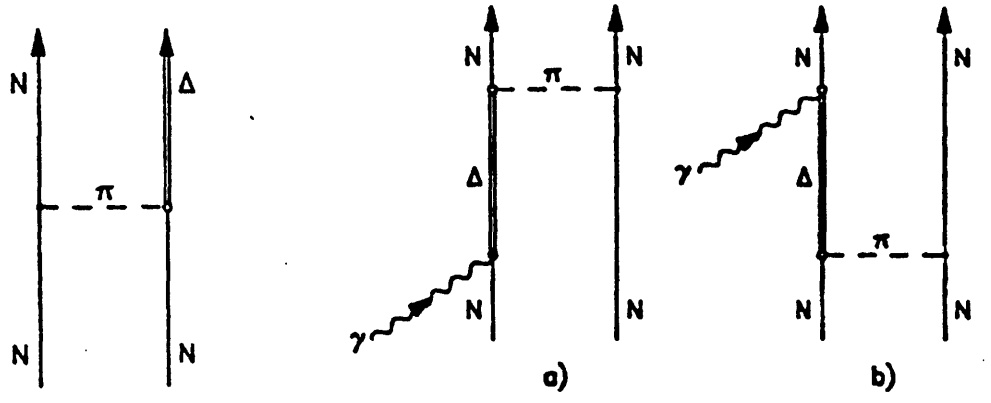

Figure 1-8: Isobar currents (IC).

So far, There have been four kinds of approaches for finding the T–matrix:

1. non–relativistic approaches with correct final state interaction and sometimes with inclusion of lowest relativistic correction [7], [8].

2. diagrammatic approaches with consideration of a selected class of Feynman diagrams where the final state interaction is treated only approximately [9].

3. covariant approaches using dispersion relations but inclusion of again only a limited number of diagrams, supposedly the most important ones [10].

4. a complete covariant approach where the Bethe-Salpeter equation is solved [11]

Fabian and Arenhoevel take the first approach, which I will now discuss.

1.3.1 The Treatment of Fabian and Arenhoevel

Using relativistic kinematics, these authors solve the Schroedinger equation and include final state interactions using a phenomenological Deuteron n–p potential such as the Paris, Reid soft core, or de Tourreil-Sprung potential.

This 'normal' theory (N), as they call it, can then have corrections added to it that include meson exchange currents (MEC) and isobar configurations (IC) to get their 'total' theory (T=N+MEC+IC). More will be said about the normal theory later in this section.

Since Fabian and Arenhoevel solve the Schroedinger equation for their results, their theory is referred to as 'non–relativistic'. Recently [12] relativistic corrections have been made to the nucleon charge and current densities in the normal theory to obtain what I will call the 'total relativistic' theory (TR=NRC+MEC+IC). As we will see, the relativistic corrections (RC) are the most significant of the above processes for determination of R_{LT} in the quasielastic region.

The Normal Theory

Here, Fabian and Arenhoevel (FA for short) obtain the Deuteron initial wave function $|i\rangle$ by solving the Schroedinger equation numerically in the center of mass frame up to an n–p

separation of $r_d = 10$ fermi. They use the asymptotic wave functions thereafter. They use the Paris potential for the n–p interaction and obtain the expected s-wave for the ground state.[7] The final n–p wave function is a partial wave expansion:

$$|\, i\,\rangle = |m_d\rangle = \sum_{nls} |\, n;(ls)\; 1m_d\rangle \quad ,$$

$$|\, f\,\rangle = |\, sm_s\,\rangle = \frac{1}{\sqrt{2\pi k^{\text{c.m.}}}} \sum_{njl\lambda} \sqrt{2l+1}\,(l0sm_s|\,(ls)\,jm_s) \exp\left(i\delta^j_\lambda\right) U^j_{ls\lambda}\,|\, n;\lambda jm_s\rangle \quad , \quad (1.19)$$

where

$$|\, 1;\lambda jm_s\rangle = \sum_{l's'} U^j_{l's'\lambda}\,|\, 1;(l's')\,jm_s\Big\rangle \quad ,$$

$$|\, n;\lambda jm_s\rangle = \sum_{l's'} |\, n;\lambda(l's')jm_s\rangle \quad . \qquad \text{for } n > 1 \; . \quad (1.20)$$

and the Blatt–Biedenharn convention is used for the final state partial wave expansion. $\vec{k}$ is the relative two–nucleon momentum. [13]. n enumerates the possible two-nucleon intrinsic configurations. $n = 1$ refers to the normal two–nucleon state while $n > 1$ refers to excited isobar configurations.

FA use one–body non-relativistic current densities that include the nucleon form factors and assume 'on–shell' form factors for the two nucleons:

$$\rho(q) = G_E(q) \quad ,$$

$$\vec{\mathrm{j}}(\vec{\mathrm{q}}) = \frac{1}{2M}\left(G_E\vec{\mathrm{P}} + iG_M\sigma \times \vec{\mathrm{q}}\right) \quad . \quad (1.21)$$

$$G_{E/M} = G^s_{E/M} + \tau_3 G^v_{E/M} \quad ,$$

$$\vec{\mathrm{P}} = \vec{\mathrm{p}}_i + \vec{\mathrm{p}}_f, \qquad \vec{\mathrm{q}} = \vec{\mathrm{p}}_f - \vec{\mathrm{p}}_i \quad , \quad (1.22)$$

[7] since the parameters of the Paris potential are determined from measurements, the small d-state component of the ground state is also present in the initial state

They then solve for the T–matrix of the disintegration process: $\gamma + d \Rightarrow p + n$

$$\begin{aligned} T_{sm_s,\mu m_d} &= \langle sm_s | \, T \, | \mu m_d \rangle \\ &= -(2\pi)^{-\frac{3}{2}} \sqrt{\frac{kM}{4\pi}} \left\langle sm_s \, | \, \hat{J}_\mu(\mathbf{q}) \, | m_d \right\rangle \ . \end{aligned} \tag{1.23}$$

which can be written as:

$$T_{sm_s,\mu m_d} = \exp\left(i\mu\sigma_{\rm np}^{\rm c.m.}\right) t_{sm_s,\mu m_d}\left(\theta_{\rm np}^{\rm c.m.}\right) \ , \tag{1.24}$$

They then expand the nuclear current density J^μ in terms of Coulomb and transverse electric and magnetic multipoles:

$$\hat{J}_\mu = (-)^\mu \sqrt{2\pi\,(1+\delta_{\mu 0})} \sum_{LM} i^L \sqrt{2L+1} D^L_{\mu M}\left(0, -\theta_{\rm np}^{\rm c.m.}, -\phi_{\rm np}^{\rm c.m.}\right) \widehat{Q}^{[L]}_{\mu,M} \ , \tag{1.25}$$

$$\widehat{Q}^{[L]}_\mu = \delta_{\ \mu|1} \left\{ \widehat{T}^{[L]}_{el} + \mu \widehat{T}^{[L]}_{\rm mag} \right\} + \delta_{\mu 0} \widehat{C}^{[L]} \ , \tag{1.26}$$

This results in a multipole decomposition of the T–matrix:

$$t_{sm_s,\mu m_d} = \sqrt{1+\delta_{\mu 0}} \sum_L d^L_{\mu, m_s - m_d}\left(\theta_{\rm np}^{\rm c.m.}\right) \left\langle sm_s \, | \, O^{[L]}_\mu | \, m_d \right\rangle \ , \tag{1.27}$$

where

$$\begin{aligned} \left\langle sm' \, | \, O^{[l]}_\mu \, | \, m \right\rangle = \sqrt{4\pi} \sum_{\lambda l j} \sqrt{\frac{2l+1}{2j+1}} \exp\left(i\delta^j_\lambda\right) U^j_{ls\lambda}\,(l0sm'(\mathrm{ls})\mathrm{jm}') \\ \times\,(1mLm' - m(1\mathrm{L})\mathrm{jm}')\,\mathrm{N}_\mu(\lambda\mathrm{j}) \ , \end{aligned} \tag{1.28}$$

and

$$N^L_\mu|\,(\lambda j) \ = \ i^L \sqrt{2L+1} \sqrt{\frac{M}{2k^{\rm c.m.}}} \sum_{\substack{n'l's' \\ n''l''s''}} U^j_{l's'\lambda'} \left\langle n';\,(l's')\,j\lambda \| \, \widehat{Q}^{[L]}_\mu \, \| n'';\,(l''s'')\,1 \right\rangle$$

$$= \delta_{\mu 1}\left\{E^L(\lambda j) + M^L(\lambda j)\right\} + \delta_{\mu 0} C^L(\lambda j) \ . \tag{1.29}$$

The remaining procedure is then to include all multipoles in equation 1.27 up to a selected cutoff L_{max}. The Born approximation (BA) is then used for all higher multipoles.[8]

$$T = T_{L\,max} + \left(T^{BA} - T^{BA}_{L\,max}\right) \ . \tag{1.30}$$

FA choose the cutoff L_{max} carefully so that the process converges to some reasonable form for the structure function (see figure 1.9). They find that $L_{max} = 6$ is adequate for convergence, the criteria being that L_{max} and $L_{max}+1$ give the same curve. Notice also from figure 1.9 that neither the Born approximation nor a partial wave analysis up to $L_{max} = 6$ can by itself give the correct form for the structure function.

This then comprises the normal theory N. As previously mentioned, it should describe the structure functions near the quasielastic ridge (figure 1.10) quite well. In other energy–momentum transfer domains, the non–nucleon degrees of freedom MEC and IC can play an important role in determining the cross section and structure functions, as we'll see in the next section.

The MEC And IC Corrections Of FA

Figures 1.7-1.8 show examples of the MEC and IC, also referred to as 'interaction effects' in the literature. These effects should become more important in our structure function determination the farther we move off the quasielastic ridge(fig. 1.10). FA add MEC and IC terms to the total current to produce calculations N+MEC, N+IC, and T=N+MEC+IC. The full expressions for these terms can be found in [7].

FA add meson exchange currents and isobar configurations in the following way:

1. an isovector π two-body exchange term is included for the dominant long-range MEC

[8] In the quasielastic peak region where one expects FSI, MEC, and IC to play a minor role, the neglect of MEC and IC and the use of the Born approximation for the final state can result in a closed expression for the T–matrix without resorting to a multipole expansion. When this is done, FA refer to the calculation as the plane wave Born approximation (PWBA). See [7] for the T–matrix formula.

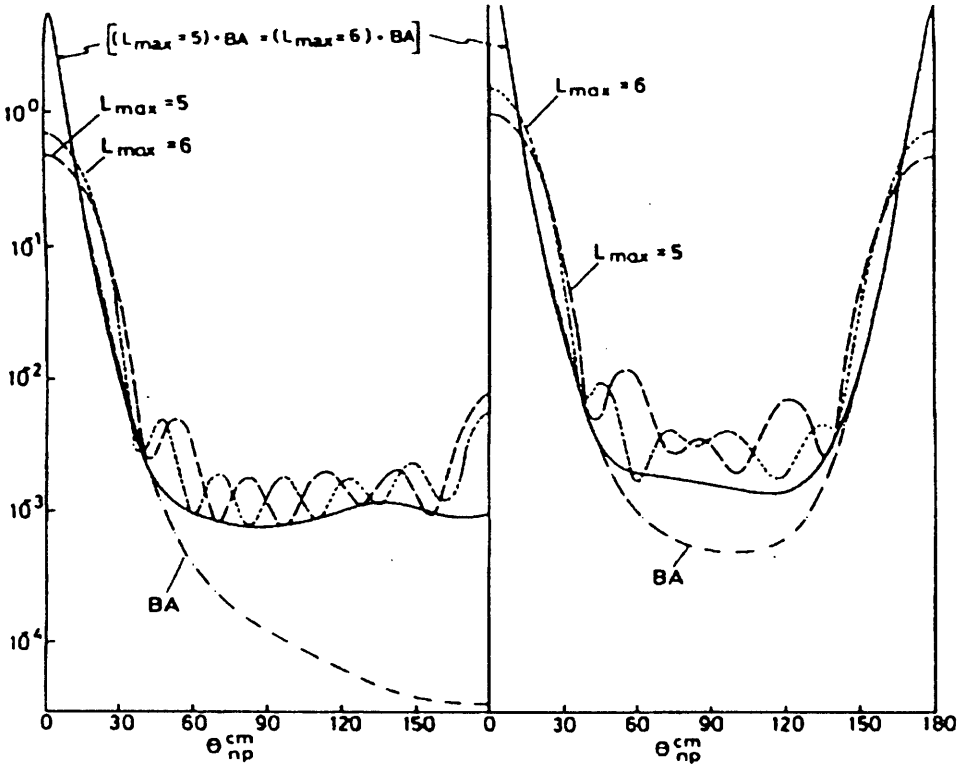

Figure 1-9: Comparison of longitudinal (left) and transverse (right) exclusive structure functions for the truncated multipole series, the Born approximation (BA) only, and the "combined" result (full curves) for E_{np}=140 MeV, q^2_{cm}=12 fm.

contribution

2. for the shorter range MEC, ρ and ω exchange current terms are added

3. A certain part of the long-range part is subtracted out since it was already implicitly included in the N theory. This is called the Siegert correction and follows from Siegert's Theorem [14] [15].

4. As for IC, using the impulse approximation, a term is added to the current for each of the configurations $N\Delta$, $\Delta\Delta$, and $N^*(1470)N$.

Figure 1.10 shows the effect of the FA MEC and IC on the inclusive transverse structure function f_{trans}. Notice that near the quasi–elastic ridge the interaction effects amount to only a few percent. These effects gradually increase in importance the farther we get from this region in center–of–mass momentum transfer and final state center–of–mass np total energy, the latter being closely related to the energy transfer.

Relativistic Corrections

Finally, we need to consider the relativistic corrections FA make which result in their 'total relativistic' theory TRC=T+RC. Starting from their non–relativistic theory, FA add lowest order corrections to the electromagnetic charge and current operators. This amounts to an expansion of the current in factors $\frac{p}{M}$ and $\frac{q}{2M}$. FA also boost the initial and final state wave functions from their rest frames to the final moving frame of the hadronic system.

$$|\, P_n\rangle = e^{i\vec{P}\cdot\vec{R}} U(\vec{P}_n)\,|\, n\big\rangle \ , \tag{1.31}$$

where $|\, n\rangle (n = i, f)$ denotes an intrinsic rest frame wave function and $U(\vec{P}_n)$ is the boost operator, a unitary transformation. Then one obtains for the current matrix element:

$$\tilde{J}_\lambda = \left\langle f \,|\, \tilde{J}_\lambda \left(\vec{q}, \vec{P}\right) \,|\, \right\rangle \ , \tag{1.32}$$

where

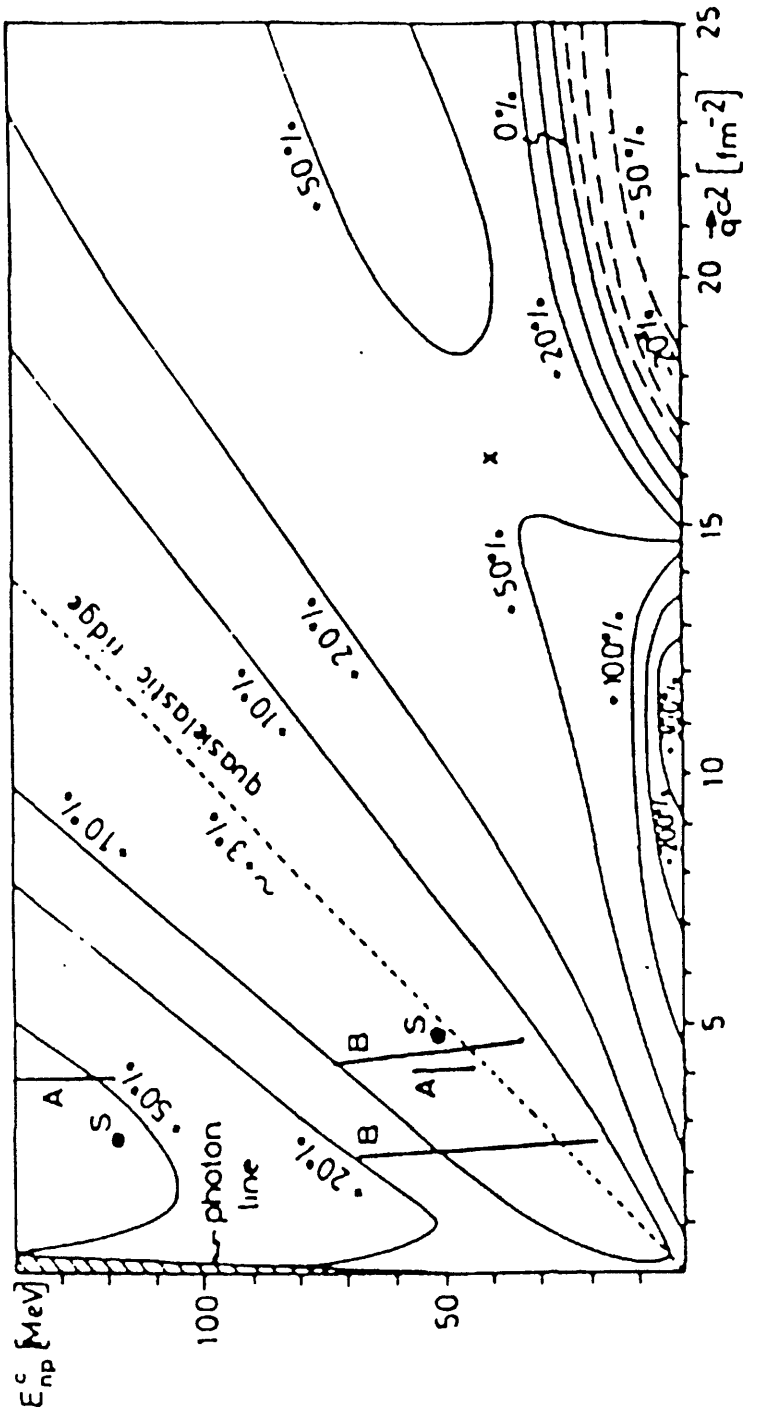

Figure 1-10: change in the integrated(i.e., inclusive) transverse form factor f_{trans} after inclusion of MEC and IC effects in the FA calculation.

$$\vec{q} = \vec{P}_f - \vec{P}_i, \vec{P} = \vec{P}_f + \vec{P}_i, \text{ and}$$
$$\tilde{J}_\lambda\left(\vec{q},\vec{P}\right) = \int d^3R\, U^\dagger\left(\vec{P}_f\right) J_\lambda(0) U\left(\vec{P}_i\right) e^{-i\vec{q}\cdot\vec{R}} \tag{1.33}$$

acts on intrinsic coordinates only. Corrected formulas for the current can be found in [12].

Results

FA calculate both cross sections and structure functions with their method. We can see from figures 1.11-1.12 that the structure functions can be much more sensitive to interaction effects than the cross section itself. This is one of the important reasons for measuring the structure functions individually.

Figure 1.13 shows the FA calculation for the kinematics of the Bernheim experiment. This experiment measured the D(e,e'p) cross section at two different sets of kinematics and over a wide range of missing momenta. We see that the total theory (T) fits the data well over the entire range of p_i covered.

Figure 1.11 shows the FA calculation of the structure functions as a function of θ_{np}^{cm}. Notice the importance of MEC and IC as we look at each structure function. Since MEC and IC are mainly 3–current effects, we shouldn't be surprised to see that R_T and R_{TT} show the greatest sensitivity to these, while R_L shows very little sensitivity to MEC and IC.

1.4 Previous Measurements

Measurements of the inclusive D(e,e') cross section have shown evidence for the existence of MEC and IC, especially electro-disintegration at threshold and large momentum transfer [16] [17]. The exclusive D(e,e'p) cross section should yield additional information about these processes, such as their dependence on internal nucleon momenta. At sufficiently high energy and momentum transfer, even sub-nucleon degrees of freedom (i.e., quarks and gluons) in the Deuteron can be probed [18]. The D(e,e'p) cross section has been measured

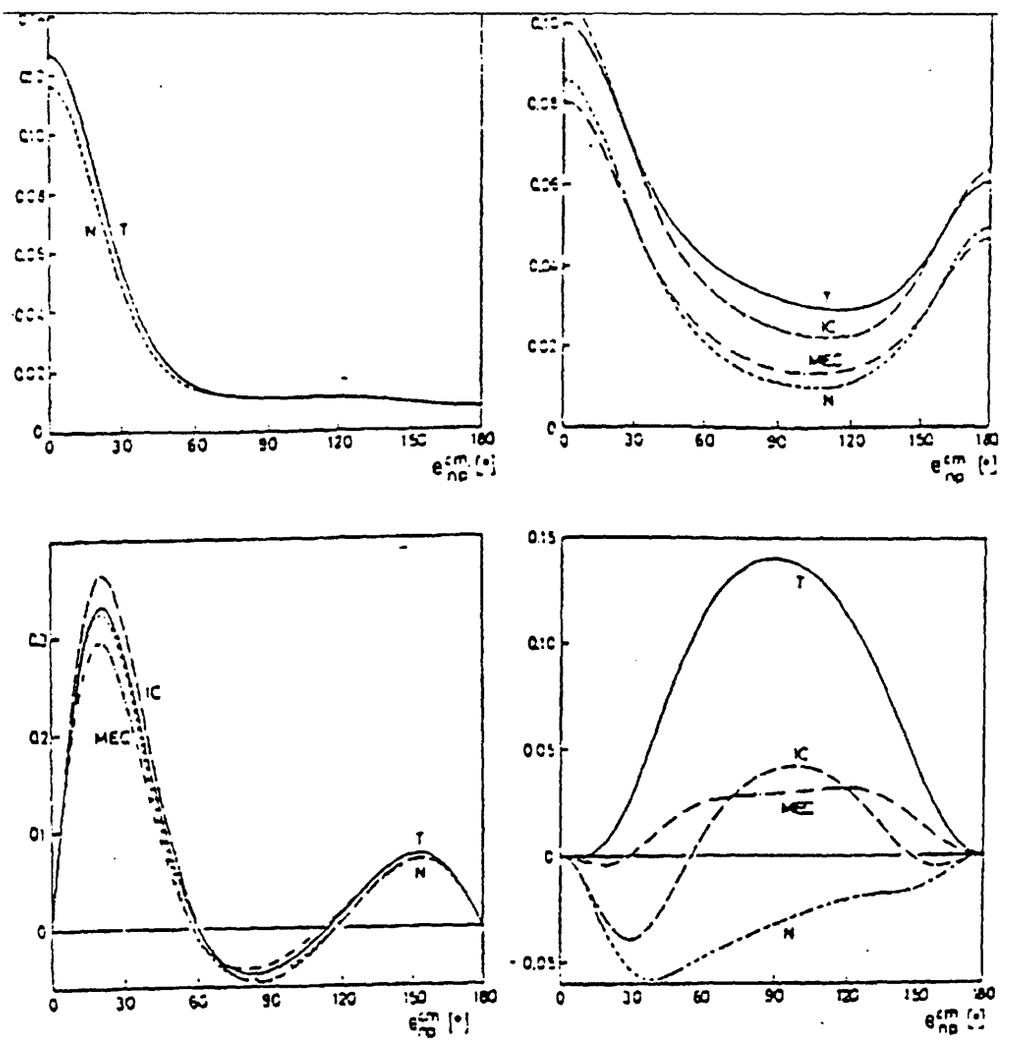

Figure 1-11: The four structure functions at $E_{np} = 140$ MeV, $q^2_{cm} = 2.33\ fm^{-2}$ R_L (upper left), R_T (upper right), R_{LT} (lower left), R_{TT} (lower right). Relativistic effects not included in 'T'.

at kinematics comparable to ours in recent years [19] [20].

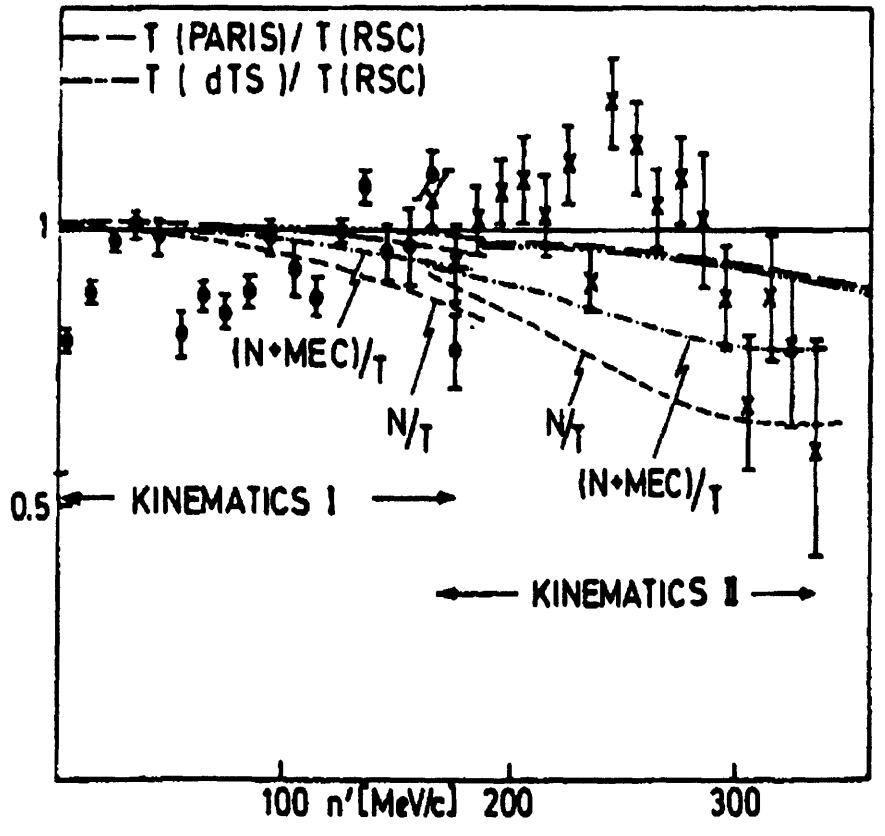

Figure 1-12: Ratios of Bernheim measurements to the total theory (T=N+MEC+IC, i.e. theory without relativistic corrections) of FA (points). Also plotted are ratios of FA theory components with the total theory(curves). As is shown, the Bernheim data was taken at two different sets of electron kinematics.

We see from figure 1.12 that the measured cross section is within 20-25% of the FA total non-relativistic cross section up to a missing momentum of 300 MeV/c. Using PWIA assumptions, the Deuteron momentum distribution was also obtained from the measured D(e,e'p) cross section (Fig. 1.13 from [7]). As we expect, $\rho(p)$ has the s-wave shape, the d-wave contribution being small.

There have been two experiments besides ours that have separated some of the D(e,e'p) struc-

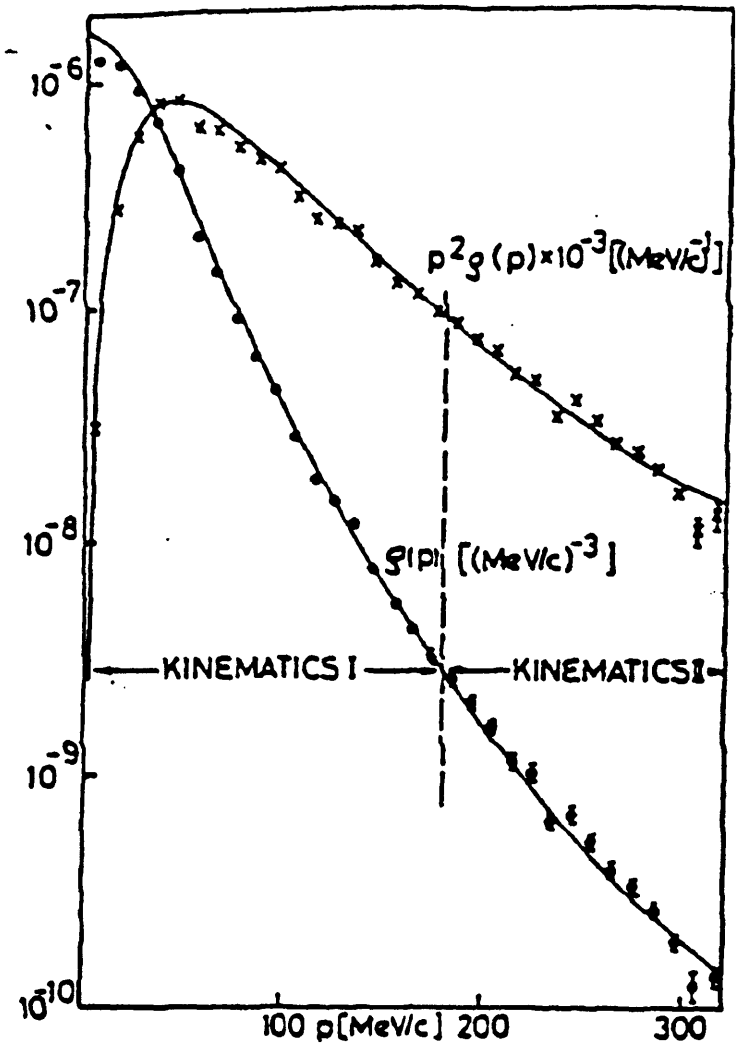

Figure 1-13: Deuteron momentum distribution determined from Bernheim data.

ture functions. One was performed at NIKHEF, the other at Saclay. The NIKHEF group measured R_L, R_T, and R_{LT} over a range of missing momenta [21] [22]. Figures 1.14-1.15 show their results for R_{LT} and A_ϕ, where A_ϕ is the LT asymmetry given by

$$A_\sigma = \frac{\sigma_0 - \sigma_\pi}{\sigma_0 + \sigma_\pi} \tag{1.34}$$

σ_π and σ_0 are the measured cross sections at $\phi_{pq} = \pi, 0$ respectively.

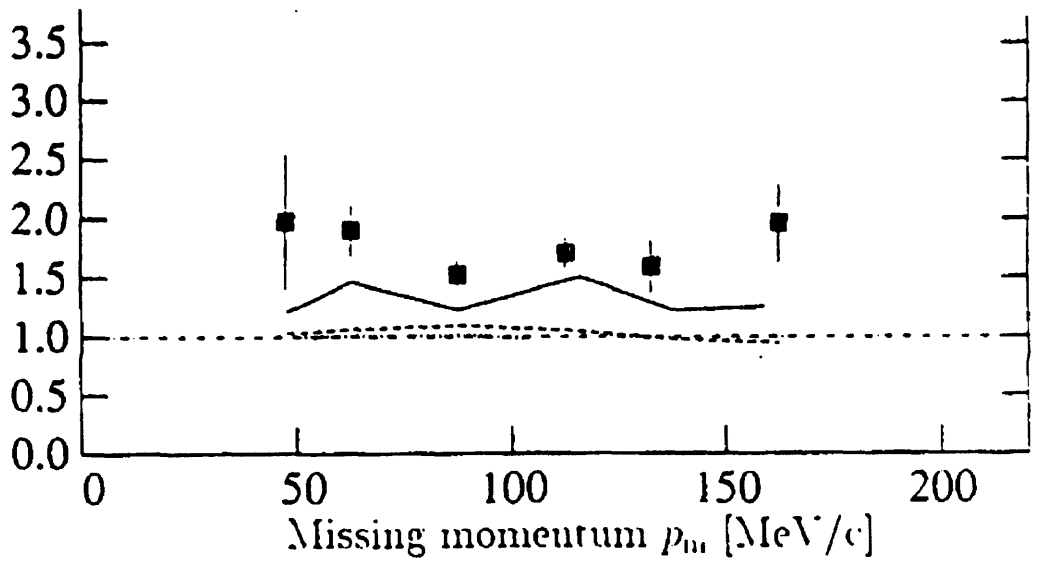

Figure 1-14: Ratio of LT interference structure function measured at NIKHEF (points), Tjon–Hummel(solid) fully relativistic theory, and the FA non-relativistic total calculation (dashed), with a non–relativistic PWIA calculation. The dot-dashed curve is the ratio of PWIA with itself.

We see that both plots show a disagreement between non-relativistic total (T) FA and the data. A fully relativistic calculation by Hummel and Tjon shows better agreement with the data. This result is not surprising. Mosconi and Ricci [23] have shown that relativistic corrections to the nucleon form factors produce larger absolute values for R_{LT} and A_ϕ,

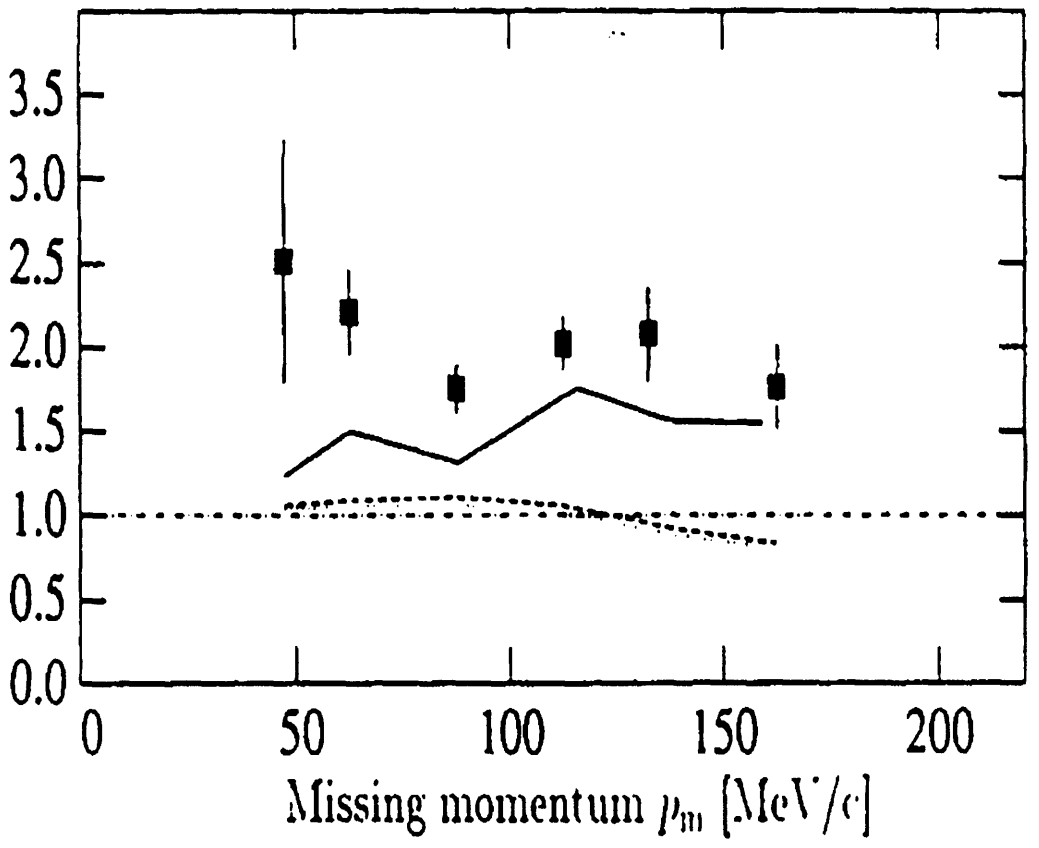

Figure 1-15: LT asymmetry measured at NIKHEF and divided by that calculated in PWIA (points) compared to the same ratio for the FA non-relativistic T calculation (dashed) and the Tjon–Hummel(solid) relativistic theory.

which would correct the FA curve in the proper direction. What wasn't demonstrated until these measurements was the possibility that relativistic corrections or theories would be important in describing a structure function. Indeed, R_L and R_T do not show such sensitivity to relativistic corrections [24] [25].

The group at Saclay [26] [27] [28] has measured cross sections and several structure functions for Deuterium, ^{3}He, and ^{4}He at kinematics similar to ours and at a few points in the range $50\frac{MeV}{c} < p_i < 150\frac{MeV}{c}$.

Figures 1.16-1.17 show their results for R_{LT} and A_ϕ.

Again we see that FA predict a value for $\| A_\phi \|$ that tends to be low relative to the data. Mosconi and Laget give calculations for A_ϕ that include relativistic corrections. Notice that these correct the FA curve in the right direction, even though they both may overshoot the measurements slightly.

It is interesting to note that although Saclay shows agreement with NIKHEF in their measurement of A_ϕ, the two groups disagree somewhat in their comparisons of measured values of R_{LT} with those predicted by FA. NIKHEF disagrees with FA, while Saclay seems to show agreement (compare figs. 1.14 and 1.16). More will be said about this in chapter 4. For now it should suffice to say that A_ϕ is much less sensitive to certain theoretical ambiguities in the calculation of the absolute cross section than R_{LT}.

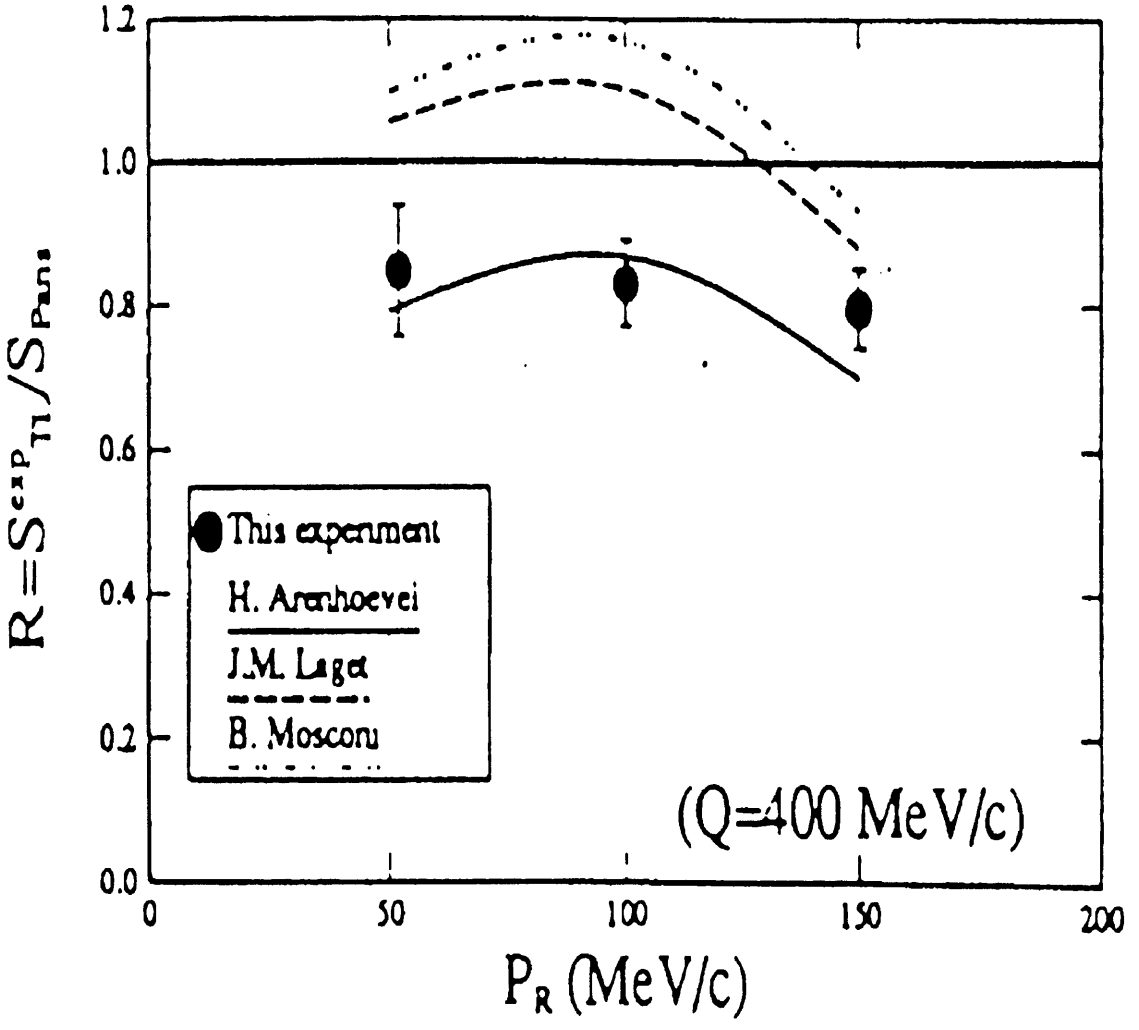

Figure 1-16: LT interference structure function measured at Saclay and expressed as a ratio of the corresponding spectral function to the PWIA spectral function using the Paris potential. It is compared to the same for FA total, Laget, and Mosconi calculations.

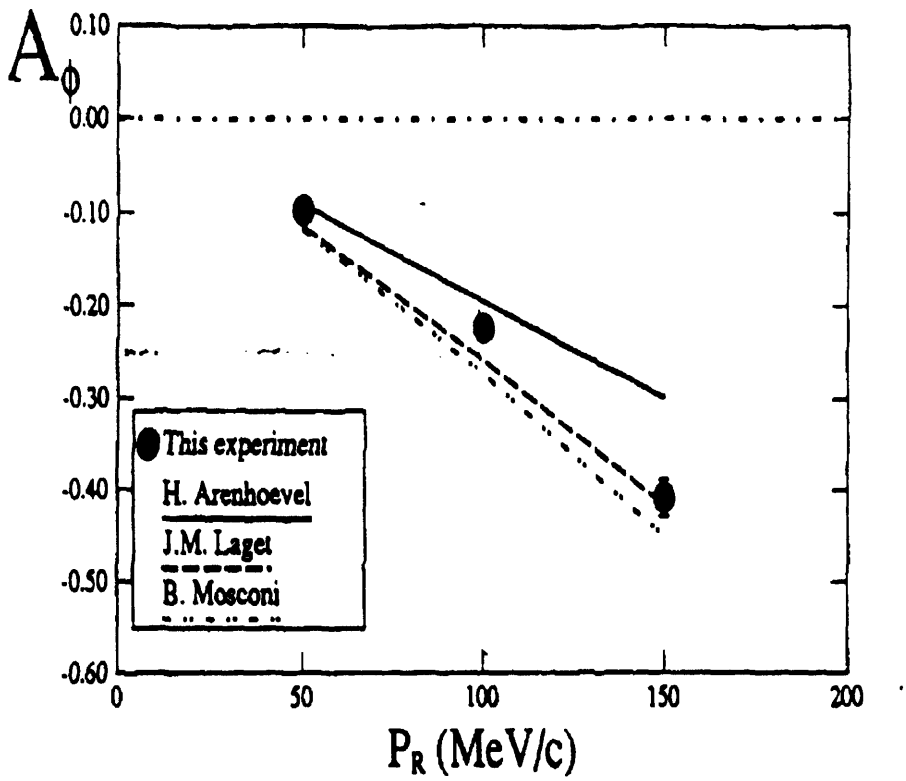

Figure 1-17: LT asymmetry measured at Saclay and compared to FA total, Laget, and Mosconi calculations.

Chapter 2

Experimental Apparatus and Data Acquisition

We performed the experiment in 1991 at the Bates Linear Accelerator Center in the North Experimental Hall on Beam Line S. We used ELSSY (energy loss spectrometer system) to detect electrons and the new OOPS (Out-of Plane Spectrometer) to detect protons. Our beam energy was 576 MeV. This chapter briefly describes the accelerator, the two spectrometers with their associated instrumentation, the trigger hardware, and the data acquisition software.

2.1 The Accelerator

At the time of the experiment, Bates was a 1 GeV recirculated pulsed electron linear accelerator. The second pass beam pulse length is about 13 μs at a repetition rate of 600 pulses per second giving an instantaneous duty factor of 0.8%. The beam peak current was typically 4 milliamps giving an average current of about 32 microamps. We determined the beam energy to one part in 10^3 by off-line analysis involving mainly differential recoil of several nuclear masses (see chapter 3 for more details). The momentum dispersion of the beam was 0.3%. The spot size on target was 1mm horizontal and 5mm vertical. This small vertical spot size was achieved for the data runs by increasing one of the beam focussing magnets (SQ7), and by reducing the accelerator's energy defining slits (see fig. 3.2 in [31]).

The two spectrometers, ELSSY, the electron arm, and OOPS, the proton arm, were located on Beam Line S in the North Experimental Hall. Most of the electronics and the data aquisition computer were located in the North Hall Counting Bay. I will occasionally

refer to the North Experimental Hall and North Hall Counting Bay as 'downstairs' and 'upstairs' respectively.

We detected electrons at 44°. The protons were detected at 64.7° ($\theta_{pq} = 11°$, $\phi_p = 180°$) and at 42.9° ($\theta_{pq} = 11°$, $\phi_p = 0°$). We set the electron spectrometer (ELSSY) angle and momentum to look at events where $\omega = 105$ MeV and $\vec{q} = 400$ MeV/c at $\theta_q = 53.8°$. We then placed the proton spectrometer (OOPS) at the two in-plane positions having $\theta_{pq} = 10.9°$. Namely, 64.7° and 42.9°. We fixed the proton spectrometer central momentum at 440 MeV/c corresponding to $p_i = 88$ MeV/c.

We positioned the two spectrometers around an evacuated target chamber containing six targets on a moveable ladder (CH_2 and CD_2 spinners, 36 mg/cm^2 BeO, 26/67 mg/cm^2 C/LiF composite, and two natural carbon targets of 69 and 209 mg/cm^2). We used the polyethylene (CH_2) spinner target for single arm and coincidence normalizations. We used the (CD_2) spinner for D(e,e'p)data taking, monitoring its thickness with D(e,e') elastic runs in ELSSY. We used the beryllium-oxide (BeO) target for beam on target position checks and beam energy calibrations. The C/LiF composite data were intended for off-line beam energy calibration, but were found not to be useful. Finally, we used the two carbon targets for focal plane efficiency determinations in both spectrometers, background subtraction from D(e,e'p)data, and an R_{LT} measurement on Carbon.

The following sections give details of the spectrometers. See figure 2.1 for the layout of the Bates Linear Accelerator.

2.2 ELSSY – The Electron Arm

ELSSY (Energy Loss Spectrometer System) has been used in electron scattering experiments at Bates for more than fifteen years. This spectrometer and its focal plane instrumentation have been described in detail in several theses and publications. Therefore, in this section, I will only briefly describe some of their important features. For a more detailed treatment, see [29], [30].

As its name suggests, ELSSY determines the energy loss of an electron after scattering.

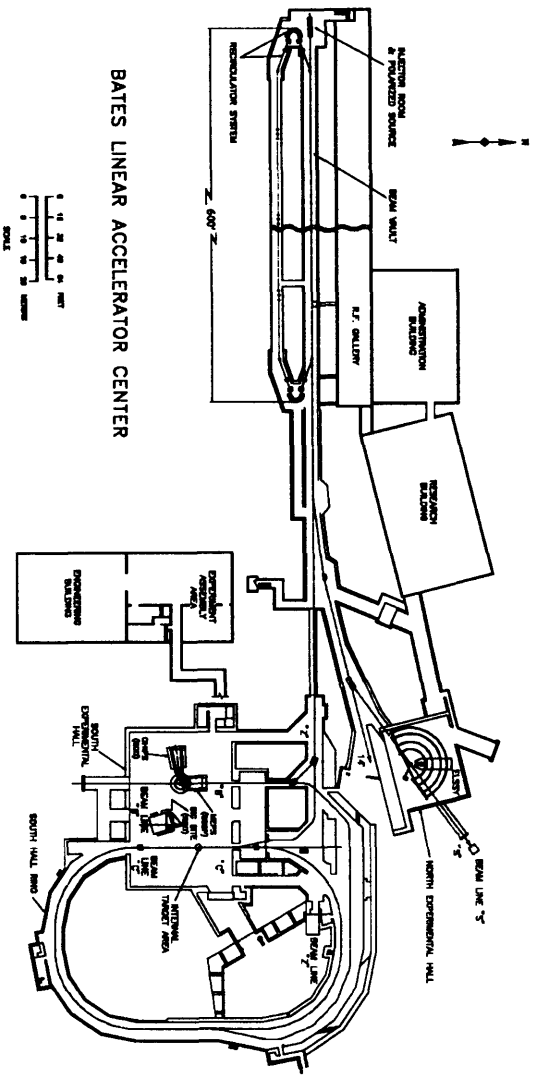

Figure 2-1: The Bates Accelerator Center–Middleton, MA.

Solid Angle	3.3 msr
Scattering Plane (ϕ)	26.2 mr (vert. slit = 2in.)
Bend Plane θ)	127 mr (hor. slit = 10in)
Momentum Acceptance	6%
Maximum Momentum	900 MeV/c
Momentum Resolution	2.10^{-4}
Radius of Curvature	2.23 m
Flight Path	$\approx$ 7 m
Bend Angle	90.0°

Table 2.1: ELSSY Parameters.

It can achieve an energy resolution of about 1 part in 10^4. This requires dispersing the electron beam on target to match the spectrometer dispersion [31]. The scattered electrons are momentum analyzed and transported to the detectors by a split dipole magnet (fig. 2.2). Horizontal and vertical slits in the snout of the spectrometer define the solid angle acceptance. These are located 76.375 (horizontal) and 78.75 (vertical) inches from the target. The slit settings used for this experiment and other ELSSY characteristics are shown in table 2.1.

ELSSY is instrumented with a VDC (vertical drift chamber) to measure bend plane position and angle of the electrons, four transverse arrays (horizontal drift chambers) to measure transverse plane position and angle, a gas Cerenkov counter to reject pions, and two scintillators (figure 2.3). Each scintillator has a single phototube. These are located at opposite edges of the scintillators. A recent addition to the ELSSY focal plane instrumentation is an array of Lead-glass blocks that provide for rejection of ultra-relativistic cosmics, such as a μ^-. The Lead-glass was not crucial in our experiment (see chapter 3). The readout of the wire chambers is via a delay line system and the trigger was the meantimed **AND** of the two scintillators, **AND**ed with an **OR** between the Cerenkov and the Lead-Glass.

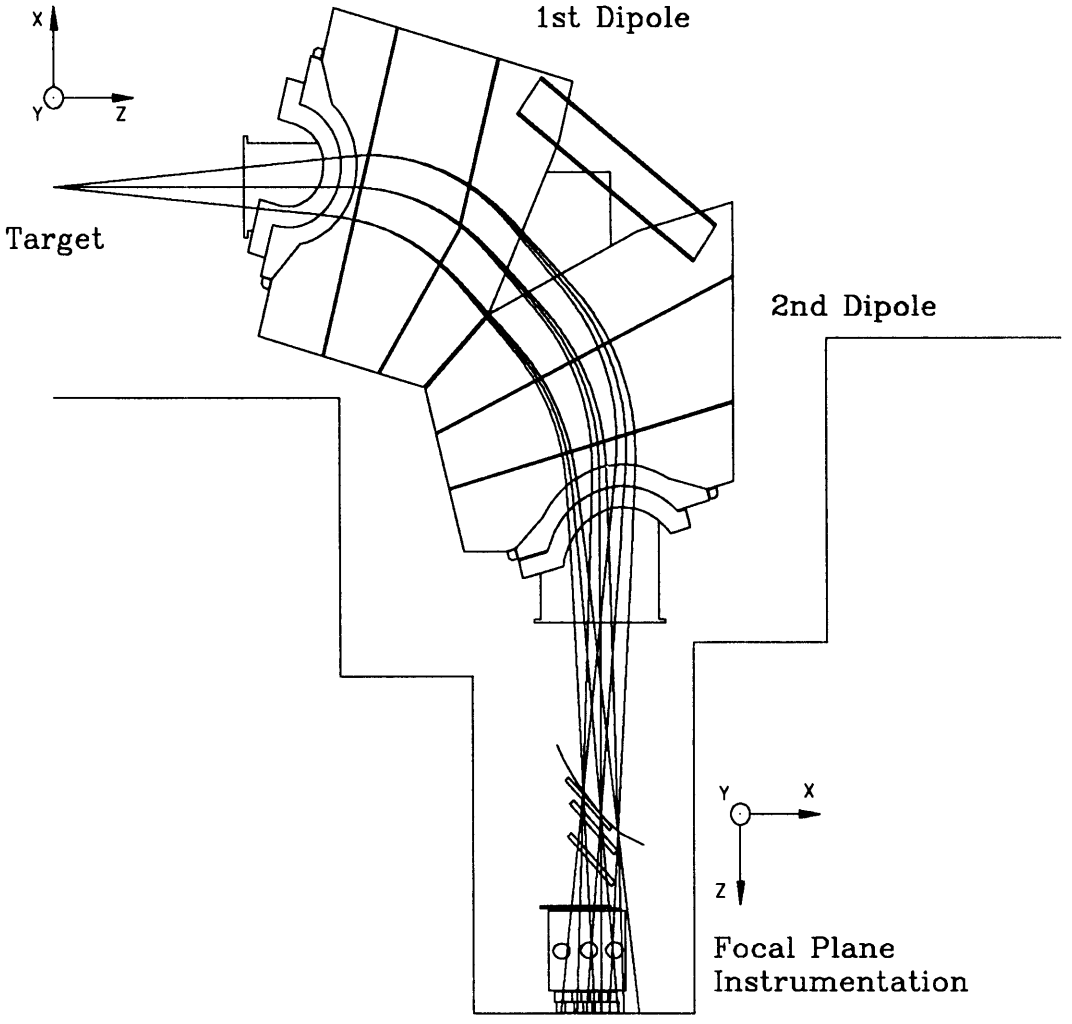

Figure 2-2: Schematic diagram of ELSSY.

For more details concerning the ELSSY trigger electronics, see [32]

2.3 OOPS

The proton spectrometer OOPS (Out-Of-Plane-Spectrometer) was designed and assembled under the direction of the University of Illinois group. Its detector package, consisting of three scintillators and three horizontal drift chambers (HDC's), was designed and built by the MIT group. Each HDC has an X plane (vertical position,i.e., position in bend plane) and a Y plane (horizontal position, i.e. position in transverse plane). The testing of the fully instrumented spectrometer was done by a collaboration consisting mainly of these two groups.

This spectrometer derives its name from the fact that, due to its small size and weight, it can be mounted out of the electron scattering plane in reactions X(e,e'p), providing the ability to determine response functions not measurable in in-plane experiments. OOPS was mounted in-plane for this experiment.

The OOPS is equipped with two magnets (a dipole and a quadrupole), the detector package, collimators, four inches of lead shielding near the detector package, and a vacuum system (see figures 2.4 and 2.5). It has a vertical bend plane and flat region of 10% $\frac{\Delta p}{p}$ momentum acceptance. OOPS has point-to-point focussing in the bend plane ($< x_f \mid \theta_T >= 0$) with a maximum solid angle acceptance of 1.2m̃sr oriented vertically ($\approx$ 24m̃r by 50m̃r). Its magnets can provide fields of up to 8kG, corresponding to a maximum central momentum of 830 MeV/c. See table 2.2 for a summary of the OOPS characteristics [33].

The HDC's measure the focal plane coordinates $(x_f, \theta_f, y_f, \phi_f)$, where θ_f is the angle of the particle trajectory in the bend plane and ϕ_f is this angle in the transverse plane. The third HDC provides redundancy to measure detector efficiencies. The scintillators provide a fast trigger and timing information and allow for rejection of the $\pi+$ background.

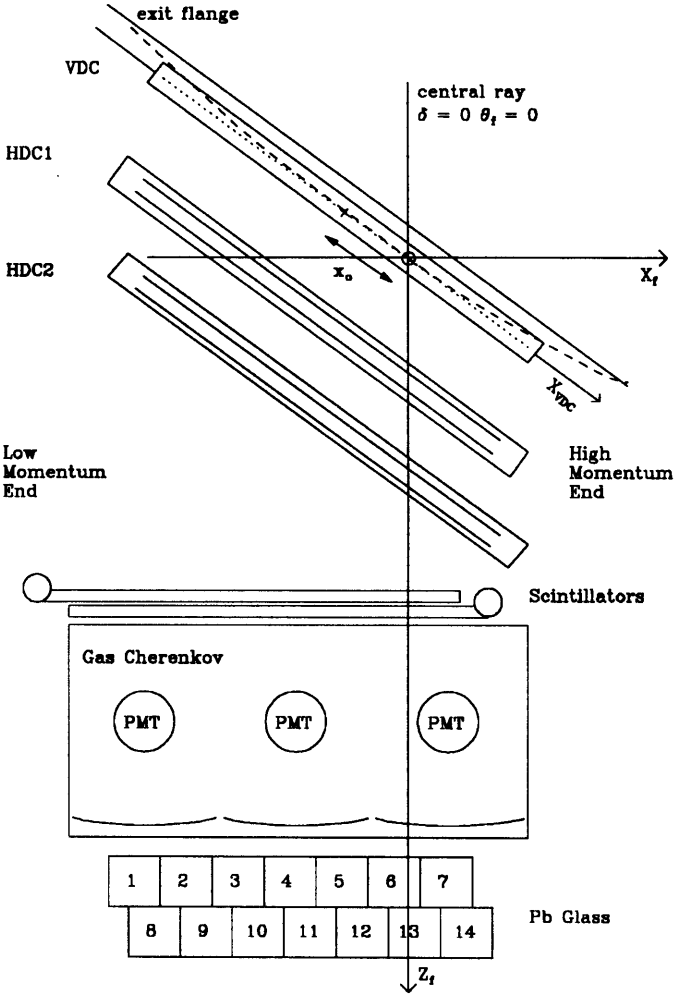

Figure 2-3: The ELSSY focal plane array.

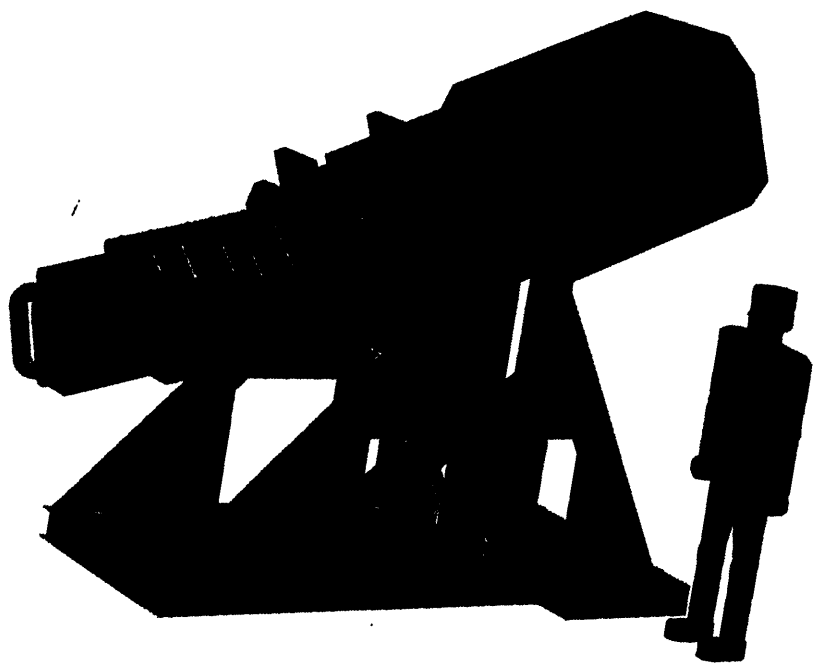

Figure 2-4: Drawing of OOPS sitting on its support structure.

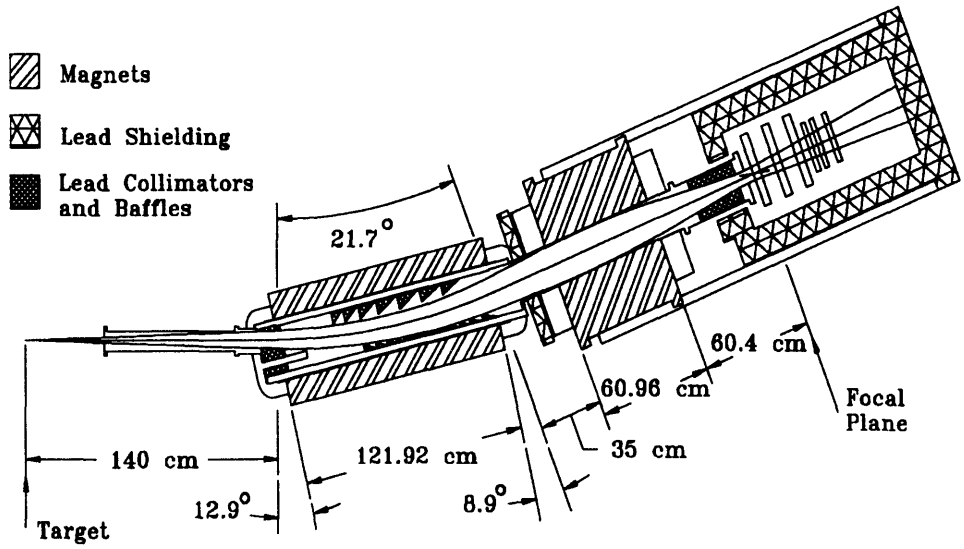

Figure 2-5: Schematic diagram of OOPS.

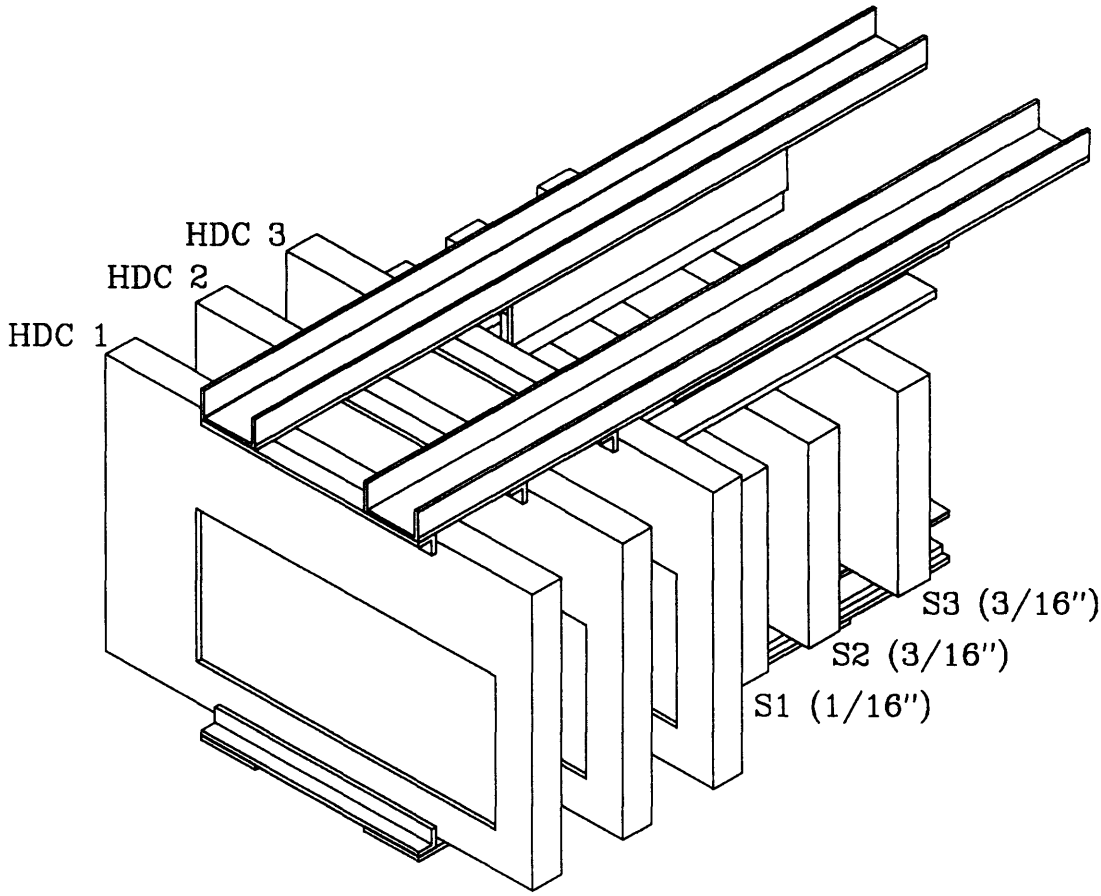

Figure 2-6: OOPS focal plane array.

Solid Angle	1.2 msr
Scattering Plane (ϕ)	24 mr
Bend Plane θ)	50 mr
Momentum Acceptance	10%
Maximum Momentum	830 MeV/c
Momentum Resolution	
Design	$3.5 \cdot 10^{-3}$
Best Obtained	$4.5 \cdot 10^{-3}$
Radius of Curvature	3.47 m
Flight Path	4.2 m
Bend Angle	21.7°

Table 2.2: OOPS Parameters.

2.3.1 The OOPS Scintillators

The three OOPS scintillators, which incorporate fiber-optic light pipes to connect each end of a scintillator to two photo-multiplier tubes, provide the OOPS trigger and the timing fiducial for the drift-chamber delay lines. The thicknesses of the scintillators (1/16", 3/16" and 3/16" in the direction of particle travel) allow low energy particle detection and particle identification, i.e. π_+ rejection [34]. The scintillators were modeled after those of the One Hundred Inch Proton Spectrometer (OHIPS) at Bates [5]. They have an active area of 7in. by 17in. The light pipes were quite flexible, allowing the detectors to fit inside the small space available.

2.3.2 The OOPS Scintillator Electronics

We ran the phototubes at between 2350 and 2750 volts, depending on the phototube. Signals from S2 and S3 were fanned out, one signal going to an ADC and the other going to a discriminator. Signals from S1, the thin scintillator, were amplified and sent to an ADC

and a discriminator. All scintillator signals were sent to constant fraction discriminators for improved timing resolution. See figure 2.7 for a logic diagram of the OOPS scintillator electronics and trigger.

Both sides of each scintillator were ANDed downstairs, forming one logic pulse per scintillator. The 3-fold coincidence of these pulses determined the OOPS single arm trigger, giving a start to all OOPS TDC's.

2.3.3 The OOPS HDC

The OOPS HDC's were built using a design developed at LAMPF [35]. Each chamber consists of two detection planes, rotated 90 degrees with respect to one other, to provide an X and Y measurement of the particle position. A detection plane consists of two types of wires: anode or signal wires (20 micron gold-plated tungsten) spaced 8 mm apart, and field defining cathode wires (76 micron gold-plated copper-clad aluminum). The two types of wire alternate in the HDC with a 4 mm space, anode to cathode. The anode wires are maintained at positive high voltage, while the cathode wires are at ground. The two planes of anode wires are separated by 0.25 mil aluminized mylar cathode planes; the distance from an anode plane to a neighboring cathode plane is 4 mm(see figure 2.7). The X (bend) and Y (transverse) planes in our chambers contain 21 and 38 wires, respectively. The total active area for an HDC is approximately 17 cm by 32 cm. The HDC's require continuous flushing with a gas mixture of 65% argon, 35% isobutane. The argon bubbles through isopropyl alcohol, which is refrigerated at 35° F, before mixing with the isobutane. We distribute the gas mixture to the three HDC's in parallel. This arrangement minimizes the flushing time needed for normal operation. Each HDC used in the prototype OOPS detector package has its gas inflow and outflow ports located on the same (front) cover plate. This configuration leads to relatively poor gas flow, since the gas must diffuse toward the rear of the chamber through holes in the intervening aluminum plates. We will implement an improved design in future OOPS HDC's.

We operated the HDC's at 2500 to 2600 V. This is higher than the 2150 V reported for

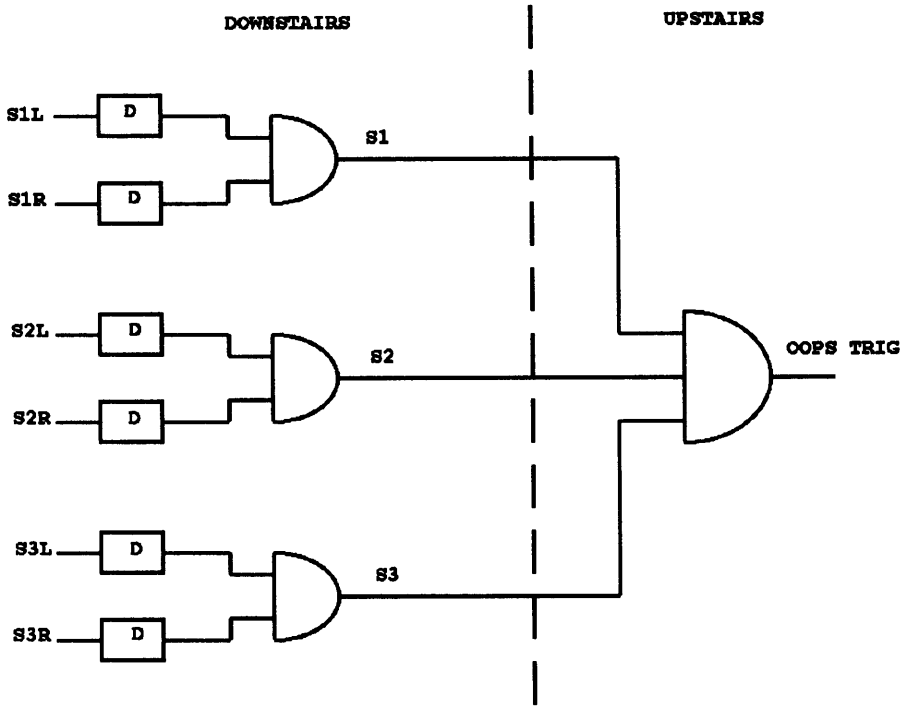

Figure 2-7: OOPS scintillator and trigger electronics.

this HDC at LAMPF. This was due to the difference in elevation. We used the chambers at sea level, whereas LAMPF is at a higher elevation and thus at a lower atmospheric pressure. Our gas density is then higher, making higher voltages necessary to create the optimum electron avalanche.

In figure 2.8 we show a typical efficiency vs. voltage curve for an OOPS HDC wire plane. Note that the efficiency approaches 100% in the region from 2.5 to 2.6 kV.

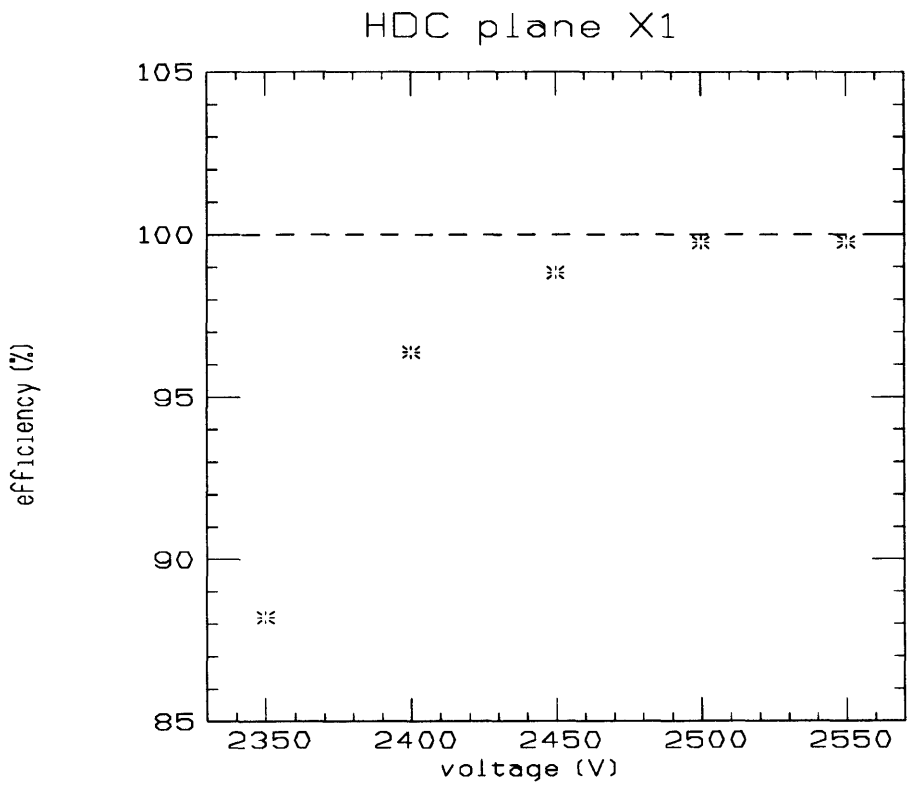

Figure 2-8: OOPS HDC efficiency vs. voltage.

2.3.4 The OOPS HDC Readout

We read out the OOPS HDC's using a delay line system. Each wire plane has one delay line. Each OOPS HDC is equipped with a high-voltage distribution box that provides high voltage for its two delay lines (one each for the X and Y planes). The HV input line is connected via current-limiting resistors to the two ends of each delay line. The HV inputs are capacitively coupled to BNC output jacks, one for each end of a delay line. Delay line signals from these output jacks are then pre-amplified. The signals from the pre-amplifier are integrated with an RC circuit and discriminated with constant fraction discriminators. The RC integrator was helpful in providing a uniform signal shape for input to the discriminators. The logic pulse generated by the CFD serves as the STOP signal for a TDC; the START signal comes from the OOPS scintillator trigger. See figure 2.9 for a diagram of the OOPS wire chamber electronics.

At the wire plane, signals induced in the anode wires travel in both directions along the delay line to either end to form the stops for two TDC's. There is a fixed time delay (τ) between successive taps.Thus, the arrival time of the signal at both ends of each delay line relative to the scintillator trigger is measured (t_L and t_R). From these arrival times, the number of the struck wire and the drift time to that wire can be determined as follows: let N be the number of wires along the delay line and t_d the drift time to wire number n. Then

$$t_L = (n-1)\tau + t_d \tag{2.1}$$

and

$$t_R = (N-n)\tau + t_d \ . \tag{2.2}$$

These equations are then solved for t_d and n:

$$t_d = \frac{1}{2}(t_L + t_R - (N-1)\tau) \tag{2.3}$$

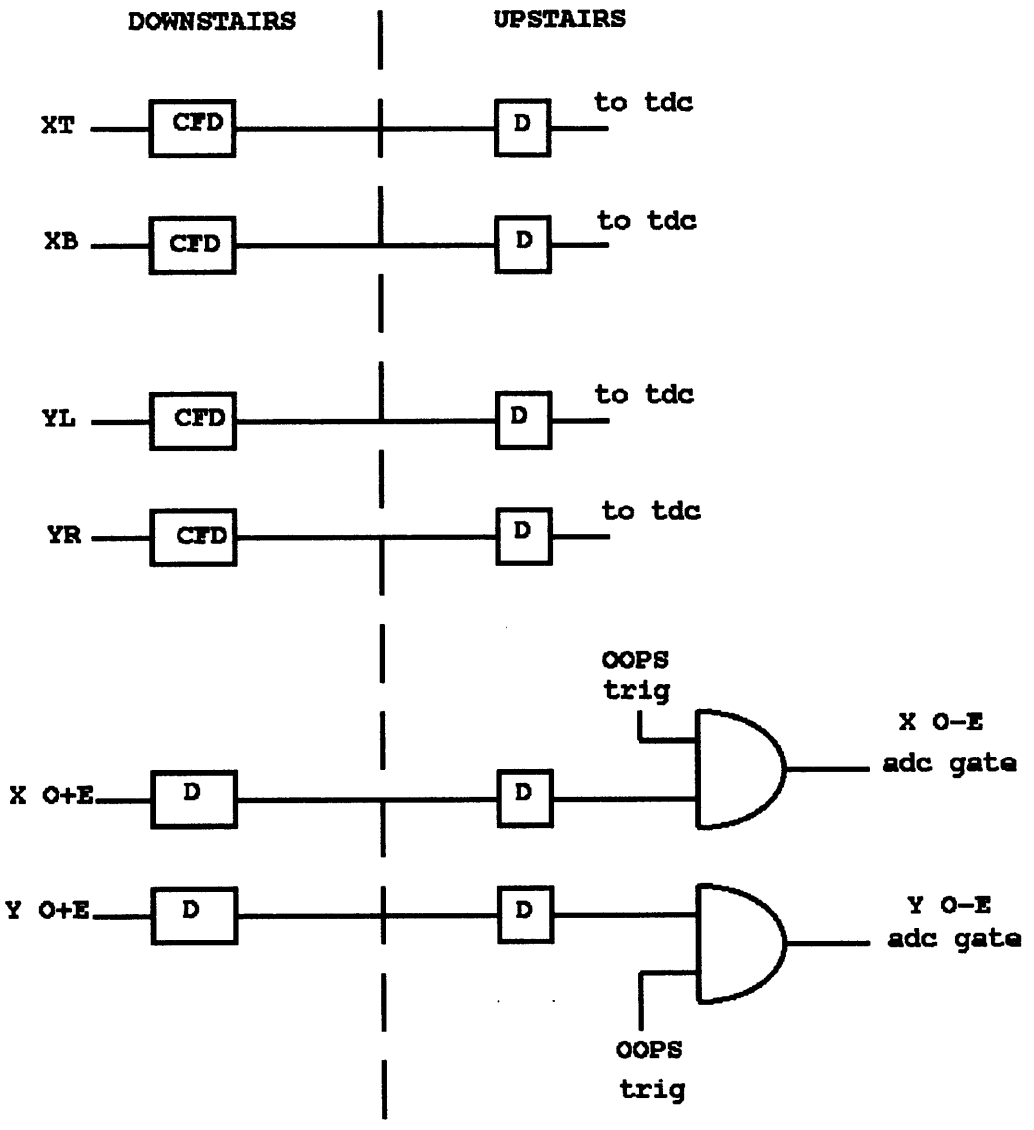

Figure 2-9: OOPS HDC logic.

and

$$n = \frac{1}{2\pi}(t_L - t_R + (N+1)\tau) \quad . \tag{2.4}$$

The code then performs the calculation to extract t_d and n for each wire plane. A spectrum of time differences for one delay line is shown in figure 2.10. Discrete peaks occur at integer values of the wire number n. As can be seen by the peak to valley ratio, individual wires can be identified with certainty.

Two more pieces of information are needed to reconstruct the particle trajectory. These are the drift-time to drift-distance conversion and the left-right information. The latter refers to the fact that in order to calculate the intercept of the particle track in a given wire plane, one must determine on which side of the active signal wire the track passed. The OOPS HDC's use the current pulses induced on the field-defining cathode wires (which alternate with the anode wires) to make this left-right decision. Every other cathode wire in a wire plane is bussed together, giving two cathode output signals per plane. A differential amplifier measures the difference in the induced current for the two sets of cathode wires. For an odd signal wire, a positive difference or "O-E" signal results for tracks passing to one side of the wire, and a negative difference for tracks passing on the other side. Even signal wires display the reverse of this pattern. The "Odd/Even" (or "O/E") amplifier also generates the analog sum of the two cathode signals; this sum or "O+E" signal can be used to define the timing of the gate to the ADC that integrates the O-E signal. This O+E timing was critical for getting good O-E spectra.

Figure 2.11 displays a typical histogram of the integrated difference signal; the two peaks, representing tracks passing by the two sides of the signal wires, stand out clearly. The gap between the two peaks, about 1% of the spectrum, is populated by those events so close to the signal wire that no clear left-right resolution is possible. Fortunately, these events are within a distance from the wire comparable to the chamber resolution so that the left-right decision is not important. For more information regarding left-right decisions, see [36]. For details of drift-time to drift-distance conversion and more information on wire chamber analysis in both ELSSY and OOPS, see Chapter 3.

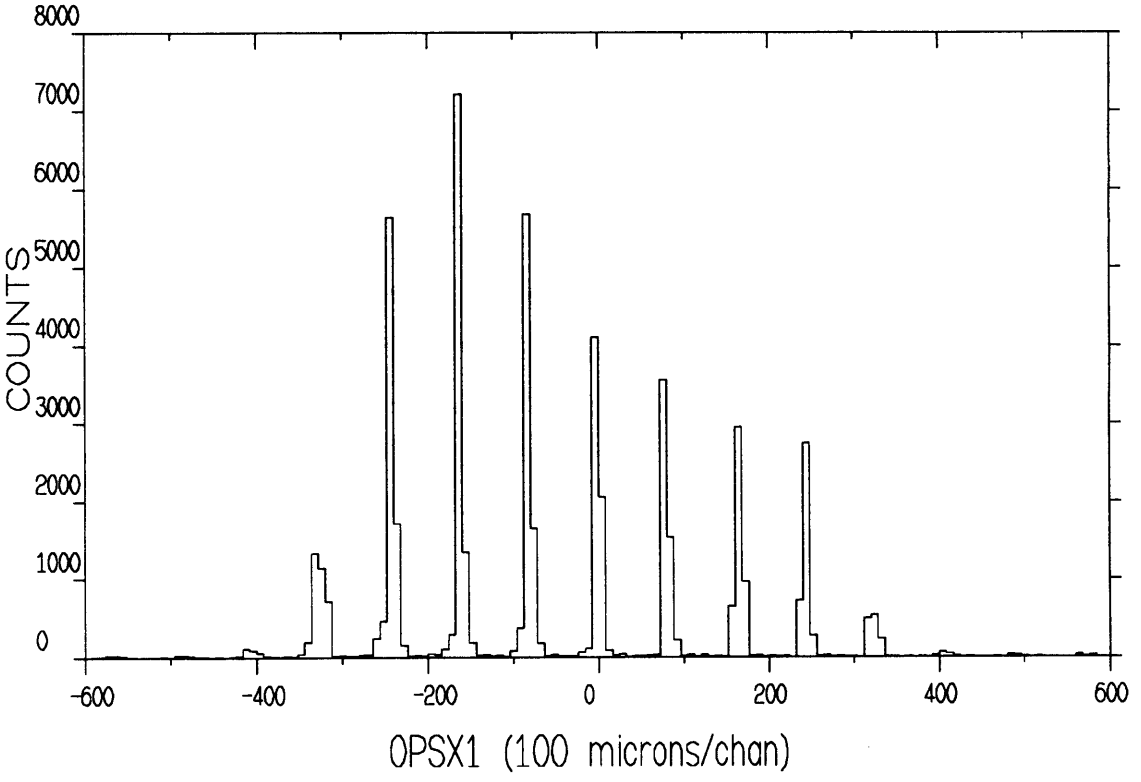

Figure 2-10: Typical OOPS Delay Line difference spectrum.

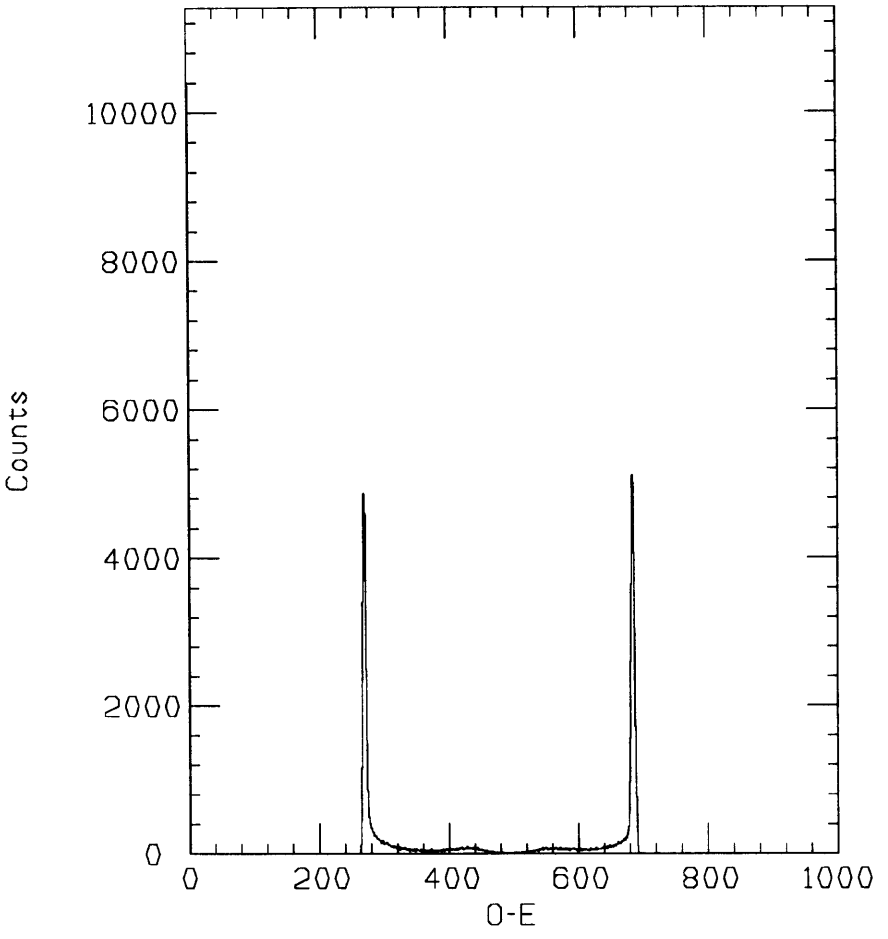

Figure 2-11: Integrated difference signal for Left-Right decision.

2.4 ELSSY-OOPS in Coincidence

D(e,e'p)data were taken using both of the previously described spectrometers in the Bates North Hall (fig. 2.12).

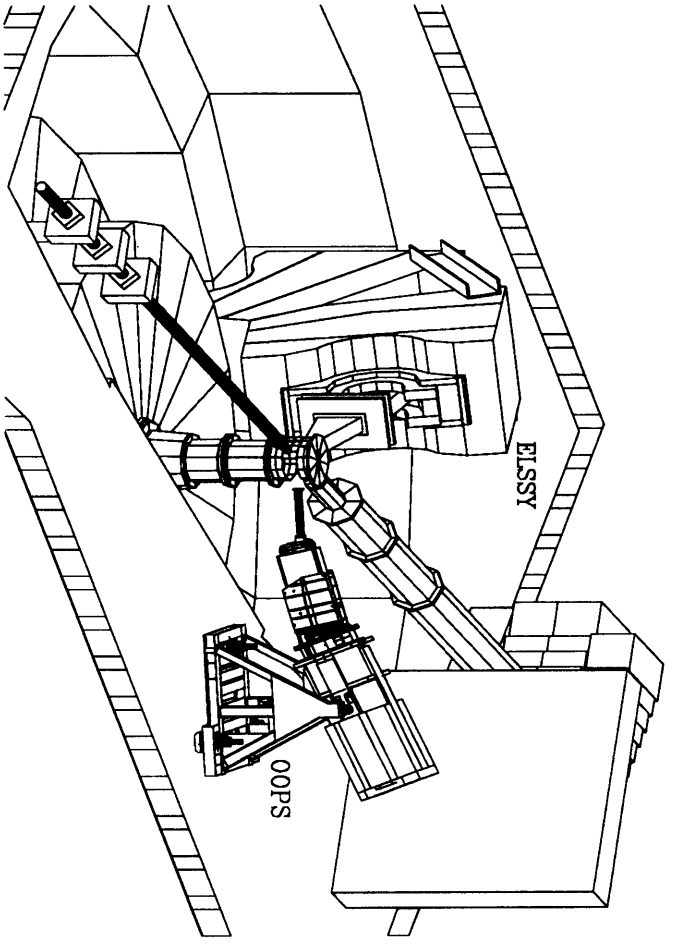

Figure 2-12: A drawing of the Bates North Hall showing ELSSY and OOPS.

2.4.1 The Coincidence Trigger Module

The coincidence trigger module provided the experimental trigger. See figure 2.13 for the coincidence data acquisition logic flow including the trigger module and figure 2.14 for the exact layout of the coincidence trigger module. A similar set-up has been used several

times previously in coincidence experiments (see [5]). The coincidence trigger module had the following features:

1. It created a coincidence trigger whenever there was an OOPS event within a 100ns window defined by an ELSSY event. This wide coincidence timing gate allowed for extensive sampling of the accidental background rate. It also allowed us to measure spectra over a wide range of proton velocities (ie: over a wide range of relative electron-proton arrival times) without altering the timing of the electronics.

2. It allowed acquisition of coincidence events and a prescaled fraction of single-arm events interspersed during the run. The prescaled fraction of single-arm events refers to acquiring one out of every 2^n single-arm events where n is chosen by the experimenter. Prescaling allowed us to monitor the behavior of the individual spectrometers independently of the coincidence yield while simultaneously acquiring coincidence data.

3. It was independent of the nature of the single arm triggers. The coincidence trigger module could be used by any pair of spectrometers used in coincidence (e.g. MEPS and OHIPS of [5]).

4. It had pile-up monitors to veto possibly corrupt events in software. I discuss pile-up in Chapter 3.

5. It had one per beam burst limiters. The CAMAC system could not handle more than one event per beam burst.

6. It allowed easy switching from purely single-arm acquisition to coincidence and single-arm acquisition. This feature proved useful when changing from single-arm normalization measurements to coincidence measurements.

7. It allowed easy changing of the coincidence timing.

8. It scaled all logic decisions for ease of reconstruction and normalization in software.

There were two inputs to the coincidence trigger, the ELSSY single-arm trigger and the OOPS single-arm trigger.

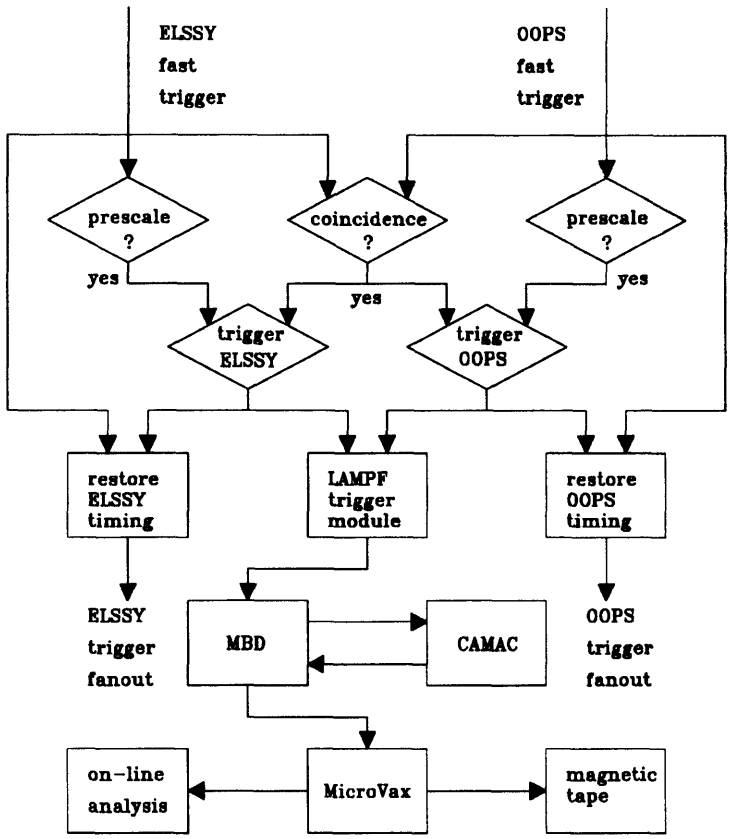

Figure 2-13: Data acquisition logic flow.

The coincidence trigger module produced many outputs:

1. The CAMAC LAM[1] to read out CAMAC,

2. An ELSSY trigger and an OOPS trigger to trigger (provide gates and starts for) the ELSSY and OOPS electronics,

[1]LAM stands for 'Look At Me' and is the flag set by CAMAC when it has data and it wants to be read out.

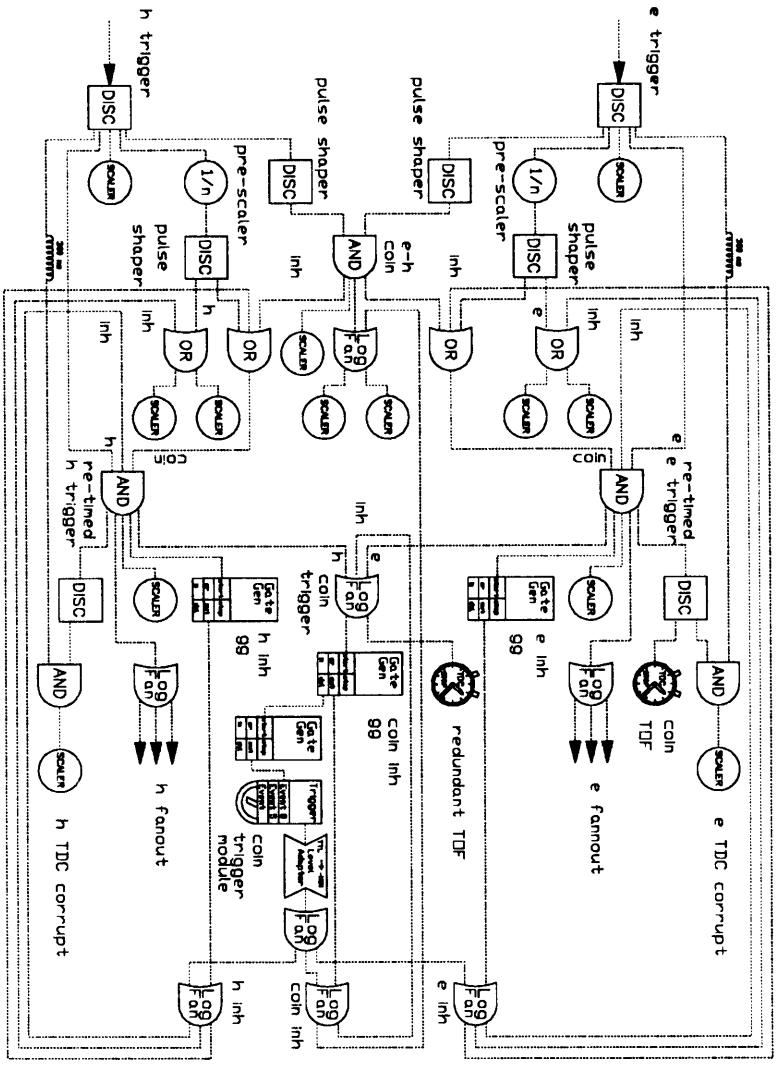

Figure 2-14: Coincidence Trigger Module electronics.

3. event scaler inputs to label the event as a combination of coincidence, ELSSY prescaled and OOPS prescaled events,

4. event scaler inputs to label the event as a ELSSY or OOPS pileup event,

5. Start (ELSSY) and stop (OOPS) signals to the ELSSY-OOPS relative time TDC (the Coincidence Time-Of-Flight TDC [CTOF]), and

6. Inputs to many CAMAC and visual scalers.

2.5 Data Acquisition and Experimental Control

We acquired the data event by event using CAMAC based ADCs, TDCs, and scalers interfaced to a microVAX via a Microprogrammable Branch Driver (MBD). When CAMAC sends a LAM, the MBD reads the data from the CAMAC modules and transferred the data to the microVAX memory. We used the Q system for both data aquisition and data analysis [37], The microVAX wrote the data to tape and, in the available time before the next event, performed on-line histogramming and analysis of events.

2.5.1 Structure of the Event Data

The microVAX acquires data from the MBD and writes them to tape event-by-event. In our case, each event consisted of 73 raw data words, these being the ADC and TDC readings for each event, as well as event scaler readings (coincidence event or not, prescale event or not etc.). There were also some 300, or so, calculated data words for each event. These were derived online from the raw data by the analyzer [38] after the raw data were written to tape. This was done for purposes of on-line display, debugging, and analysis. These calculated data words included such things as wire chamber spectra and missing energy spectra.

2.5.2 On-line Analysis

After acquiring data and writing it to tape, Q processed as many events as possible. The analyzed fraction was typically 97–99%. The analyzer provided statistics of all the CAMAC scalers both as absolute numbers and as per-beam-burst numbers. The analyzer created histograms of ADCs and TDCs and analyzed the wire chamber data, creating position and angle histograms ($x_f, y_f, \theta_f, \phi_f, \theta_t, \phi_t$) for both ELSSY and OOPS. It also provided diagnostic information for the wire chambers such as chamber deadtimes and efficiencies. For coincidence events, the analyzer created a Coincidence Time-Of-Flight (TOF) spectrum as well as missing energy spectra for user-defined Reals and Accidentals windows in the TOF spectrum. This allowed real time monitoring of coincidence yields and cross-sections during the experiment.

2.5.3 Experimental Control

Data taking was controlled by Q. The spectrometer magnets were controlled and monitored by readouts upstairs. A Rawson and an NMR probe monitored the ELSSY fields, while the OOPS magnets were monitored by current readouts. We used individual power supply controllers for each spectrometer magnet (two ELSSY dipoles, one OOPS dipole, and one OOPS quadrupole). The target ladder was controlled by a separate computer. This computer could put a specified target in the beam at a specified position. It could also change the angle of the target. It did not communicate with the microVAX.

Chapter 3

Data Analysis

The data analysis in this experiment involved replaying the data written to tape by the Q system. First, our purpose was to understand the performance of each spectrometer by constructing position, momentum, and angle spectra in each spectrometer. Second, we needed to find normalizations for each spectrometer and a method of determining single arm efficiencies in ELSSY and coincident efficiencies for OOPS–ELLSY. Third, we needed to determine the Deuterium content of our solid CD_2 target as accurately as possible, and understand how this varied during the experiment. Fourth, we needed to know our beam energy as accurately as possible. Once all this was done, we proceeded to extract coincidence cross sections and structure functions from our missing energy and momentum spectra.

The above overview of our analysis represents a very great consolidation of detail. The following chapter will lay out most of it, while pointing the reader to references if he/she needs more detail on certain topics.

3.1 ELSSY Analysis

In this section, I will explain how we took the raw ADC and TDC information from the ELSSY focal plane instruments and obtained focal plane position, momentum, and angle spectra. I'll then discuss what constituted an ELSSY 'good' event (i.e., an event that we were able to analyze) and how we scaled the number of these events back up to the number of 'real' events (i.e., an event from the reaction we were measuring). The number of real events is what goes into the cross section calculation.

3.1.1 The ELSSY Trigger

In replay, the ELSSY trigger was the meantimed AND of the two scintillators ANDed with an AND between the Cerenkov counter and the lead glass array. The Cerenkov–lead glass OR of chapter 2 was only during data acquisition. Meantimed refers to the fact that our trigger involved the coincidence of the two phototubes (one per scintillator, see fig 2.3) but came at a time τ

where

$$\tau = \frac{t_l + t_R}{2} + \text{ offset} \tag{3.1}$$

Where t_L and t_R are the arrival times of TDC signals coming from the left and right phototubes respectively. This was then combined with Cerenkov/Lead block ADC cuts for particle identification.

The Cerenkov was used to eliminate pions from the ELSSY trigger. Pions of similar momentum to our electrons would have a reduced velocity due to their much greater mass. They would emit radiation at a greater angle relative to flight path than the electrons, and thus would fail to fire the Cerenkov phototubes.

The Lead glass blocks were not really needed in this experiment. They are normally necessary for the elimination of high energy, non-target related muons (i.e., cosmics) from the ELSSY trigger. Unlike the pions, these particles may have sufficient velocity to fire the Cerenkov due to their relatively high energy ($\sim$ 100 GeV). The Lead Glass was designed to distinguish these cosmics from electrons by how much energy each deposits. However, since our experiment is coincidence detection of an electron and proton from the same scattering event, these cosmics will only form an accidental coincidence, which we can separate from genuine target-related events (see section 3.7). Nonetheless, since it made little difference in the number of data counts, and for the sake of being as accurate as possible, we made the ELSSY replay trigger contain a Cerenkov–lead glass AND rather than an OR.

3.1.2 The ELSSY VDC

The ELSSY VDC code was modified for this data analysis in order to correct for several troublesome effects. A detailed discussion of these effects and how the code was modified to correct for them can be found in [39]. I will give a less detailed accounting of what the code does. The following subsections then take us from raw TDC values to the final reconstructed track.

Wire Numbers, Drift Times, and Electron Flight-Time Corrections

Section 2.3.4 tells how we obtain a wire number and a drift time for each of the three delay lines. $t_L - t_R$ is related to the wire number, while $t_L + t_R$ is related to the drift time.

In addition, since the VDC is sloped at 45° relative to the scintillators, we must apply a flight-time correction to the drift times. This slope means that the high-momentum end of the VDC will be 40 cm closer to the scintillator pair than the low-momentum end (see figure 3.1).

This translates to a 1.5 ns earlier start for the high-momentum events as compared to the low-momentum ones. Relative to the center of the VDC, drift-times at the high-momentum end will shift to larger values (since the start signal to the TDC's comes earlier) while drift-times at the low-momentum end will shift to smaller values.

We correct for this by adding Δt to the drift-time where

$$\Delta t = X_{\text{wire}} - 2 \cdot \frac{\sin 45^\circ}{c} \tag{3.2}$$

This removes the position dependent shift in the VDC drift-time.

The Drift-Time to Drift-distance Conversion

Once we have proper drift-times, we are ready to obtain drift-distances. Figure 3.1 shows a typical drift time histogram for one of the VDC delay lines.

Notice that there exists a flat and a peaked region. The flat region, or plateau, cor-

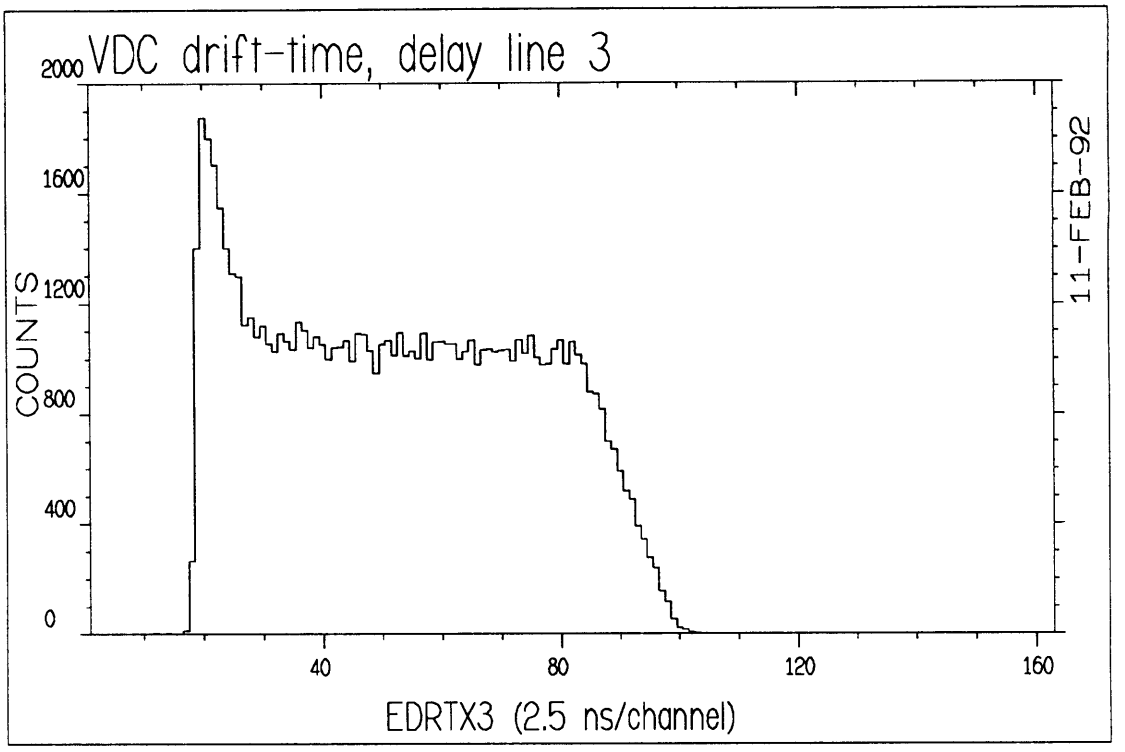

Figure 3-1: A good ELSSY drift time spectrum

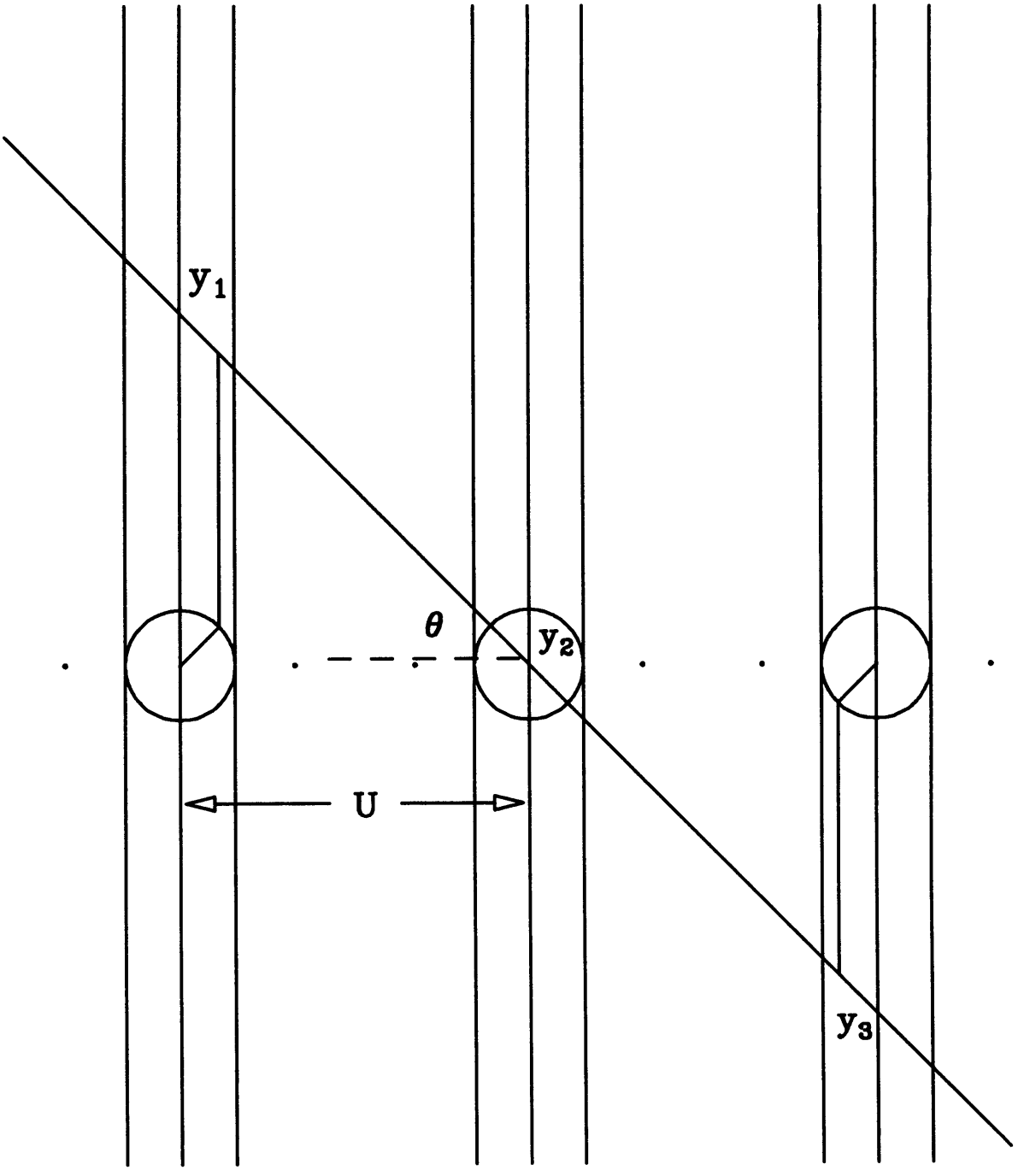

Figure 3-2: Cross section of VDC showing the 3 drift-distances. The circles correspond to the non-linear drift region close to the wire.

responds to the region of the drift cell where the field is uniform and the drift-speed is constant (the region outside the circles in the drift cells of fig. 3.2).

The peaked region corresponds to the region of the drift cell closer to the wire where the field becomes non-uniform and the ions accelerate toward the wire (the region inside the circles of fig. 3.2). It is known that the drift velocity in the flat region is 50 μm/ns. This is specific to our gas mixture and voltage.

If we uniformly illuminate the drift cell with particles, we can write the following:

$$\frac{dN}{dt_d} = \frac{dN}{dy}\frac{dy}{dt_d} = \frac{dN}{dy}v_d \tag{3.3}$$

where $\frac{dN}{dy}$ is the number of particles per unit length along the drift cell and is constant (uniform illumination),$\frac{dN}{dt_d}$ is the number of particles per unit drift time in the cell (fig. 3.1), and $\frac{dv}{dt_d} = v$ the local drift velocity.

But since $\frac{dN}{dy}$ is constant we may solve for it in the plateau region

$$\frac{dN}{dy} = \left(\frac{dN}{dt_d}\right)_{\text{plateau}} \cdot \left(\frac{1}{v_d}\right)_{\text{plateau}} \tag{3.4}$$

and we took

$$\frac{dN}{dy} = \left[\frac{dN}{dt_d}\right]_{\text{plateau}} \cdot \left(\frac{1}{50\mu\text{m/ns}}\right) \tag{3.5}$$

Now we're ready to generate a lookup table to go from drift-time — what we measure, to drift-distance — what we want to know:

$$\int_0^{t_d} dy = y(t_d) = \frac{1}{\left[\frac{dN}{dt_d}\right]_{\text{plateau}} \cdot \left(\frac{1}{50\mu\text{m/ns}}\right)} \int_0^{t_d} \frac{dN}{dt} dt \tag{3.6}$$

Our final result is the drift-distance histogram of figure 3.3. We see that the drift cell is filled uniformly, which was our original assumption.

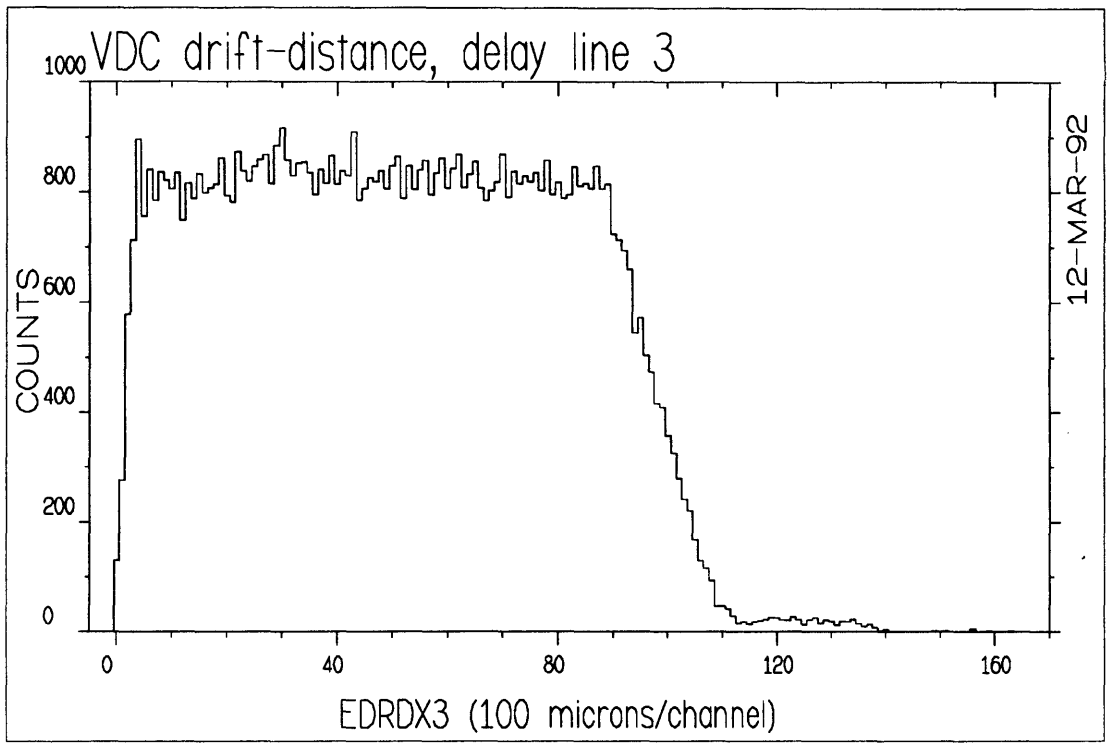

Figure 3-3: A good ELSSY drift distance spectrum

Track Reconstruction

Now we have three (hopefully) wire numbers and three corresponding drift -distances for a particle passing through the VDC. We can now determine x_f and θ_f for the event.

To get x_f we use the following algorithm from [30]

$$X_f = X_{\text{wire}}(2) + \frac{Z_1 - Z_3}{2(Z_> - Z_2)} \tag{3.7}$$

where Z_1, Z_2, and Z_3 are the three drift-distances corresponding to wires 1,2, and 3. $X(i)_i = 1,2,3$ are the wire positions measured along the VDC, and

$$Z_> \equiv \max(Z_1, Z_3) \tag{3.8}$$

To get θ_f we must correct for something we call the "Schmitt effect" or "angle-dependent drift-distance effect" [17]. Figure 3.4 illustrates this problem. The drift distance we get from our lookup table is the pathlength along the field lines, i.e., a path perpendicular to the wire plane until the ion reaches the non-linear region (the semi-circle) of the drift cell. Then the ion avalanches to the wire along a radial path. The drift-distance from the lookup table is the sum of these two paths. Notice from figure 3.4 that particles having the same drift-distance from the lookup table can have different intercepts with the Y-axis. But this Y intercept is what we have drawn in figure 3.4! So we see that the "real" drift-distance depends not only on the drift-time but also on the inclination of the track, i.e., θ_f. The "Schmitt correction" is then a θ_f dependent drift-distance correction. The Schmitt-corrected θ_f is

$$\theta_f = \cos^{-1}\left[\left[\frac{-yz + \sqrt{1 + y^2 - z^2}}{(1 + y^2)}\right]\right] \tag{3.9}$$

where

$$y = \frac{Z_1 + Z_3 - 2R\text{sec}\theta_0}{2U} \tag{3.10}$$

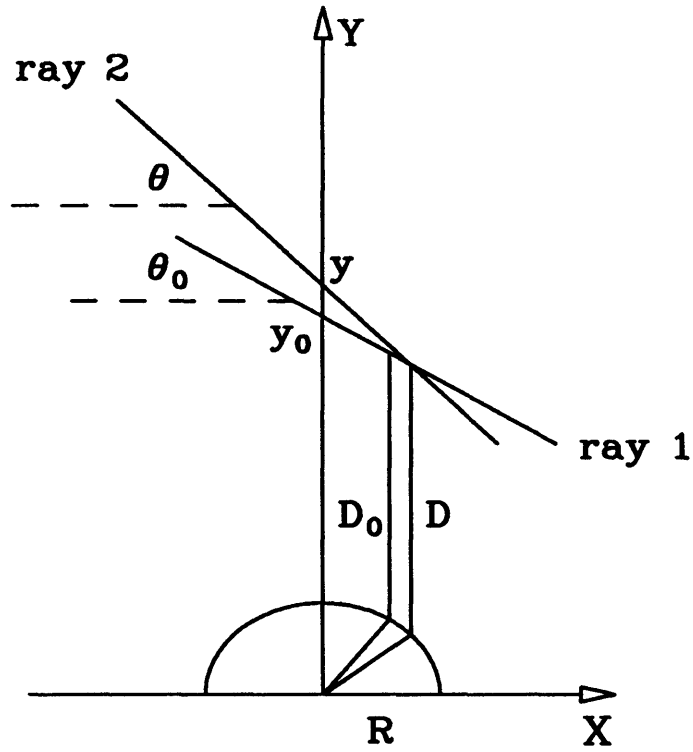

Figure 3-4: Illustration of the Schmitt effect.

and

$$Z = \frac{R}{U} \tag{3.11}$$

where

R = radius of the non-linear drift region

U = distance between neighboring wires (fig.3.2)

The corrected drift distances are then

$$y' = y + R(\sec\theta - \sec\theta_0) \tag{3.12}$$

and R and θ_0 are chosen so as to minimize the χ^2 of the track determined by the corrected drift distances fitted to a straight line.

VDC Irregularities-θ_f Correction

When θ_f is histogrammed vs. x_f (fig. 3.5), it can be seen that there are periodic dips in θ_f. It is not clear why this occurs. From measured optical properties of ELSSY, we expect a smooth linear relation between these two variables. Spectrometer aberrations are unlikely to cause this. The vertical slits for this histogram are at 3.76 inches, as opposed to 10 inches nominally. Thus, the range of particle trajectories is small enough that no significant spectrometer aberrations should affect the θ_f distribution as a function of x_f.

The only other explanation would then be either irregular construction of the VDC or non-uniformity of the readout electronics. Either one of these being the case, we decided it would be reasonable to remove these x_f-dependent bumps in replay.

Therefore, we took many slices in x_f and found their centroid in θ_f. We then fit a line to these centroids. Then we took the difference between the line and the measured centroid. This gave us an x_f-dependent correction to the value of θ_f. We added this correction to the observed θ_f to get our final answer for 'actual' θ_f. Figure 3.5 also shows the corrected histogram. Notice that the bumpiness has disappeared, making the x_f-θ_f relation look smoother and thus more physically reasonable.

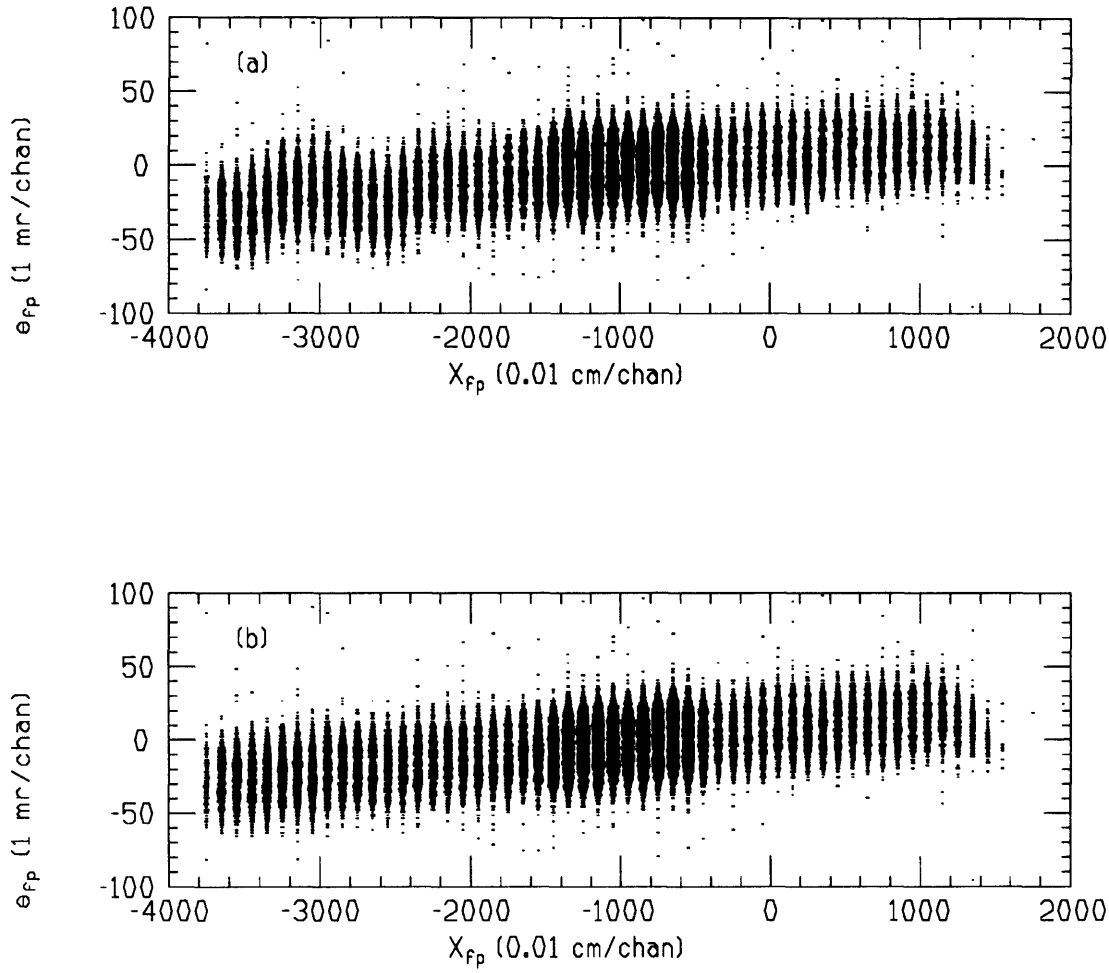

Figure 3-5: Two θ_f vs. x_f plots, the top plot is without corrections, the bottom plot contains corrections that smooth the distribution.

3.1.3 The ELSSY Transverse Arrays

These HDC's made possible our y_f and ϕ_f determination for each event. Figure 3.6 shows how the wires in the four TA's were offset with respect to each other. When the electron came through the TA, it would fire the nearest wire. The corresponding drift-distances for wires fired in the two planes of the same chamber would then give the position reading in that chamber, the electron passing between the fired wires. Ideally, all four planes would fire and the ϕ_f and y_f would be the slope and first wire plane intercept of the line fitted to the four drift distances. If only one TA fired then y_f was taken as

$$y_f = \frac{1}{2}\left[Y_{\text{wire}}(1) \mp d_1 + Y_{\text{wire}}(2) \pm d_2\right] \tag{3.13}$$

and θ_f was taken as

$$\theta_f = \tan^{-1}\left[\pm\frac{(d_2 - G + d_1)}{D}\right] \tag{3.14}$$

where Y_{wire} (1) is the position of the fired wire in the first plane, Y_{wire} (2) the position of the fired wire in the second plane, G is one half the wire spacing in a single TA plane, D is the vertical distance between wire planes in a chamber, and the top signs are taken in equations 3.11-3.12 if the particle passed to the left of the wire in plane 1 of figure 3.6 while the bottom signs are taken if the particle passed to the right of the wire in plane 1. Of course, similar equations are used if only the second TA (planes 3 and 4 of figure 3.6) fires.

Notice that since ELSSY was designed so that ϕ_f for events would be zero (within resolution), the track of the particle was perpendicular to the wire plane. This meant that our left-right decision in the TA's was unambiguous, since the two drift-distances in each chamber for each event had to add up to one-half the wire spacing in a single plane (see fig. 3.6). Drift-distance pairs that didn't add up to one-half the wire spacing, plus some resolution, were thrown out (section 3.1.4).

3.1.4 The ELSSY 'Good' Event

In summary then, for each event the VDC and TA analysis routines do the following:

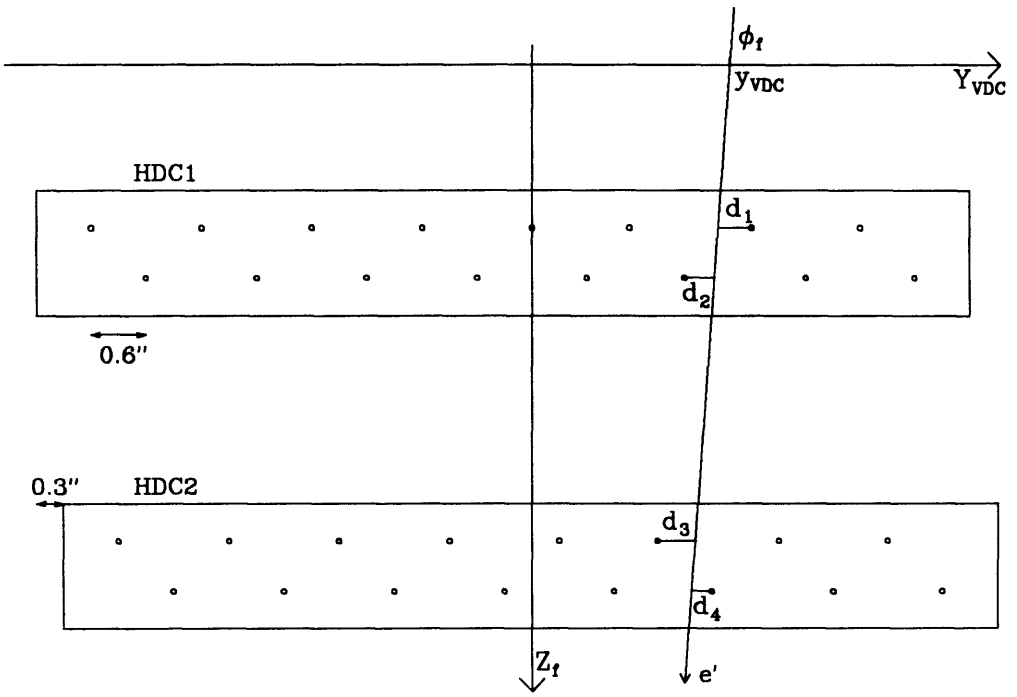

Figure 3-6: Diagram of the 4 wire planes of the Transverse Arrays.

1. they convert the raw delay line TDC values to wire numbers and drift times,

2. they convert the drift times to drift distances, and,

3. after making appropriate corrections, they convert these drift distances to focal plane coordinates $(x_f, y_f, \theta_f, \phi_f)$.

Events are divided into two classes:

1. 'noise' events where no reaction related particle passed through the chambers, and

2. 'real' events where a reaction related particle passed through the chambers.

Real events are further divided into two classes:

1. 'bad' events that do not have reconstructible trajectories in the wire chamber, and

2. 'good' events with fully reconstructible trajectories in the wire chamber.

Noise events are separated from real events by the method of section 3.1.6. Good events are selected with the following criteria:

1. the VDC delay lines TDC's yield three adjacent wires having positions within the range of the VDC

2. The VDC event must not involve the last wire on the low momentum side of the VDC (see fig. 2.3). This event might correspond to a single sign hit pattern (fig. 3.7). Our algorithm, equation 3.7, doesn't work for these types of hit patterns so we chose to eliminate all events from this wire.

3. the ratio $\frac{D_1+D_2}{D_>-D_2}$ shall be 2 plus some resolution for the VDC, corresponding to the acceptable $++-$ and $+++$ events of figure 3.7.

4. the VDC intercept, x_f, must be within the range $\pm$ 40cm, a cut just outside the physical boundaries of the VDC

5. the reconstructed angle at the target in the bend direction, θ_T, must be within range $\pm$ 100mr, a 1% cut on the tails of the θ_T spectrum (section 3.4 discusses how we transformed from focal plane coordinates in OOPS and ELSSY to target coordinates)

6. the adjacent TA plane drift distances must add to one-half the wire spacing in at least one of the two TA chambers

7. the angle at the target in the transverse direction, θ_T, must be within range $\pm$ 15mr, also a 1% tails cut, and

8. the event must have δ within range of the ELSSY scintillators. Where

$$\delta = \frac{p - p_c}{p_c}$$

Thus, δ is the fractional deviation of the particles momentum from the central momentum setting of the spectrometer. Notice from figure 2.2 that particles with too steep a bend angle at the target begin to miss the scintillators if delta is higher than a certain cutoff. We chose the delta limits to be $-3.5\% < \delta < +1.1\%$, the upper value being this cutoff.

3.1.5 The ELSSY Deadtime

The ELSSY deadtime consists of two terms:

1. the data acquisition deadtime,

2. the pileup correction.

Perhaps a clearer explanation is given in terms of a 'livetime'. Once this is understood, the corresponding deadtime is simply the livetime subtracted from 1. I'll use livetime for the rest of this thesis.

So then, the ELSSY data acquisition livetime is the number of ELSSY events on tape divided by the number of single arm triggers in ELSSY.

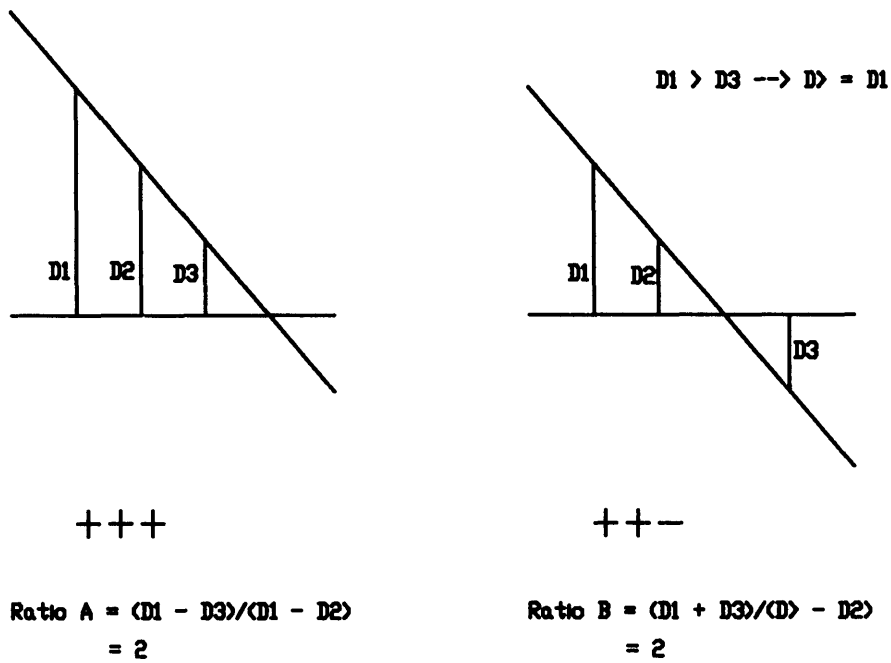

Figure 3-7: Acceptable wire hit patterns in the VDC.

In addition, if any other ELSSY events occurred within a 195 ns window of a given ELSSY event, the event was labeled as 'pileup.' In order to avoid possible contamination of the VDC, whose maximum drift time is about 240 ns, no pileup events were analyzed. The ratio of ELSSY prescale events (see section 2.4.1 for a definition of 'prescale') without pileup to all ELSSY prescale events was then used as another livetime correction run by run.

Our total ELSSY livetime was then

$$e\_lt = (e\_lt_{DAQ}) \left(e\_lt^{\text{prescale}}_{\text{no pileup}}\right) \tag{3.15}$$

We divided all ELSSY spectra counts by this number to get the 'real' number of counts.

3.1.6 The ELSSY Efficiency

Not every ELSSY hardware trigger corresponded to a 'real' ELSSY event. Nor did it always correspond to a 'good' or analyzable event. This meant we had to determine what percentage of the unanalyzed hardware triggers were 'bad' in that they corresponded to a 'real' event (section 3.1.4) and what percentage were 'noise' events. To do this we used the method of Doug Beck and Karen Dow [40] [41].

This method consists of measuring an elastic cross section in ELSSY and then making successive cuts on the peak, keeping track of how many events are lost at each cut. For example, figure 3.8 shows a 'good' spectrum. Figure 3.9 shows this same spectrum where the condition in the first test description box of table 3.1 is relaxed. Notice that there are still small peaks visible. We then consider the background subtracted counts in these small peaks to be 'real' events and add them to the number of counts in the peaks of figure 3.8 as a running total of 'real' events. We then do the same procedure with the other tests listed in table 3.1, adding real events to the total after each test is applied. This then gives a final correction factor to the counts obtained from figure 3.8. Remember, the events in the peak of figure 3.8 are all 'good', whereas the counts in the peaks of the other figures are all 'bad'. The 'real' counts are those that go into the cross section calculation and these are made up

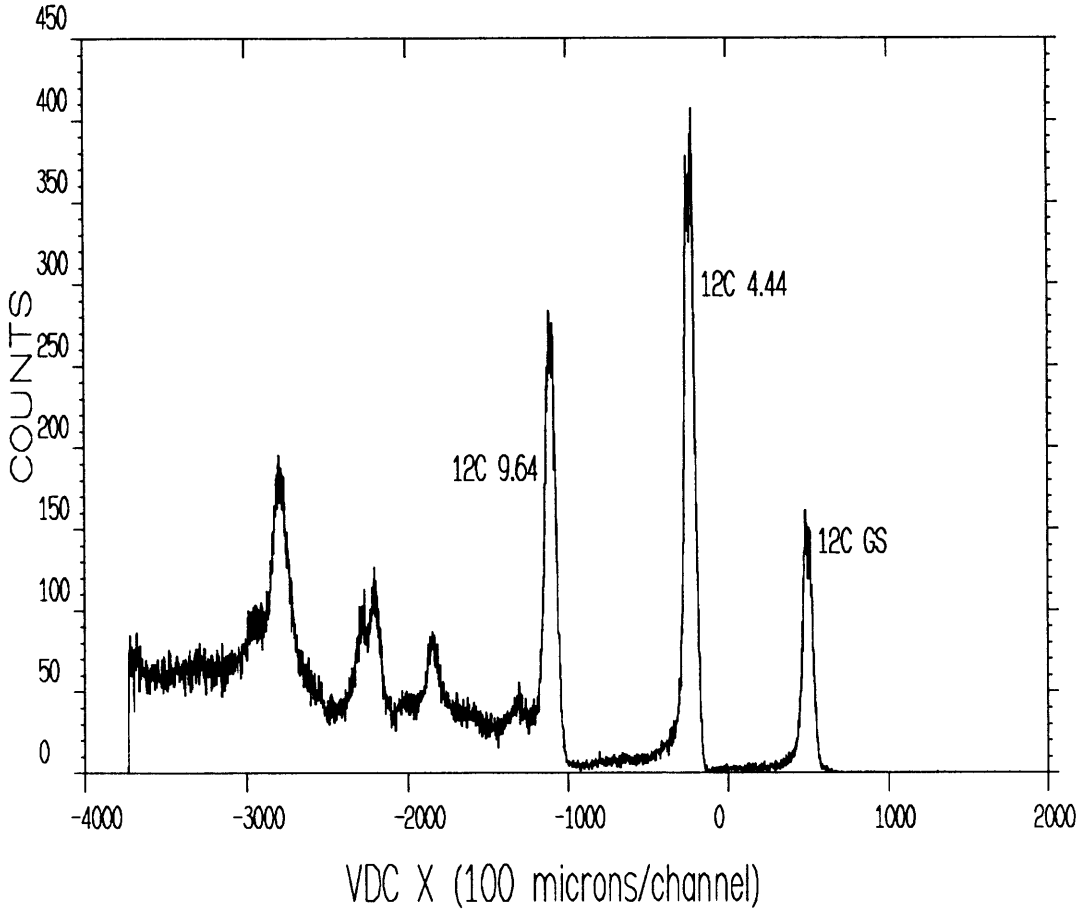

Figure 3-8: For ELSSY efficiency determination, a 'good' Carbon spectrum.

of the 'good' and the 'bad' counts (section 3.1.4).

We used this procedure to find the efficiencies in order to determine single arm cross sections in ELSSY.

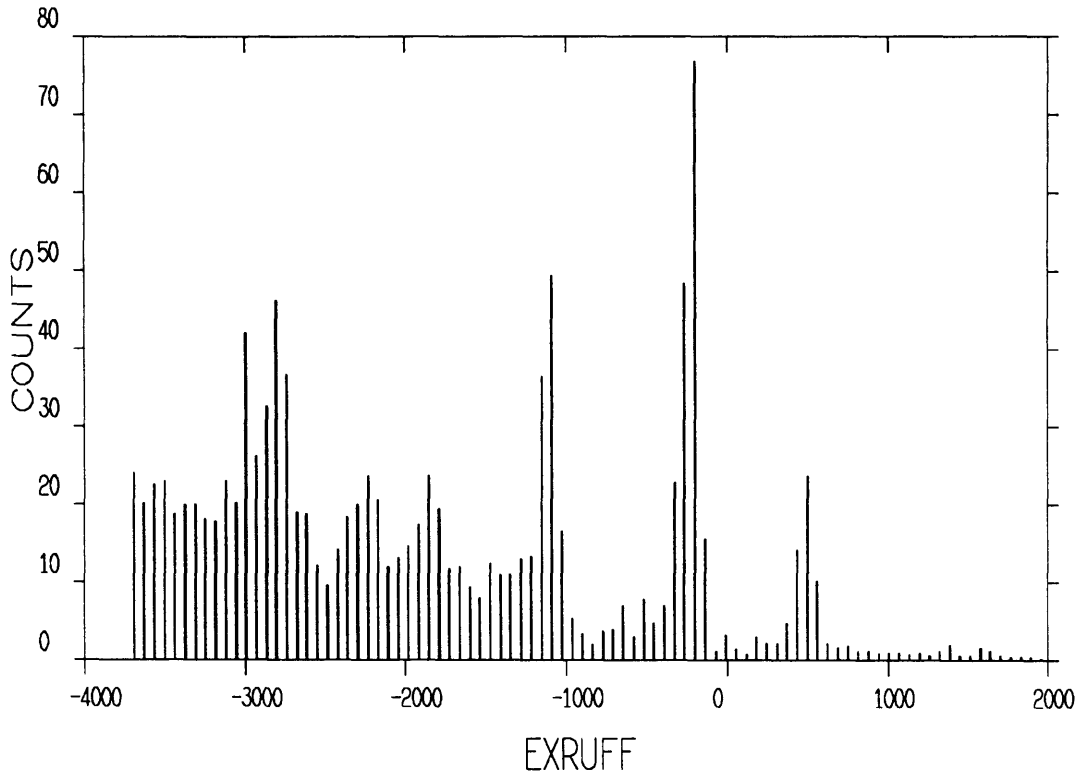

Figure 3-9: A Carbon spectrum with one of its 'good' criteria relaxed. Events that increment the histogram are then 'bad' events.

histogram name	test description	typical % real events lost
EXRUFF	$\frac{D_1+D_2}{D_>-D_2}$ not equal to 2 (section**)	1.5
EXISDL	first or last VDC wire not adjacent to other two	1.0
EXIMDL	middle VDC wire missing	< 0.5
EXNOTA	neither TA 1 or 2 had good drift sum	< 0.5
EXBAD	one of the trigger ADC's out of range	< 0.1
EXTOR	one of the target variables out of range	< 0.1
EX50F6	same condition as EXISDL except one of the 6 delay line TDC's is missing	< 0.1

Table 3.1 ELSSY Histograms and Tests.

A different method was used for the OOPS-ELSSY coincident efficiency that involved use of the time of flight spectrum (section 3.7.4). The OOPS-ELSSY coincident efficiency was the efficiency used for extraction of the $D(e,e'p)$ cross sections.

3.1.7 The ELSSY Normalization

So far we have discussed how we accounted for real events that formed a hardware trigger but could not be analyzed for one reason or another. Real events that did not form a hardware trigger also had to be accounted for. These events were lost due to scintillator or Cerenkov inefficiency, or to some other small effect. We corrected for them with a normalization factor. The remainder of this section explains how this normalization factor was obtained.

Before we go on, it should be meantimed that the discussion of the rest of this section assumes that the ELLSY focal plane efficiency profile is flat. That is, the efficiency of every part of the focal plane as a function of delta is just as efficient as any other part. We assume this is true since the ELSSY slits shrink its angular acceptance well below the point that we would lose events having too large a target angle in the bend direction. In section 3.3, we show that this assumption is correct. See this section for a discussion of how the focal plane efficiency is determined.

To get the overall normalization of ELLSY, we first measured the hydrogen (e,e′) elastic peak in ELSSY using a CH_2 target. then used the peak fitting program ALLFIT to fit the spectra and determine cross-sections [42]. Next, we adjusted this cross section using information about ELSSY wire chamber efficiencies and dead times to give the final answer. Finally, we compared this cross section with that obtained from a parameterization of H (e, e′) elastic scattering at MAINZ [43]. Figure 3.10 shows the ratio $\frac{H(e,e')\mathbf{ELSSY}}{H(e,e')\mathbf{MAINZ}}$ for each of our H (e,e') runs. If we average all of these together we get $\frac{H(e,e')_{\mathrm{ELSSY}}}{H(e,e')_{\mathrm{MAINZ}}}$. Our ELSSY normalization factor was then $N_{\mathrm{ELSSY}} = \frac{1}{.979} = 1.0222$ and we multiplied our D(e,e′p)cross sections by this number.

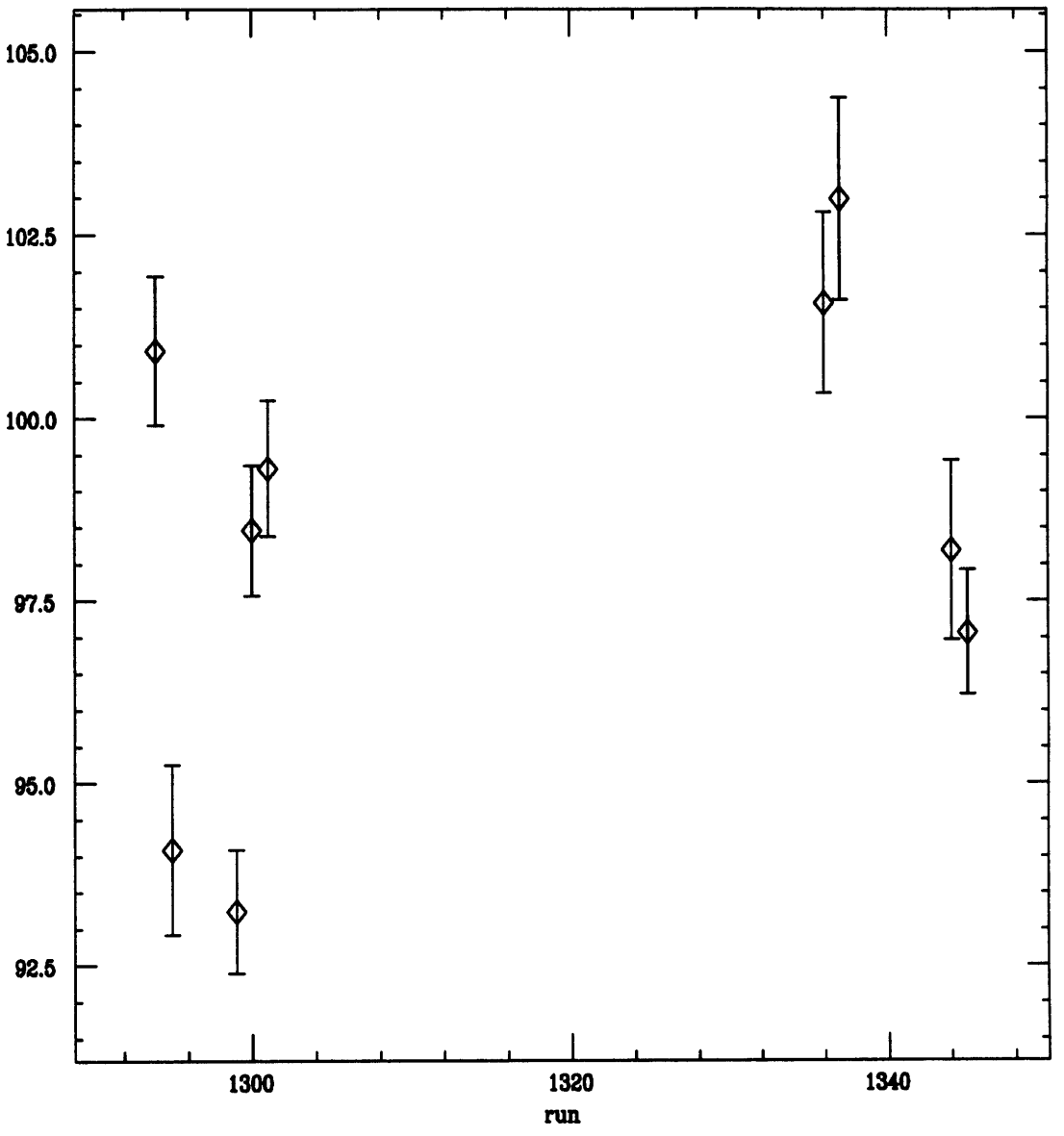

Figure 3-10: The ratio $\frac{H(e,e')_{\mathbf{ELSSY}}}{H(e,e')_{\mathbf{MAINZ}}}$ in % plotted versus run number.

3.2 OOPS analysis

Analysis of events in OOPS consisted of getting particle identification from the OOPS scintillators, reconstructing the proton track from the information obtained from the six HDC planes, and determining the focal plane efficiency profile.

3.2.1 The OOPS HDC

For each event, the OOPS HDC analysis code does the following:

1. it converts the twelve raw delay line times (one delay line per wire plane, two ends per delay line) to wire numbers and drift times using the same algorithms as the ELSSY VDC and TA,
2. it converts the drift times to drift distances (see section 3.2.1 for more details),
3. it fits a track to the set of two or three drift distances in the X and Y chamber, and,
4. it converts the tracks in the chambers to the focal plane coordinates $(x_f, y_f, \theta_f, \phi_f)$,

Good delay line difference, drift time and drift distance spectra are shown in figures 3.11-3.13.

The OOPS HDC Drift-Time to Drift-distance Conversion

For OOPS, we used the program DRT to get a drift-distance lookup table from the drift-time histograms [44]. DRT assumes flat illumination of the OOPS HDC drift cell. We therefore input to it a flat or 'white' wire chamber spectrum. It then solves for the drift speed as a function of distance from the wire when given the corresponding drift-time histogram (fig. 3.12). It then creates a lookup table for drift-distance y_d given the drift-time t_d. Following from equation 3.3 we then have

$$y_d = y(t_d) = \frac{1}{\left[\frac{dN}{dy}\right]} \int_0^{t_d} \frac{dN}{dt} dt \ , \tag{3.16}$$

and we have our table.

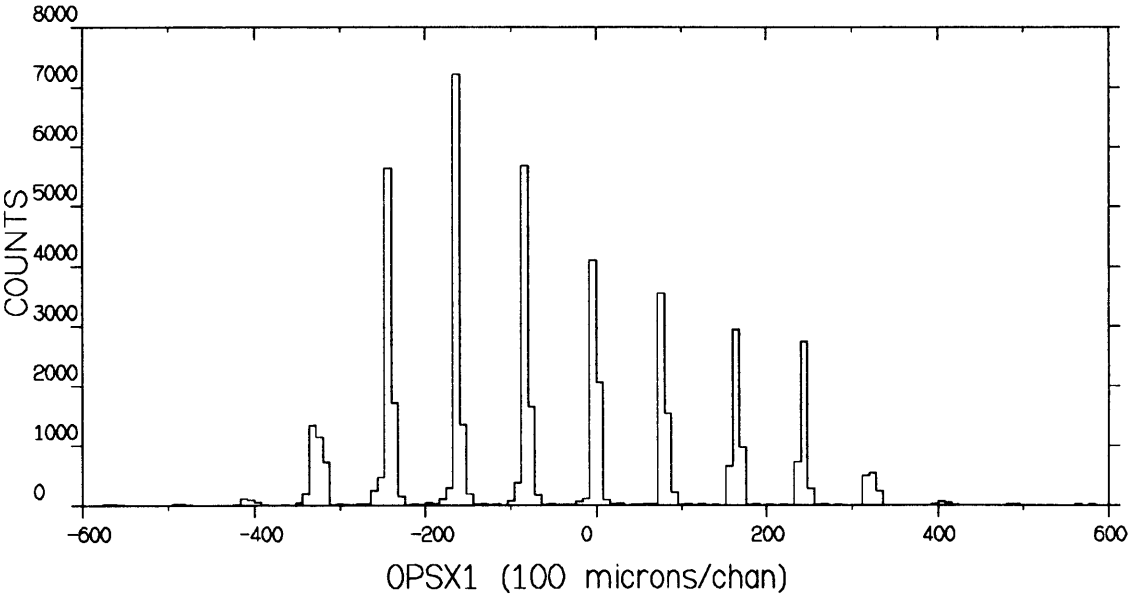

Figure 3-11: A good OOPS wire spectrum.

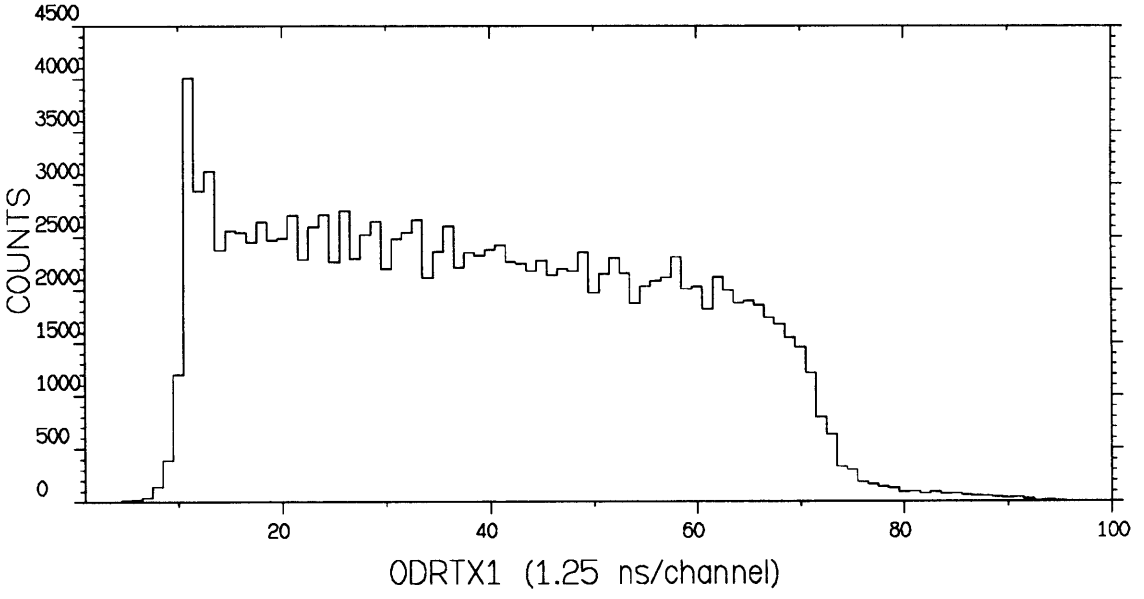

Figure 3-12: A good OOPS drift time spectrum.

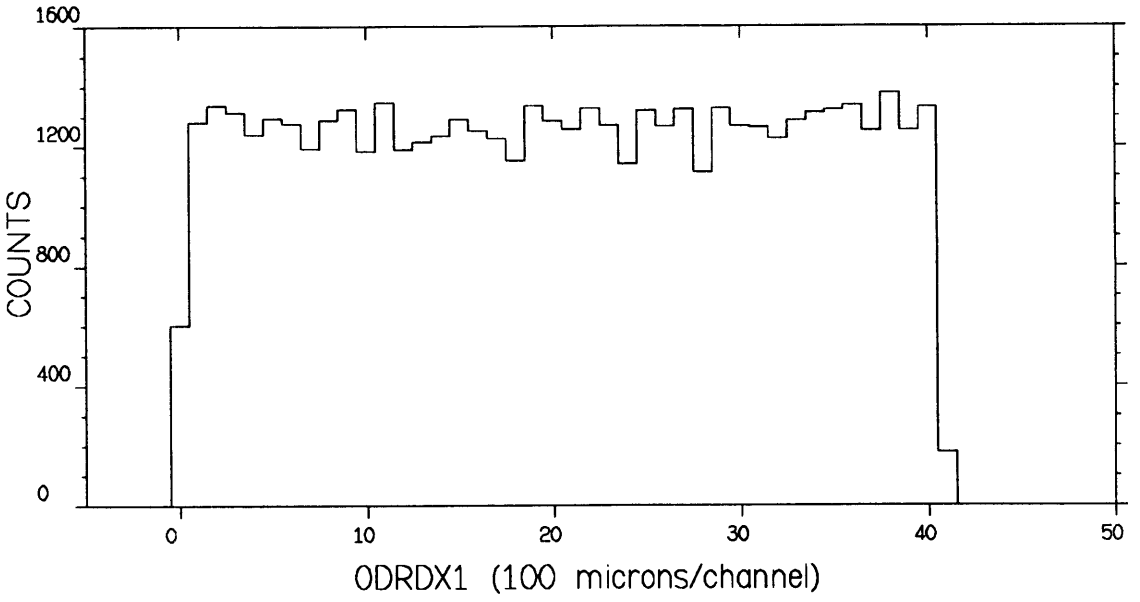

Figure 3-13: A good OOPS drift distance spectrum.

3.2.2 The OOPS Scintillators and Trigger

For OOPS, the trigger was the AND of all three scintillators. The timing of the trigger was determined by the meantimed middle scintillator, S2.

The OOPS scintillators had the ability to distinguish between pions and protons in software as shown in figure 3.14. However, we found it unnecessary to cut pions from the coincidence trigger using this information, as our energy transfer for D(e,e'p)events was below pion creation threshold.

3.2.3 The OOPS Livetime

The OOPS livetime consists of two terms:

1. the data acquisition livetime,

2. the pileup correction.

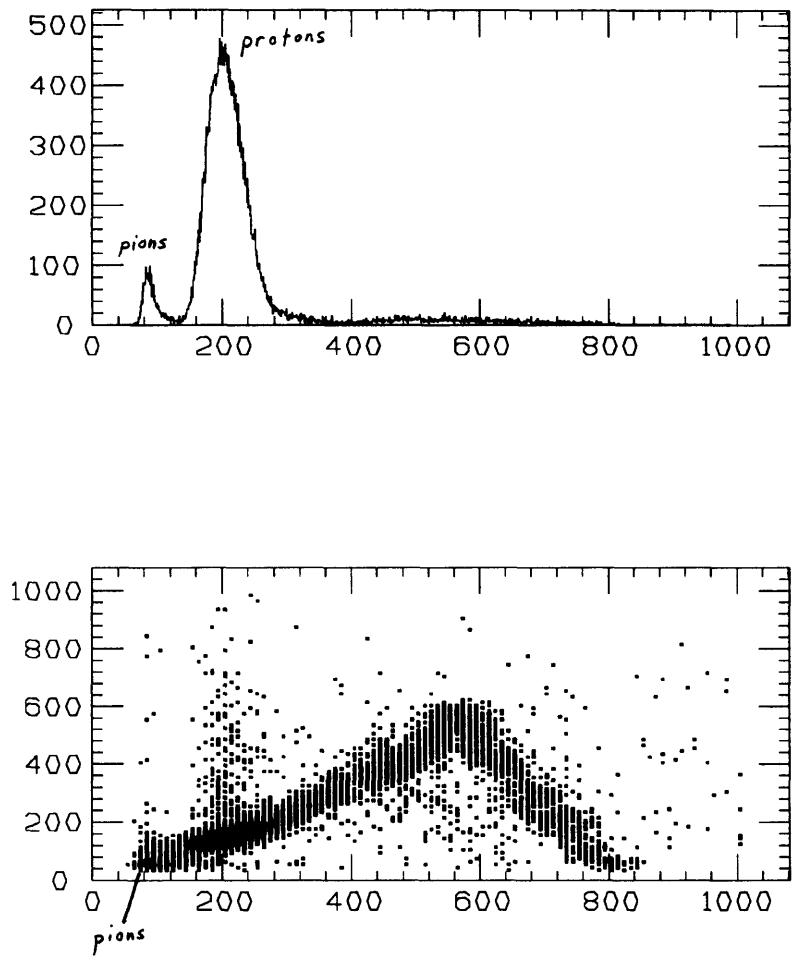

Figure 3-14: A plot of OOPS scintillator 2 (top) and of OOPS scintillator 2 vs. 3 (bottom). The differential energy loss of pions and protons enables particle identification.

The data acquisition livetime was the number of OOPS events on tape divided by the number of single arm triggers in OOPS.

The pileup correction was the ratio of OOPS prescale events without pileup to all OOPS prescale events. Our total OOPS livetime was then

$$h\_lt = (h\_lt_{DAQ}) \left(h\_lt^{\text{prescale}}_{\text{no pileup}}\right) \tag{3.17}$$

We divided all OOPS spectra counts by this number to get the 'real' number of counts in OOPS.

3.2.4 The OOPS Trigger Deadtime

There existed a small inefficiency in our OOPS trigger electronics. We lost some triggers due to the length of the delay in our circuit. This was discovered by J. Mandeville and studied extensively by him and by M. Holtrop. This was about a 1% effect, which we corrected for with a formula. This formula and a detailed description of the problem can be found in the back of [50].

3.2.5 OOPS Efficiency

When needed, single OOPS efficiency information was obtained with H(e,e'p) by detecting an electron in ELSSY and looking for the corresponding proton in OOPS. This was important for determination of the OOPS normalization, described in the next section.

3.2.6 OOPS Normalization

To get the overall normalization of OOPS, we measured H(e,e'p) with OOPS and ELSSY. This was done as part of our R_L/R_T separation measurements.

We wanted to see every coincidence proton. Thus, the ELSSY slits were set so that the full ELSSY angular acceptance would produce a column of protons having an angular acceptance smaller than the OOPS acceptance. Then, every missing proton was due to inefficiency, not geometry. We then ran the program REVMOC [45] to get what we be-

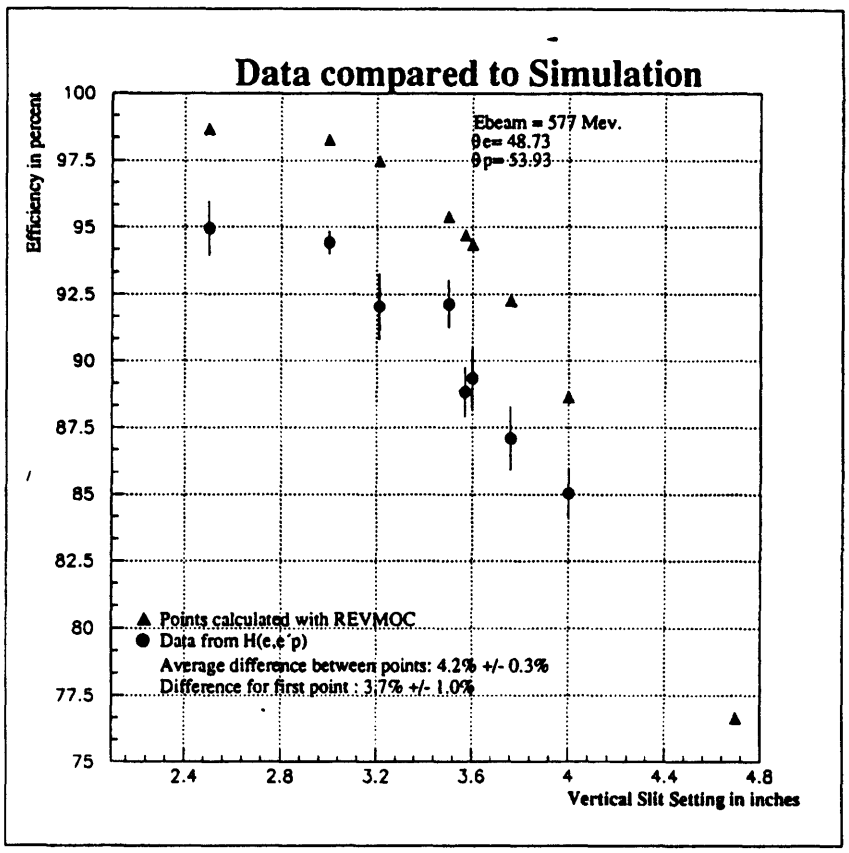

Figure 3-15: The output of REVMOC compared to measured H(e,e′p)efficiency as a function of ELSSY slit setting.

lieved the detection efficiency of the protons should be, considering multiple scattering. We then divided this percentage by the efficiency obtained from the H(e,e'p) to get the OOPS normalization (figure 3.15).

$$N_{\mathrm{OOPS}} = \frac{eff_{\mathrm{REV\,MOC}}}{eff_{1\mathrm{H(e,e'p)}}} = \frac{98.0}{95.0} = 1.03 \tag{3.18}$$

So we multiplied our raw D(e,e'p) cross sections by this number.

Though these H(e,e'p) measurements were performed with OOPS at 54° and 25°, and with beam energies of 570 and 290 MeV respectively, we assumed that this overall OOPS normalization did not change when we moved OOPS to 64.7° and 42.9° for our R_{LT} measurements.

3.2.7 The OOPS 'Good' event

So for each event the OOPS code does the following:

1. it converts the raw delay line TDC values to wire numbers and drift times.
2. it converts the drift times to drift distances, and,
3. after making appropriate corrections, it converts these drift distances to focal plane coordinates $(x_f, y_f, \theta_f, \phi_f)$.

As in ELSSY, events are divided into two classes:

1. 'noise' events where no reaction related particle passed through the wire chambers (HDCs), and
2. 'real' events where a reaction related particle passed through the wire chambers.

Real events are further divided into two classes:

1. 'bad' events that do not have reconstructible trajectories in the wire chambers, and
2. 'good' events with fully reconstructible trajectories in the wire chambers.

Noise events are separated from real events by the method of section 3.2.5. Good events are selected with the following criteria:

1. at least two out of three X planes fire and likewise for the Y planes.
2. OOPS x_f must be within range $\pm$ 4.6cm, a 1% cut on the tails of the distribution.
3. the angle at the target in the bend direction, θ_T, must be within the range $\pm$ 32mr (section 3.4 discusses how we transformed from focal plane coordinates in OOPS and ELSSY to target coordinates), and,
4. the angle at the target in the transverse direction, ϕ_T, must be within the range $\pm$ 18.5mr. Both items 3 and 4 represent 1% cuts on the distribution tails.

3.3 Relative Efficiency of the Focal Planes

Since the focal planes are not uniformly efficient, we measured their relative efficiencies. This non-uniform efficiency possibly came both from geometrical effects reducing the solid angle feeding different focal plane positions, and from differential detector efficiencies.

We determined the relative unnormalized focal plane efficiencies by measuring a smoothly varying cross-section at several overlapping points in the focal plane and deconvoluting the measurements into a relative efficiency and a cross-section. For ELSSY, we measured the C(e,e′) spectrum either on the quasi-elastic peak or in the dip region at several different central momenta. For OOPS we measured the C(e,p) spectrum at the same time as the C(e,e′) spectrum. We used the program RELEFF [46] to deconvolute the focal plane efficiency from the (e,e′) and (e,p) spectrum. RELEFF approximates the cross-section as the sum of polynomials f_n up to order n:

$$\sigma_{ij} = \sum_n a_n f_n(p_{ij}) \tag{3.19}$$

where σ_{ij} is the cross-section and p_{ij} is the momentum of the i^{th} channel for the j^{th} measurement. The polynomials f_n can be either regular polynomials of the form x^n or Legendre

polynomials. We used Legendre polynomials. The coefficients a_n are then varied by minimizing χ^2 where

$$\chi^2 = \sum_{ij} w_{ij} \left(C_{ij} - N_j \sigma_{ij} \epsilon_i\right)^2 \tag{3.20}$$

and C_{ij} is the number of counts, and w_{ij} is the statistical weight in channel i for run j, N_j is the normalization factor for run j and ϵ_i is the relative efficiency of channel i. An iterative procedure is used to determine ϵ_i and the coefficients a_n. The ϵ_i are initialized at unity and χ^2 minimized with respect to $\{a_n\}$:

$$\frac{\partial_{\chi^2}}{\partial a_n} = o, \quad \forall \quad n \ . \tag{3.21}$$

This gives n linear equations which determine $\{a_n\}$:

$$X_n = \sum_m M_{mn} a_m = 0 \ , \tag{3.22}$$

where

$$X_n = \sum_{ij} w_{ij} C_{ij} \epsilon_i N_j f_n \left(p_{ij}\right) \tag{3.23}$$

and

$$M_{mn} = \sum_{ij} w_{ij} \left(\epsilon_i N_j\right)^2 f_m \left(p_{ij}\right) f_n \left(p_{ij}\right) \ . \tag{3.24}$$

The coefficients a_m are found by inverting the matrix M and calculating $M^{-1}X$. With these coefficients new efficiencies are computed:

$$\epsilon_i = \frac{\sum_j C_{ij}}{\sum_j \sum_n N_j a_n f_n \left(p_{ij}\right)} \ . \tag{3.25}$$

Note that this procedure preserves the total number of counts. The ϵ_i so determined are put back into equation 3.22. The procedure is repeated until χ^2 converges; this condition enforces the convergence of ϵ_i and a_n.

The ELSSY focal plane efficiency is shown in figure 3.16. Since the slit settings for ELSSY made for a significantly smaller solid angle than defined by the collimator itself, we

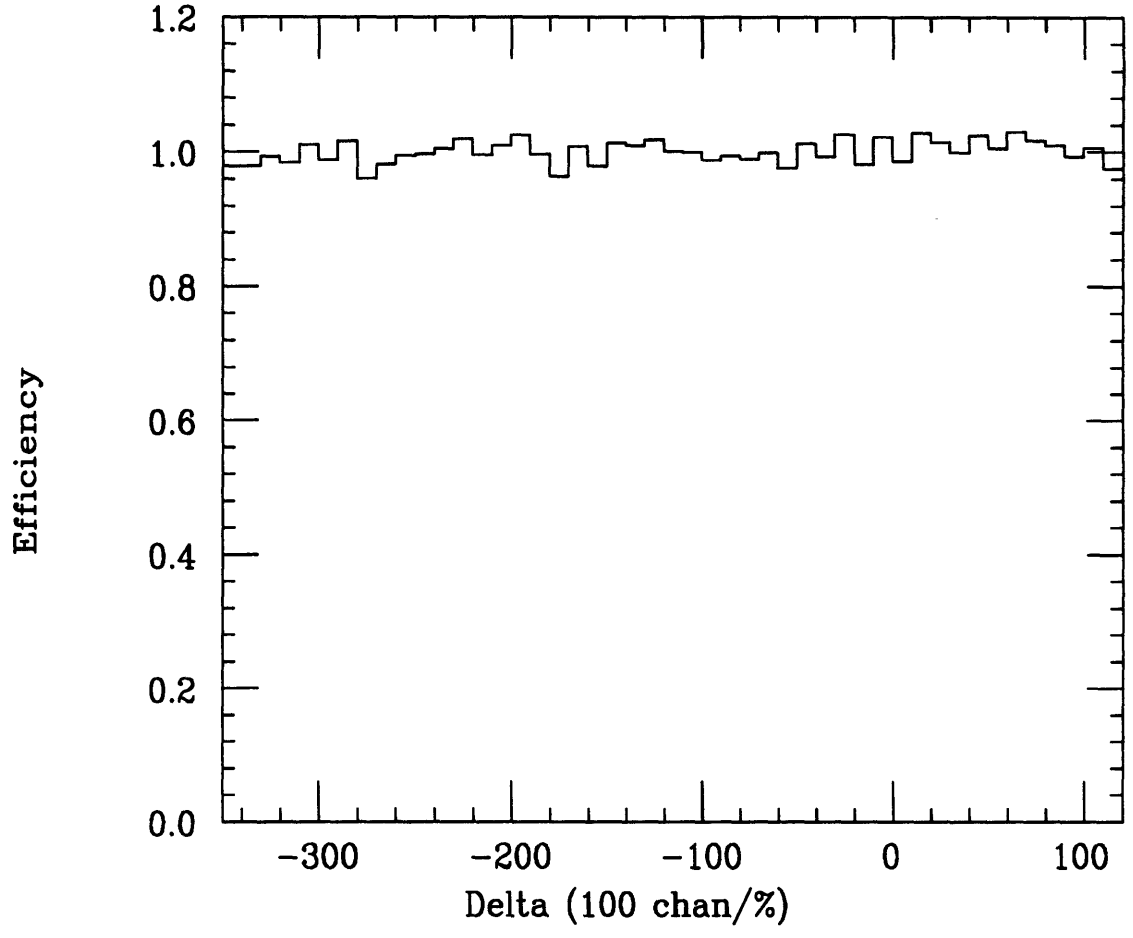

Figure 3-16: Focal plane relative efficiency in the ELSSY momentum where all trajectories reach the scintillators. This spectrum determined by RELEFF.

see that its efficiency profile is essentially flat for a region in delta of about 5%. The steep dropoff thereafter is due to particles completely missing the ELSSY scintillators for certain extreme target angles and momenta (fig. 2.2). As mentioned in section 3.3, we did not use data from this region in our measurement.

The OOPS focal plane efficiency is shown in figure 3.17. Here we see a gradual dropoff which is probably due to geometrical effects. Figure 3.18 shows the measured C(e,p) single-arm cross section in OOPS. Notice that the cross-section measurements are consistent from run to run, indicating that the efficiencies were unfolded correctly.

As a check for OOPS, we compared our results with those of [47]. These authors determined The OOPS focal plane efficiency using a TURTLE simulation [48]. Their result is shown in figure 3.19. Notice that the curves in figures 3.17 and 3.19 have the same shape within statistical error.

3.4 The Focal Plane to Target Transformation

In order to construct the cross section $\frac{d^6\sigma}{d\Omega_e d\Omega_p dE_m d\omega}$, we need the target angles for each event, θ_T (bend) and ϕ_T (transverse), as well as the final proton and electron momenta at the target, given by δ_T. [1] Since we are only able to measure angles and positions at the focal plane, we must find a transformation to go from $(x_f, y_f, \theta_f, \phi_f)$ to $(x_f, y_f, \theta_f, \phi_T)$. In addition, we need to determine $\delta(x_f)$ from the focal plane coordinates.

For both spectrometers, this transformation can be written as to first order as:

$$\begin{pmatrix} X_T \\ \theta_T \\ Y_T \\ \theta_T \end{pmatrix} = \mathbf{M} \begin{pmatrix} X_f \\ \theta_f \\ y_f \\ \theta_f \end{pmatrix} \tag{3.26}$$

[1] Remember, the magnetic fields of the spectrometers do not change the momentum of either the proton or electron between the target and the focal plane, $\delta_T = \delta_f$. The Lorentz force always acts perpendicular to the charged particle's trajectory, doing no work on the particle.

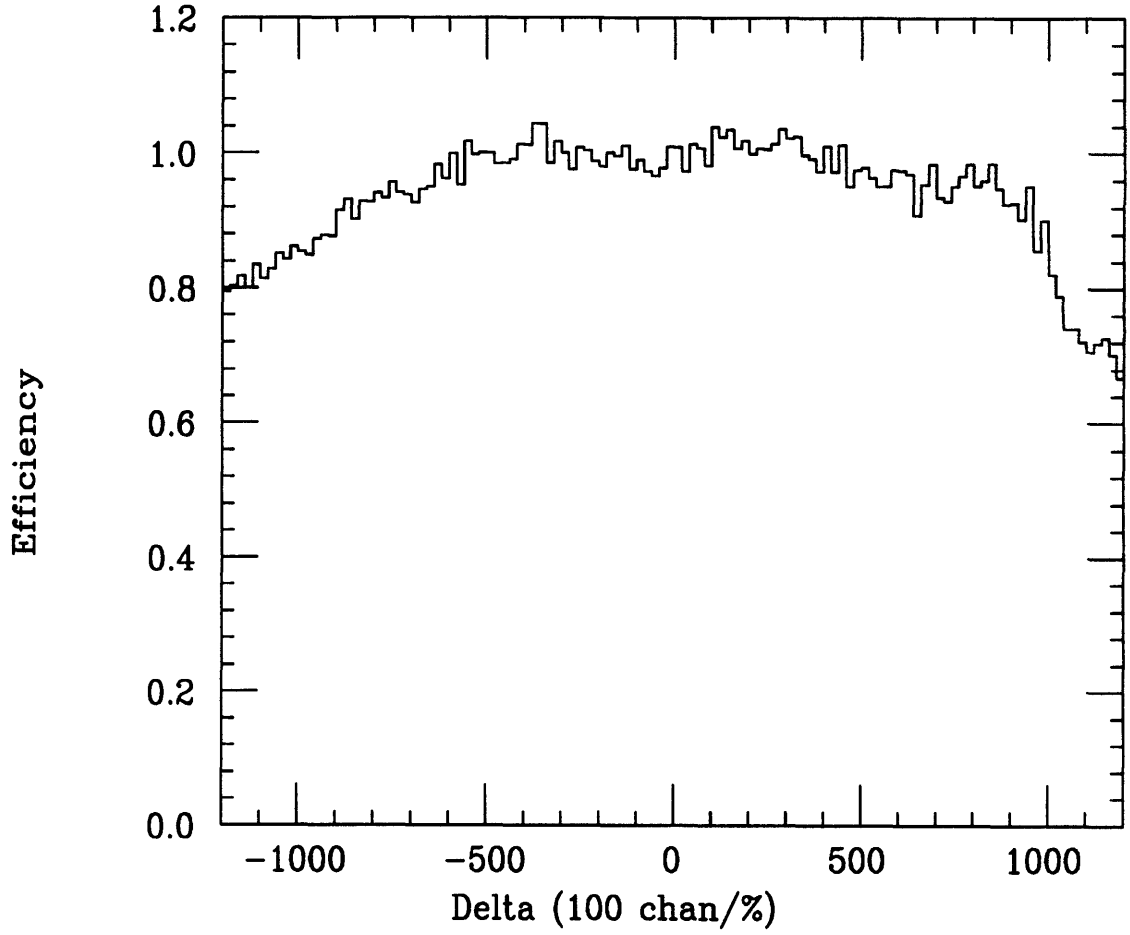

Figure 3-17: Focal plane relative efficiency in OOPS as determined by RELEFF.

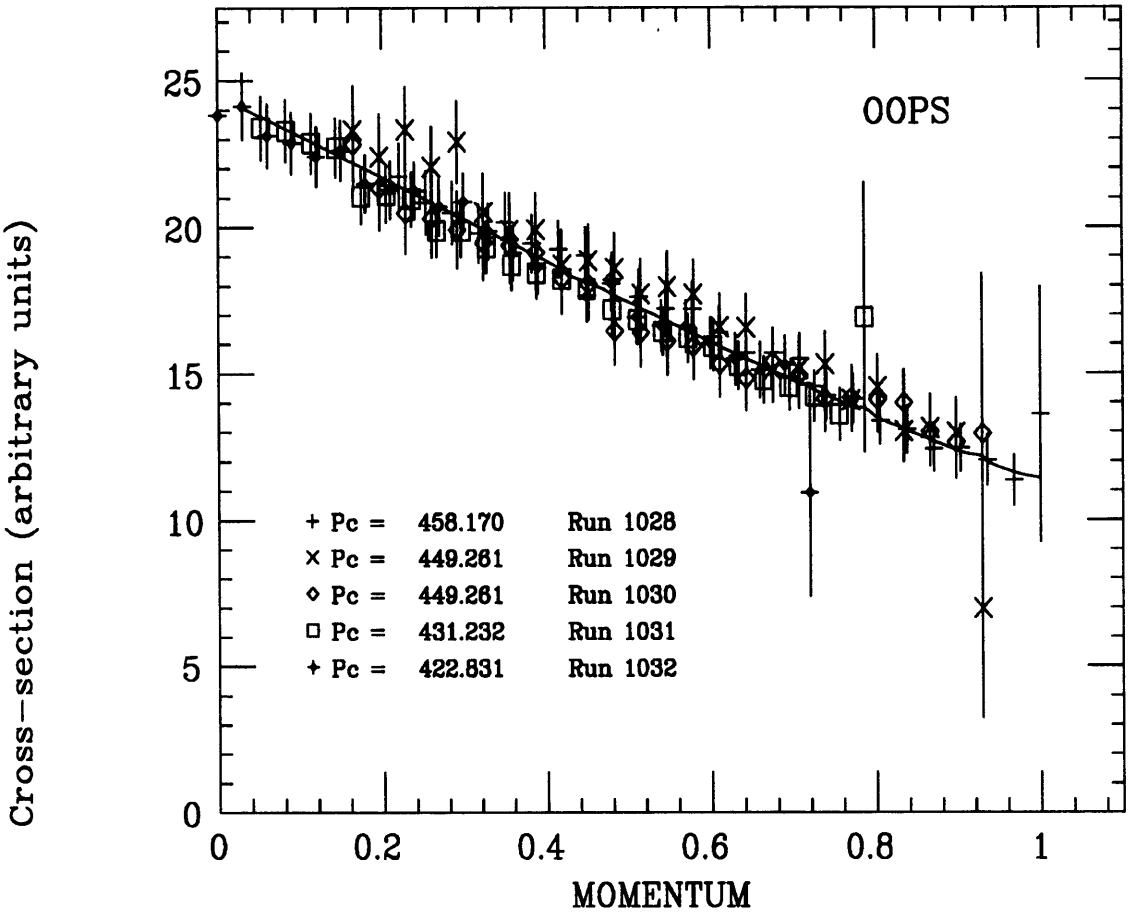

Figure 3-18: The measured C(e,p) cross section in OOPS for runs used in RELEFF.

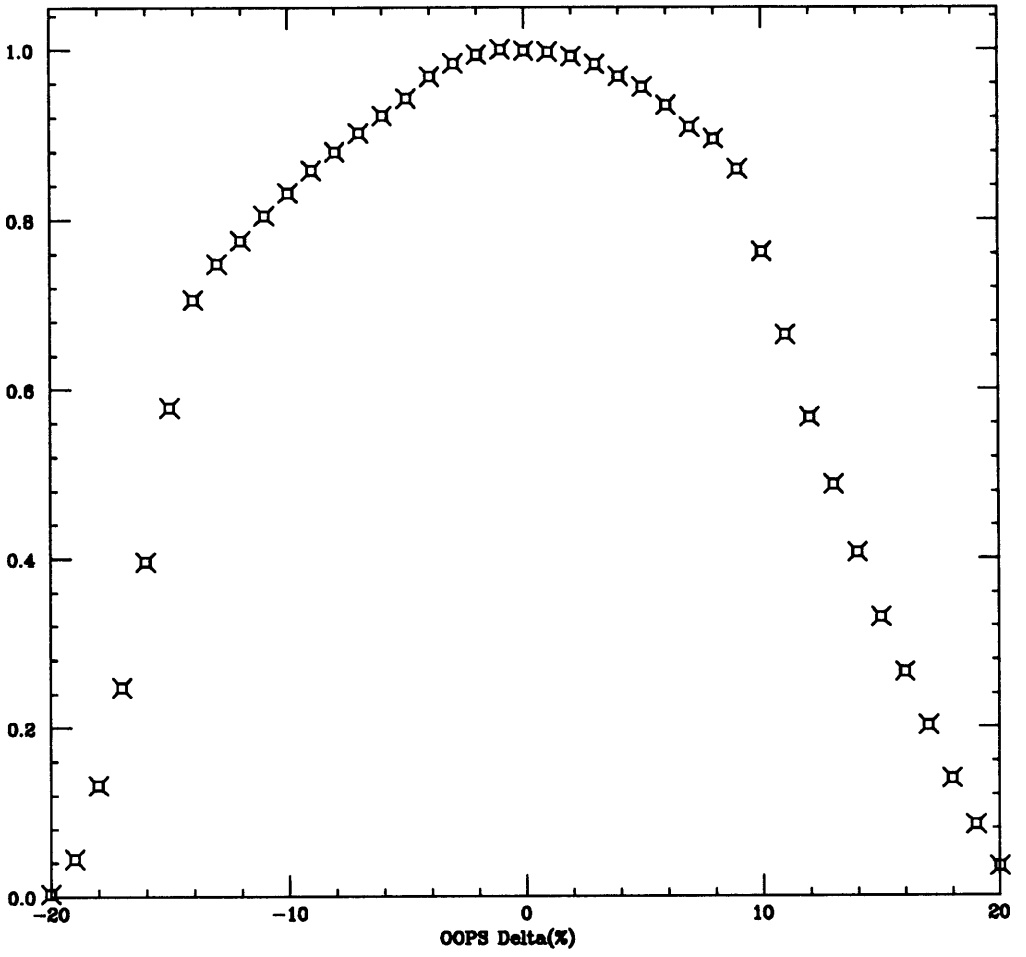

Figure 3-19: The OOPS relative efficiency profile determined by TURTLE.

where 'T' denotes a target vector, 'f' denotes a focal plane vector, and **M** is a the 4x4 transformation matrix.

We then speak of the 'matrix element' M_{11} as $\frac{dx_T}{dx_f}$ etc. The entire set of matrix elements for the spectrometer is referred to as the spectrometer 'optics.' The higher order matrix elements were determined for both spectrometers and were found to be small, though some were included in the focal plane to target transformation in replay.

3.4.1 ELSSY Optics

We measured the ELSSY matrix elements using a sieve slit. This 25 hole sieve slit produced the pattern shown in figure 3.20 at the focal plane. We produced a spectrum like figure 3.20 for a number of discrete states in Carbon, Beryllium, and Oxygen (fig. 3.21). Thus, each set of 'spots' corresponded to a certain x_f. So we knew (θ_T, ϕ_T) for each hole, and we measured (θ_f, x_f, Y_f) for each hole as well. We then fit the data to obtain $\theta_T(x_f, Y_f, \theta_f)$ and $\phi_T(x_f, Y_f, \theta_f)$. [2] This resulted in the matrix elements of table 3.2.

[2] Recall that ELSSY was designed so that ϕ_f would be 0 for all target rays. Thus, the ϕ_f dependence was small and ignored.

Matrix Element	value	uncertainty
$\langle\theta\|\theta\rangle$	-1.022	0.003
$\langle\theta\|x\rangle$	$8.618 \cdot 10^{-1}$	$0.141 \cdot 10^{-1}$
$\langle\theta\|y\rangle$	$-2.484 \cdot 10^{-1}$	$0.182 \cdot 10^{-1}$
$\langle\theta\|y^2\rangle$	$3.882 \cdot 10^{-2}$	$0.475 \cdot 10^{-2}$
$\langle\theta\|x\theta\rangle$	$-1.109 \cdot 10^{-3}$	$0.273 \cdot 10^{-3}$
$\langle\theta\|xy\rangle$	$-1.530 \cdot 10^{-2}$	$0.185 \cdot 10^{-2}$
$\langle\theta\|xy^2\rangle$	$1.394 \cdot 10^{-3}$	$0.491 \cdot 10^{-3}$
$\langle\theta\|\theta^2\rangle$	$2.483 \cdot 10^{-4}$	$0.867 \cdot 10^{-4}$
$\langle\phi\|y\rangle$	1.636	0.020
$\langle\phi\|\theta^2 y\rangle$	$7.397 \cdot 10^{-5}$	$1.329 \cdot 10^{-5}$
$\langle\phi\|x\theta y\rangle$	$-1.781 \cdot 10^{-4}$	$0.428 \cdot 10^{-4}$
$\langle\phi\|\theta y\rangle$	$-5.005 \cdot 10^{-5}$	$48.10 \cdot 10^{-5}$
$\langle\phi\|xy\rangle$	$-9.983 \cdot 10^{-3}$	$1.286 \cdot 10^{-3}$
θ_T offset	5.200	0.190
ϕ_T offset	$4.734 \cdot 10^{-2}$	$6.46 \cdot 10^{-2}$

Table 3.2 The ELSSY Matrix Elements

Additional details of our procedure are well described in [49].

The ELSSY Momentum Calibration

In addition to the matrix elements quoted in the previous section, we also needed to know the ELSSY δ as a function of x_f. We expected a near linear dependence, but we fit to second order to check this.

The procedure was to scan an elastic peak across the focal plane by changing the ELSSY magnetic fields in increments of about 1% (fig. 3.22). Events in the peak then had energy

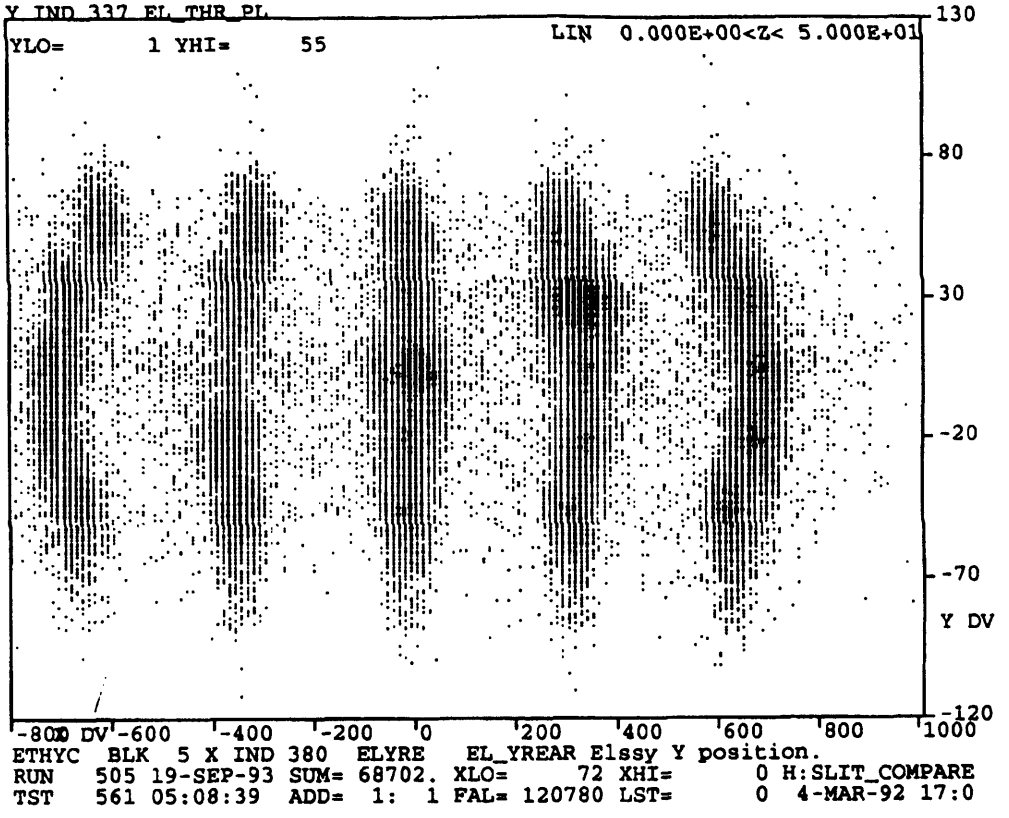

Figure 3-20: θ_f vs. Y_f with sieve slit installed. Using a fitting routine, 25 holes can be resolved.

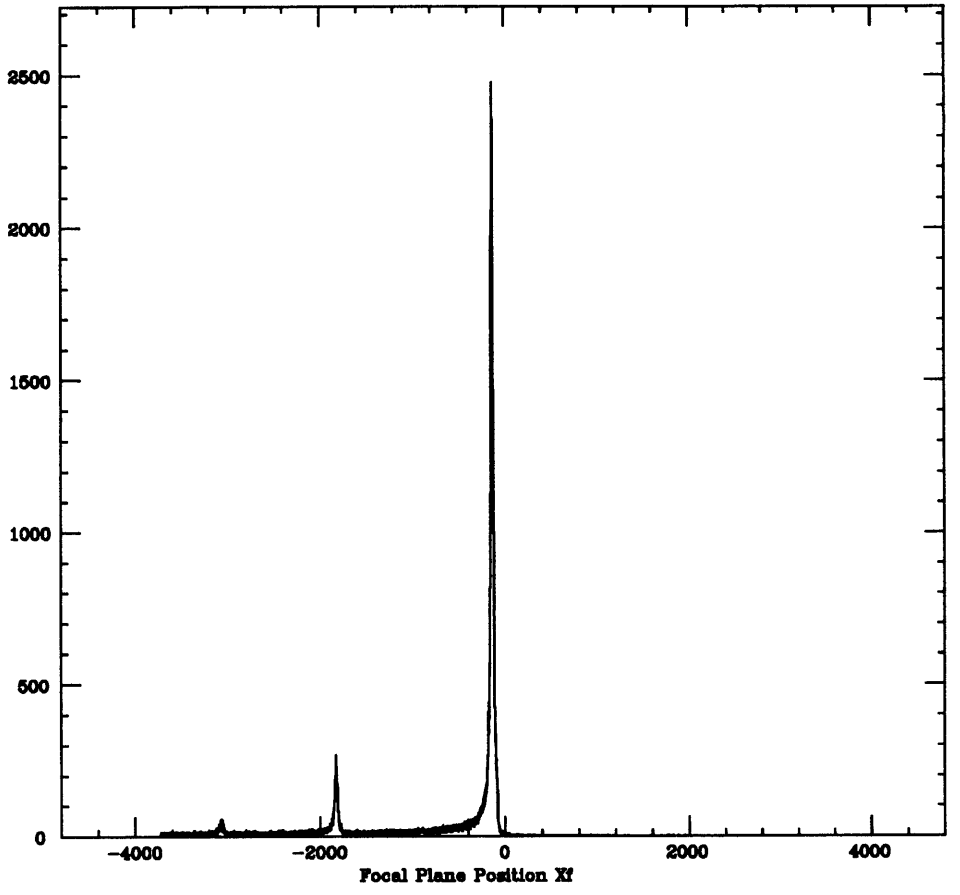

Figure 3-21: The Carbon elastic(highest) and excited states measured in ELSSY for the optics study.

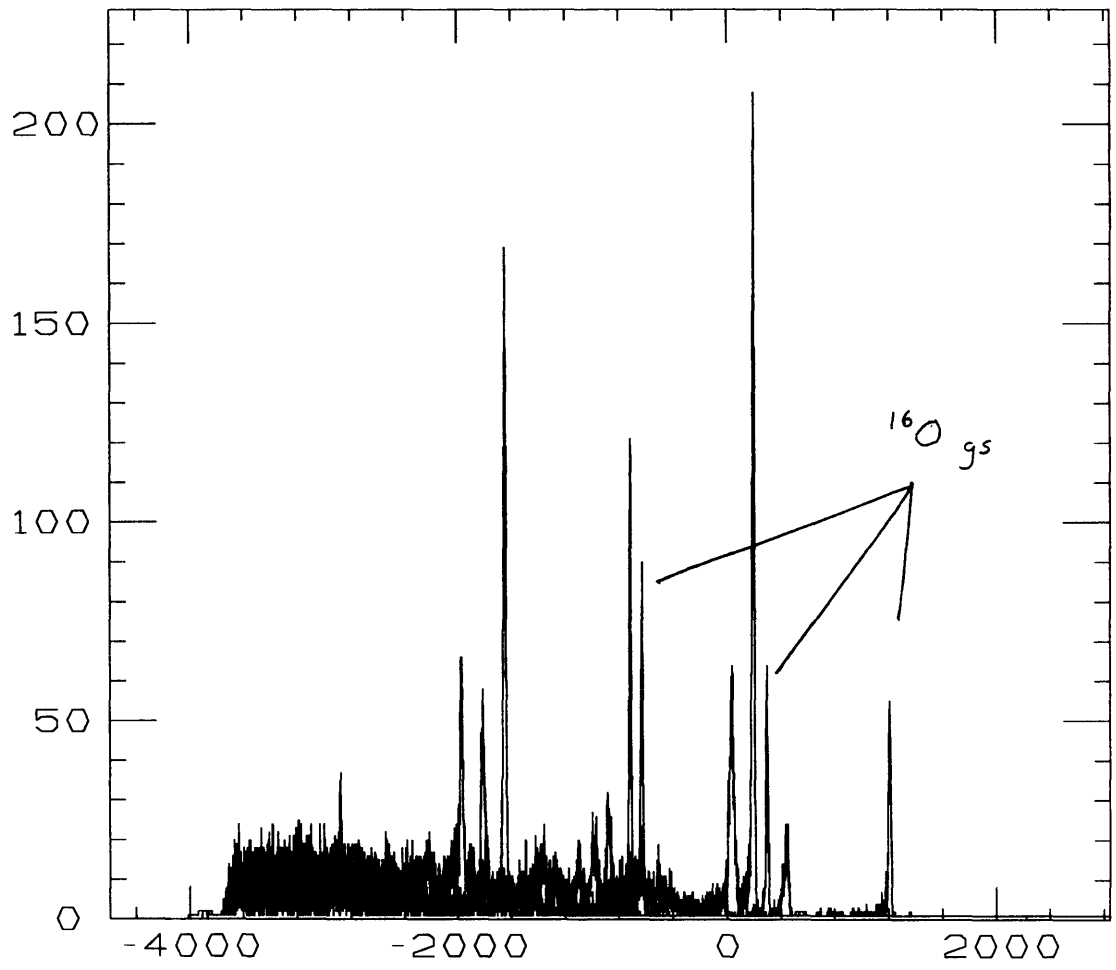

Figure 3-22: An overlay of three BeO spectra offset by 1% changes in the ELSSY magnetic field. We used the Oxygen elastic peak for our calibration.

E_f where

$$E_f = \frac{E_0}{1 + \frac{2E_0}{M_T}\sin^2\left(\frac{\theta_e}{2}\right)} \tag{3.27}$$

and where E_0 is the beam energy determined by the method of section 3.6, θ_e is the scattering angle, and M_T is the mass of the target nucleus (^{16}O for our case). Of course, the scattering angle θ_e is the sum of the angle where ELSSY sits and ϕ_T, the deviation from the spectrometer central angle.

We then kinematically corrected the peaks. ELSSY has a finite acceptance in the scattering angle θ_e. Thus, events have a range in final energy due to this angular range. We eliminated this 'kinematic broadening' by using our ϕ_T reconstruction. Thus we had

$$E_{f_{kin}} = \frac{E_0}{1 + \frac{2E_0}{M_T}\sin^2\left(\frac{\theta_e - \phi_T}{2}\right)} \tag{3.28}$$

These 'kinematically corrected' peaks were narrower than the original ones, broadened only by the ϕ_T resolution, and thus made for better position determination.

Next we fit the narrowed peaks using ALLFIT to find their positions in x_f. Then we found the value of δ for each peak

$$\begin{aligned} \delta_i &= \frac{E_f}{E_{ci}} - 1 \\ E_{ci} &= \alpha_{\mathrm{ELSSY}} B_i \end{aligned} \tag{3.29}$$

where E_{ci} is the central momentum setting for peak i, B_i is the magnet setting for run i, and α_{ELSSY} is the ELSSY magnet constant.

The result is a mapping of δ to x_f (figure 3.23) which we used to fit for our function of interest $\delta(x_f)$. The two additional ELSSY matrix elements we found from this procedure are listed in table 3.3. Notice that the second order term is very small, the dependence being mostly linear.

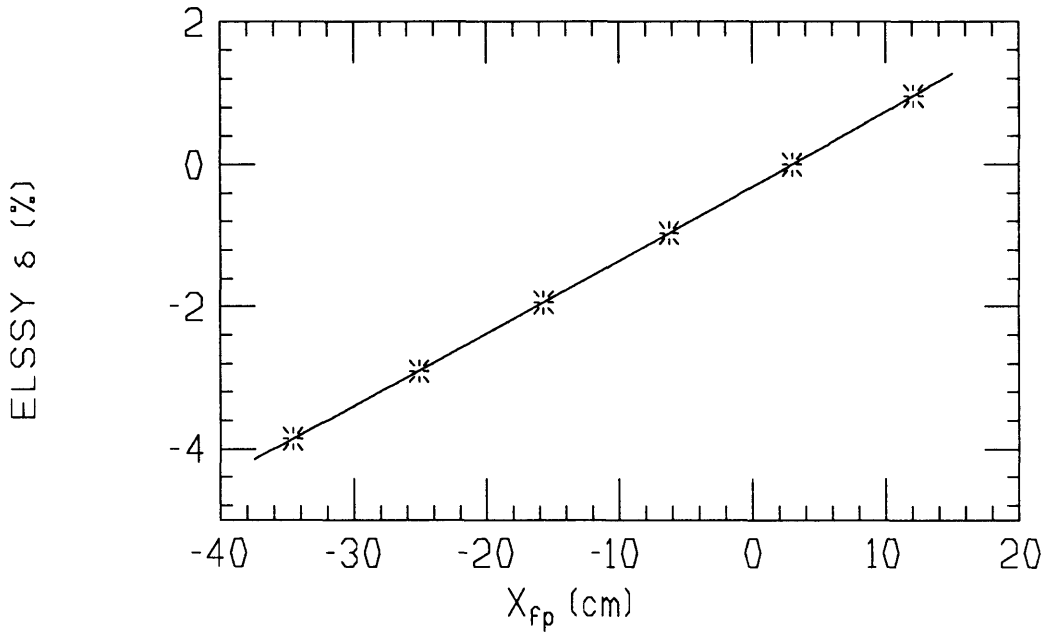

Figure 3-23: Our fit of $\delta(x_f)$.

Matrix Element	value
$\langle\delta\|x\rangle$	0.105
$\langle\delta\|x^2\rangle$	$7 \cdot 10^{-5}$
δ offset	0.40

Table 3.3 The ELSSY Momentum Matrix Elements

3.4.2 OOPS Optics

The OOPS matrix elements were found using essentially the same techniques as described in the previous section for ELSSY, and are listed in table 3.4. For more details on the measurement of the OOPS matrix elements, and for a listing of the design matrix elements for OOPS, see [50].

Matrix Element	value (error in last digit)
$\langle\delta\|x\rangle$	4.65
$\langle\delta\|x\theta\rangle$	$2.17 \cdot 10^{-2}$
$\langle\delta\|x\theta^2\rangle$	$8.2 \cdot 10^{-5}$
$\langle\delta\|\theta\rangle$	$4.9 \cdot 10^{-3}$
$\langle\delta\|\theta y^2\rangle$	$-5.4 \cdot 10^{-5}$
$\langle\delta\|y^2\rangle$	$2.1 \cdot 10^{-3}$
δ offset	0.18
$\langle\theta\|\theta\rangle$	$-2.907 \cdot 10^{-1}$
$\langle\theta\|x\rangle$	-4.05
$\langle\theta\|x\theta\rangle$	$-3 \cdot 10^{-2}$
$\langle\phi\|y\rangle$	1.096
$\langle\phi\|\phi\rangle$	0

Table 3.4 The OOPS Matrix Elements

3.5 Target Thickness Normalization

As mentioned at the beginning of chapter 2, our target for the R_{LT} measurement was a solid CD_2 spinner of nominal thickness 77.5 mg/cm^2. We found it necessary to monitor the target thickness throughout the experiment by measuring the $D(e,e')$ cross section in ELSSY intermittently. We were uncertain of our target thickness from run to run for the following reasons:

1. From data taken for the R_L-R_T separation on Deuterium, which used a different CD_2 spinner, we found that the beam produced enough heat to cause a certain amount of evaporation of deuterium from the target (fig. 3.24). Thus, we suspected this might be the case for our target.

2. The R_L-R_T separation data also revealed that the CD_2 contained a certain percentage of Hydrogen. We weren't able to check how much Hydrogen was in our target but the R_L-R_T spinner was about 2.5% CH_2.

3. There was the possibility of some systematic error (value unknown) in the measurement of the CD_2 target thickness at Bates. This measurement gave us the value of 77.5 mg/cm^2.

We fit the Deuteron elastic peak (fig. 3.25) with ALLFIT and used this information, along with the ELSSY normalization and efficiency method (section 3.1.6), to obtain $D(e,e')$ cross sections. We then compared these with parameterized deuterium elastic cross sections measured at Saclay [51] (fig. 3.26) and 'normalized' our spinner thickness to the [51] data, for each run, accordingly.

us an average CD_2 thickness of about 70 mg/cm^2 for our data runs. Thus, our measured target thickness averaged about 90% of our nominal target thickness.

3.6 Beam Energy Calibration

The Bates switchyard magnets determined our Beam energy to be nominally 580 MeV. The Beck formula of [40] gave 570 MeV for the beam. In order to obtain a more precise number for E_0, we implemented a method of finding the focal plane calibration in ELSSY that minimized our systematic error. We then used the standard technique of differential recoil to determine the beam energy. We used ELSSY for this since it is the highest resolution electron spectrometer at Bates.

3.6.1 Focal Plane Calibration

First we parameterize the x_f dependence of the focal plane as

$$E(X_f) = E(0) + AX_f + \frac{B}{2}X_f^2 + \frac{C}{3}X_f^3 + \ldots \tag{3.30}$$

We then differentiate, obtaining

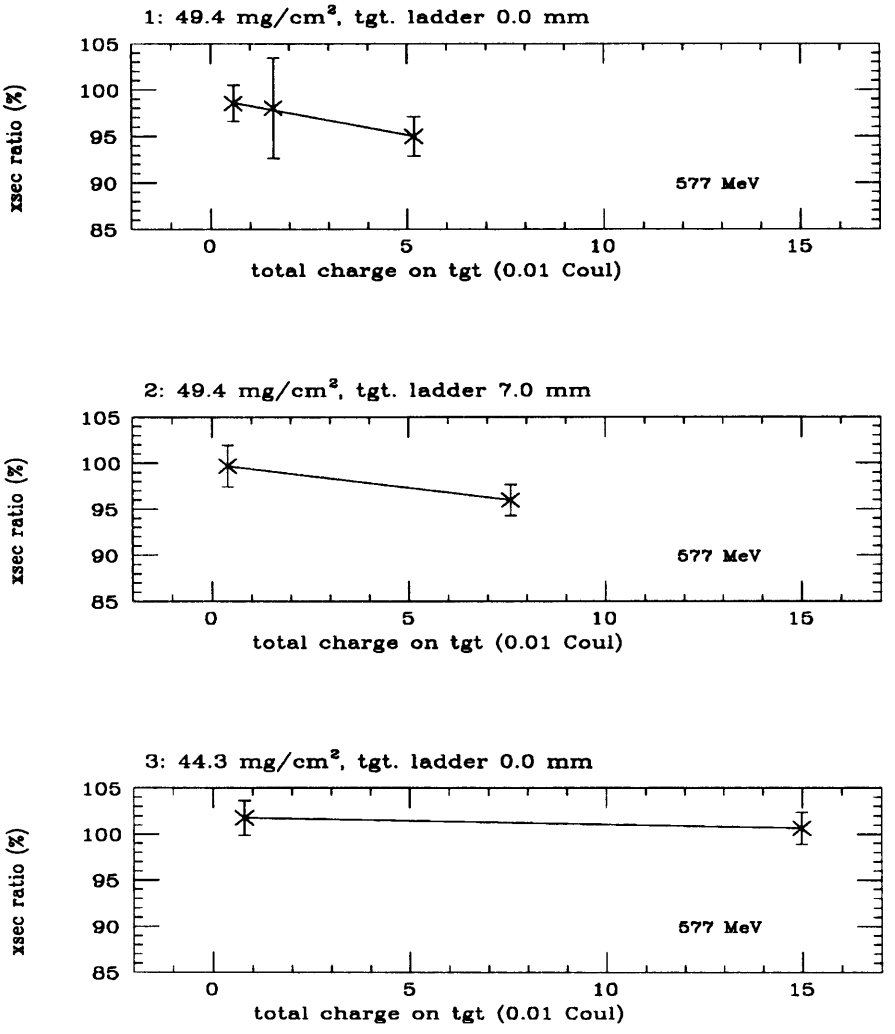

Figure 3-24: Deuterium evaporation in the R_L-R_T runs.

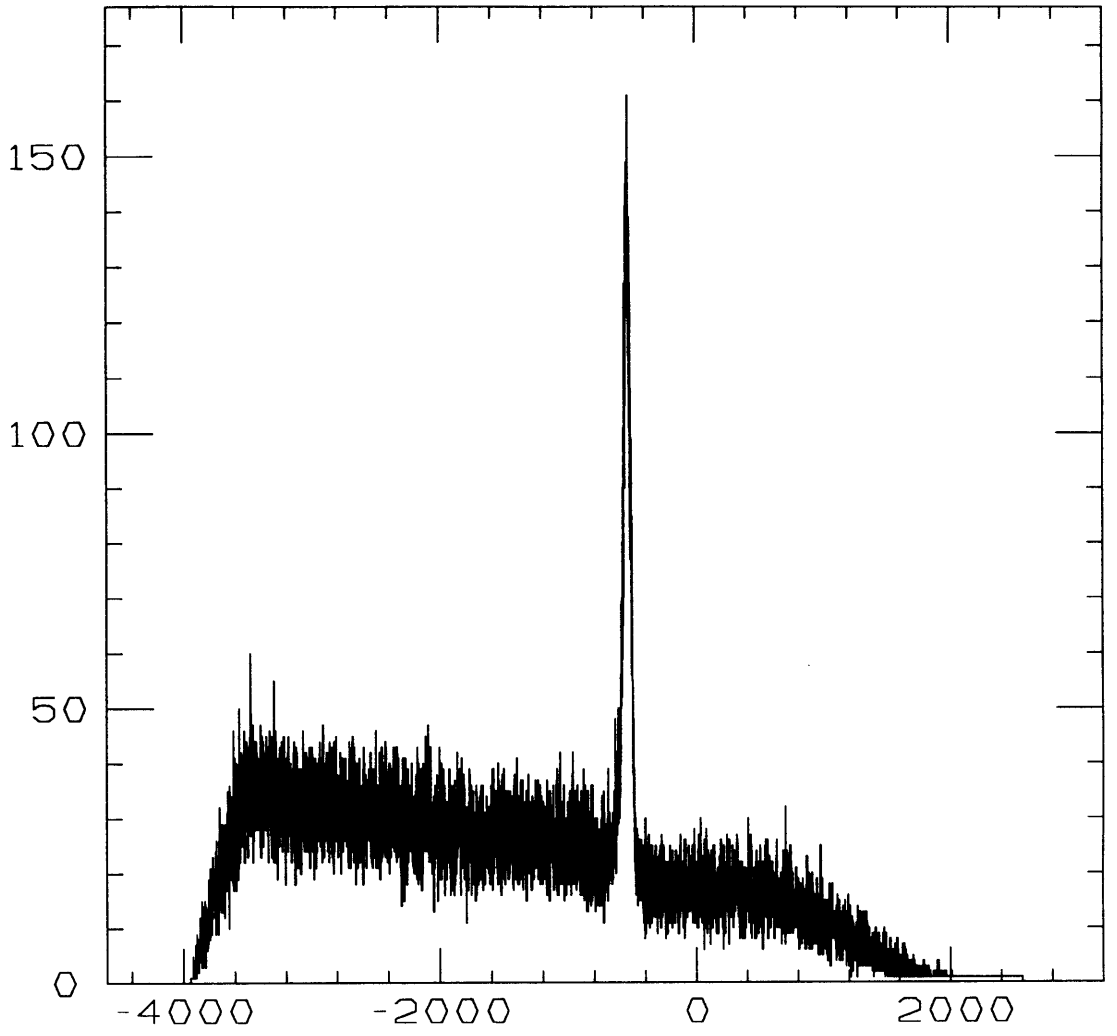

Figure 3-25: The Deuteron elastic peak. The background is from the Carbon in the target and the peak is kinematically corrected to narrow it for better position determination.

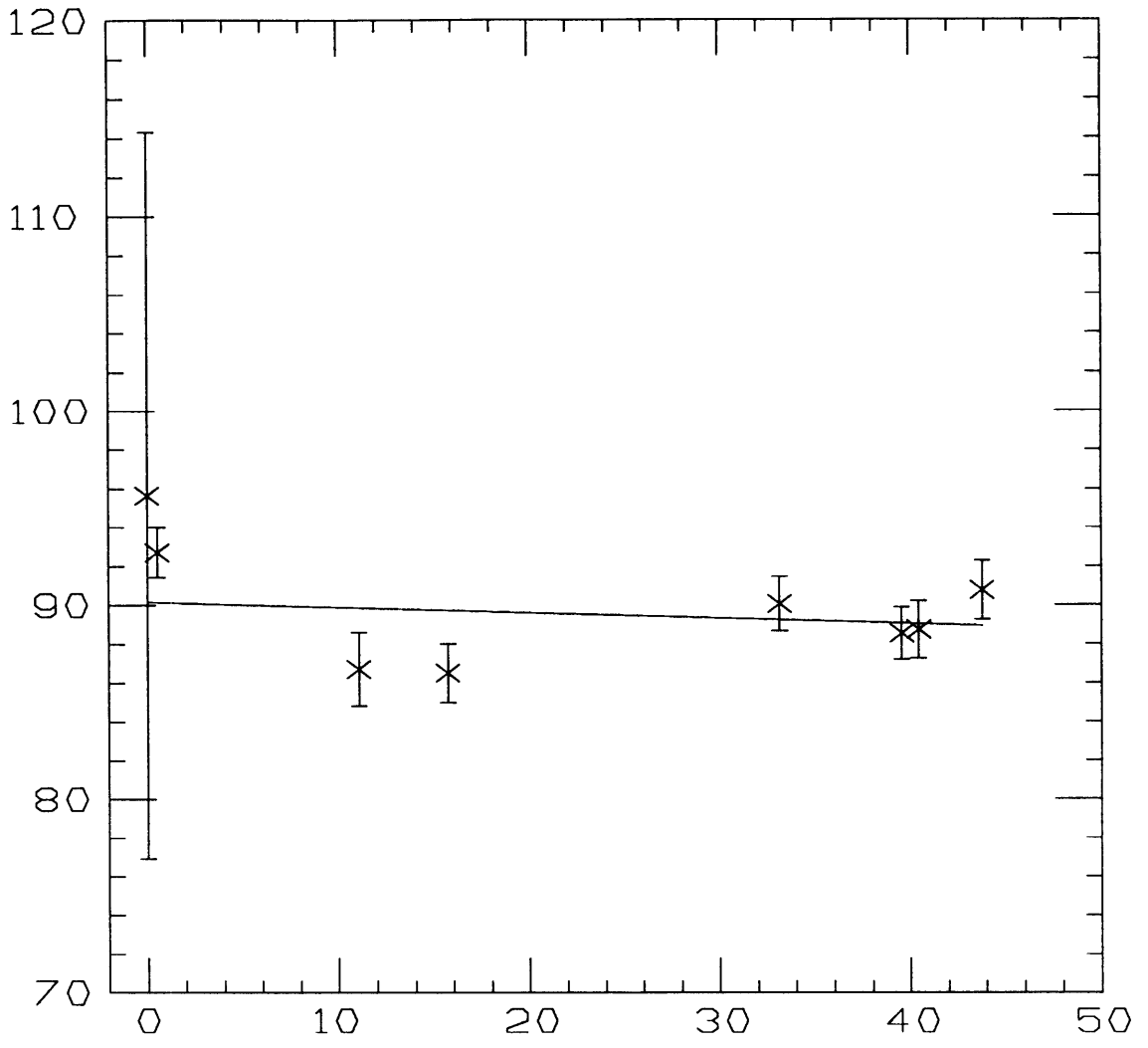

Figure 3-26: The ratio $\frac{D(e,e')_{\text{ELSSY}}}{D(e,e')_{\text{Saclay}}}$ in % and as a function of total charge on target (i.e. time). Also shown is a linear fit to the points.

$$\frac{dE}{d_{X_f}} = A + BX_f + CX_f^2 + \ldots \tag{3.31}$$

Expecting a dependence only up to second order, we cut off the expansion appropriately to give

$$\frac{dE}{d_{X_f}} = A + BX_f \tag{3.32}$$

Now we need to determine the parameters A and B. To do this, we scattered electrons off a Carbon target and off a BeO target and set ELSSY to look at the elastic and other discrete states of these nuclei (figures 3.27-3.28). We then assigned an energy to each peak. For a pair of peaks we can write

$$\frac{E(X_{f2}) - E_1(X_{f1})}{X_{f2} - X_{f1}} = A + B\left(\frac{X_{f1} + X_{f2}}{2}\right) \tag{3.33}$$

If we now define $\left(\frac{X_{f1}+X_{f2}}{2}\right)$ to be X_f we then can rewrite equation 3.33 as

$$\frac{\Delta E}{\Delta X_f} = A + BX_f \tag{3.34}$$

From kinematics we have the energy $E(X_f)$ corresponding to a peak of excitation energy E_x in a nucleus of mass M is:

$$E(X_f) = \frac{1}{\eta}(\bar{E}_0 - \zeta) \tag{3.35}$$

where

$$\begin{aligned} \eta &\equiv 1 + \frac{2\bar{E}_0}{M}\sin^2\left(\frac{\theta e}{2}\right) \\ \zeta &\equiv E_x + \frac{Ex^2}{2m} \\ \bar{E}_0 &\equiv 2E_0 - E_{\text{loss}} \end{aligned} \tag{3.36}$$

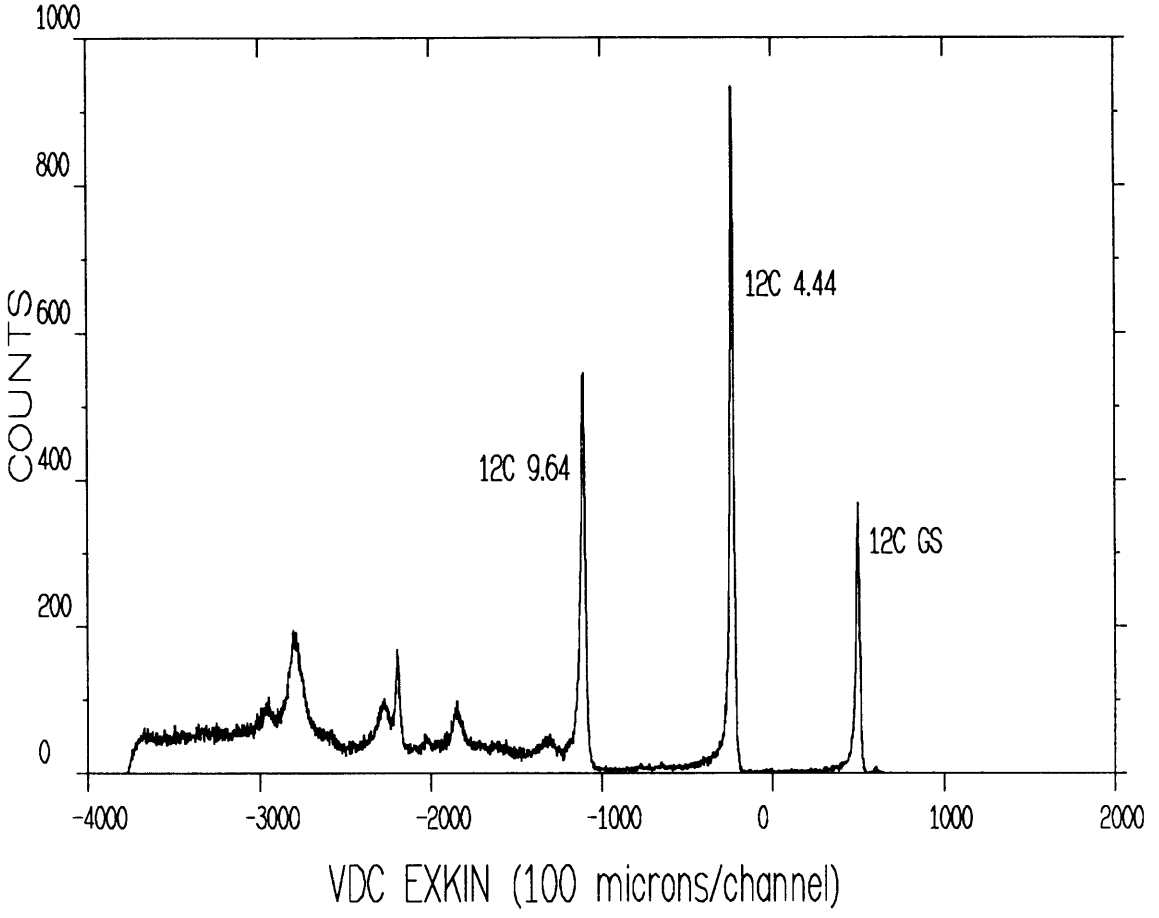

Figure 3-27: Carbon spectrum used for focal plane calibration in the beam energy determination.

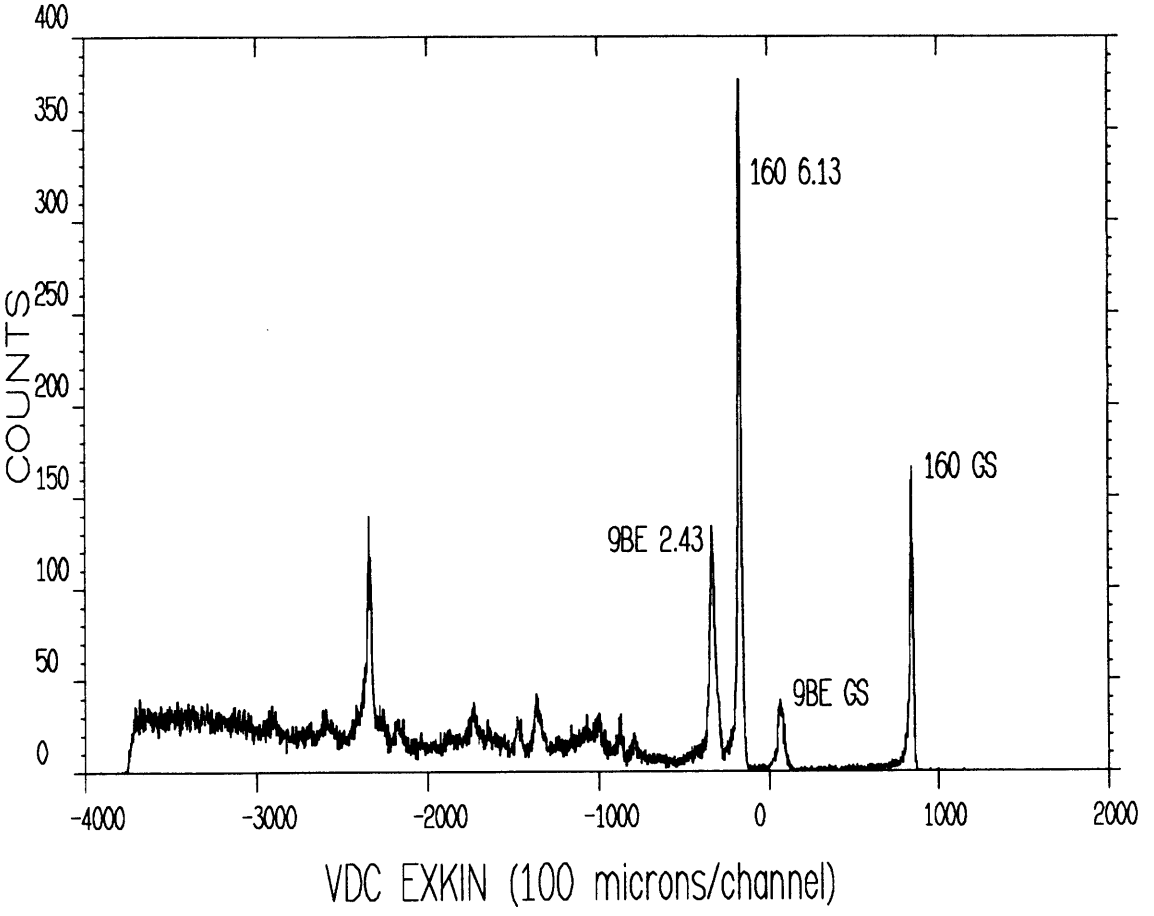

Figure 3-28: BeO spectrum used for focal plane calibration and beam energy determination.

E_{loss} = most probable value of energy lost in target

If we now get ΔE for peaks of the same target and of the same nucleus, we notice that two of the possible four terms yielded by equation 3.35 cancel giving

$$\Delta E = \frac{1}{\eta}\left(Ex + \frac{Ex^2}{2m}\right) \tag{3.37}$$

and so our expression for ΔE has only a weak dependence on E_{loss}. This is where we gain in systematic error over the corresponding expression if we take ΔE for peaks in different nuclei and/or targets. In general, all four terms appear

Figures 3.27 and 3.28 show the peaks we used for the calibration. We used the ^{12}C gs, 4.4, and 9.6 MeV states, and the ^{16}O gs and 6.1 MeV state. The other candidates were unsuitable due to overlap with a neighboring state from another nucleus. This overlap made our determination of the peak position with ALLFIT unreliable to the required accuracy.

3.6.2 Results

Once we have the focal plane calibration, we can use the Beryllium and Oxygen ground states to get the beam energy

$$\frac{\Delta E}{\Delta X_f} = \left(\frac{1}{\eta_O} - \frac{1}{\eta_{B_e}}\right) E_0 = A + BX_f \tag{3.38}$$

The results are shown in table 3.5. All energies are in MeV.

We attempted to check the beam energy by also getting E_0 using the Beryllium and Carbon ground states and the Oxygen and Carbon ground states. These pairs gave slightly different results for E_0 and we concluded that, due to a shift in x_T from run to run (a shift that caused x_T to shift), we could not rely on a measure of E_0 by a pair consisting of states from different runs. Of course, it can be seen from equation 3.38 that once we obtain the focal plane calibration, we cannot get E_0 from two states of the same nucleus. Thus, we're left with the Be and O ground states as our differential recoil pair to determine E_0.

Experiment	Date	Nominal Energy	Beck Energy	Measurement Method	Energy
R_L/R_T	2/27	581.7	570.6	Differential Recoil	577.0 ± 0.3
R_L/R_T	3/01	581.7	570.6	Differential Recoil	577.0 ± 0.3
R_L/R_T	3/05	581.7	570.6	Differential Recoil	577.6 ± 0.3
R_L/R_T	3/05	291.1	290.1	Differential Recoil	292.6 ± 0.2
R_L/R_T	3/13	291.1	290.1	Differential Recoil	292.9 ± 0.3
R_{LT}	3/14	581.3	570.2	Differential Recoil	576.0 ± 0.3
R_L/R_T	3/01	581.7	570.6	Opening Angle	578.9 ± 1.6

Table 3.5 Results of the Beam Energy Calibration

3.6.3 The Opening Angle method

Another less precise way of getting E_0 and thus verifying the above method's results is by recognizing that the beam energy can be measured with the spectrometers and the reaction ^{1}H(e,e'p). If we define

$$\gamma_{E_0} \equiv \frac{E_0}{m_p} \tag{3.39}$$

Then we have from the kinematics

$$\gamma_{E_0} = \frac{\sin\theta_e \cos\theta_p}{1 - \cos\theta_e} - 1 \tag{3.40}$$

Where θ_e is the electron scattering angle. θ_p is the proton scattering angle, and both angles are measured with respect to the beam.

So we determine E_0 from our measurement of the spectrometer positions and of the particle angles with respect to these spectrometers. Results are shown in table 3.5 and we see that there is agreement between the opening angle and the differential method. Conversely, the Beck result is rules out. Figure 3.29 shows a histogram of E_0 determined this way event by event. The centroid of the distribution is our E_0 value determined via

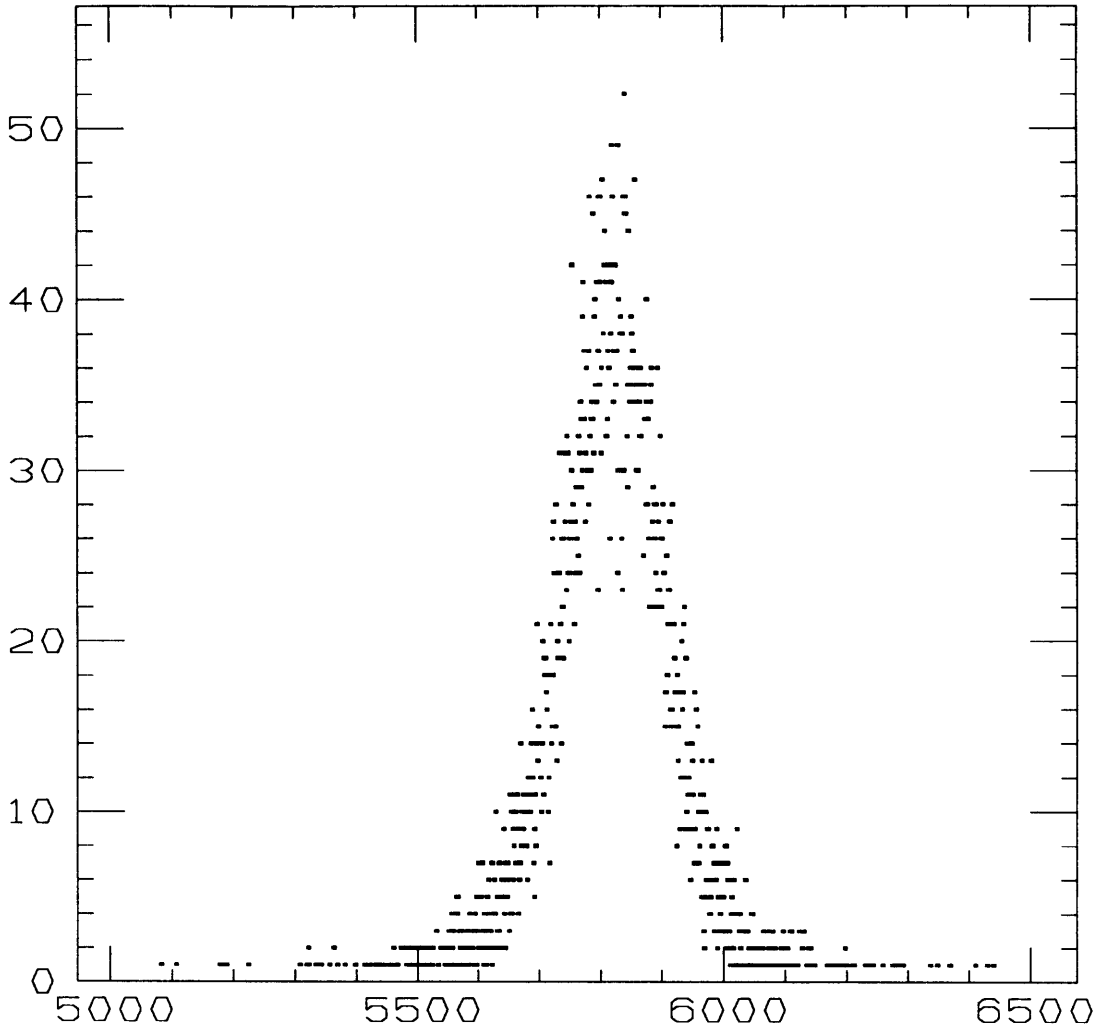

Figure 3-29: Beam energy determined by the scattering angles of proton and electron in H(e,e'p). The fitted centroid of the peak is our beam energy.

opening angle. The width of the distribution is determined by the angular resolution of both OOPS and ELSSY.

3.7 The Coincidence Measurement

Now we are ready to consider the details of the D(e,e'p) measurement. In this section I will first briefly outline our procedure for measuring a coincidence cross section. Included here will be a short discussion about the time-of-flight spectrum, missing energy spectrum, and how to use these to extract the number of coincidence events. A reader needing more detail here should consult [52]. The remaining subsections will detail how we applied these methods to D(e,e'p), how we computed the detection volume $d\Omega_e d\Omega_p d\omega$ as a function of missing momentum, and how we computed our coincidence efficiencies and deadtimes.

3.7.1 The Coincidence Livetime

The coincidence livetime is similar to the single-arm livetimes. It also consists of two terms:

1. the data aquisition livetime,

2. the pileup correction.

The coincidence data aquisition livetime is the number of readable coincidence events on tape divided by the total number of coincidence triggers. The pileup correction is the number of coincidence events on tape with good software triggers (i.e., neither arm has pileup) divided by the same with or without pileup.

$$c\_lt\,(c\_lt_{\rm DAQ})\,(c\_lt_{\rm no\,pileup}) \tag{3.41}$$

3.7.2 Time of Flight Spectra

The relative time-of-flight spectrum (TOF) is the raw time difference between the ELSSY single-arm trigger and the OOPS single-arm trigger. The 'physics', i.e., the event we're

trying to observe, occurs in the peak of figure 3.30. This peak sits on top of a flat background of random coincidences.

The corrected time-of-flight spectrum (TOFC, shown in figure 3.31) has corrections for path length and velocity variation in OOPS. In ELSSY, the velocity variation is negligible, and so its θ_T dependent path length correction is all that's included. By measuring the proton's momentum we can determine its velocity and by measuring its focal plane coordinates we can trace its path back through the spectrometer and determine its flight path length. By correcting the time-of-flight spectrum for the dispersion in flight times, we narrow it and thus reduce the number of accidentals under the timing peak. This increases the signal to noise ratio and decreases the statistical error of the data.

3.7.3 The Missing Energy Spectrum

Once we have the narrower TOFC, we can form the missing energy spectrum. We do this by first forming a 'reals' spectrum (fig. 3.32) by cutting on the TOFC peak (gate 1 in figure 3.31). We also form an 'accidentals' spectrum by cutting on the accidentals region (gate 2 in fig. 3.31). We then form the 'trues' spectrum by subtracting the accidentals from the reals while correcting for the real to accidental gate ration r/a

$$\text{trues} \;=\; \text{reals} \;-\; \frac{r}{a} \cdot \text{accidentals}$$

We then end up with a spectrum such as in figure 3.33 for our CD_2 target. The first peak is the single Deuteron missing energy state while the second peak is the Carbon p-shell. Notice that since we're only interested in the Deuteron peak for this experiment, we replayed the data assuming Deuteron kinematics. This resulted in a broadened and displaced p-shell peak. All that's important here is to be able to separate the two peaks to obtain a D(e,e'p) cross section. More details of how we use the missing energy spectrum will be given in sections 3.7.4-3.7.5.

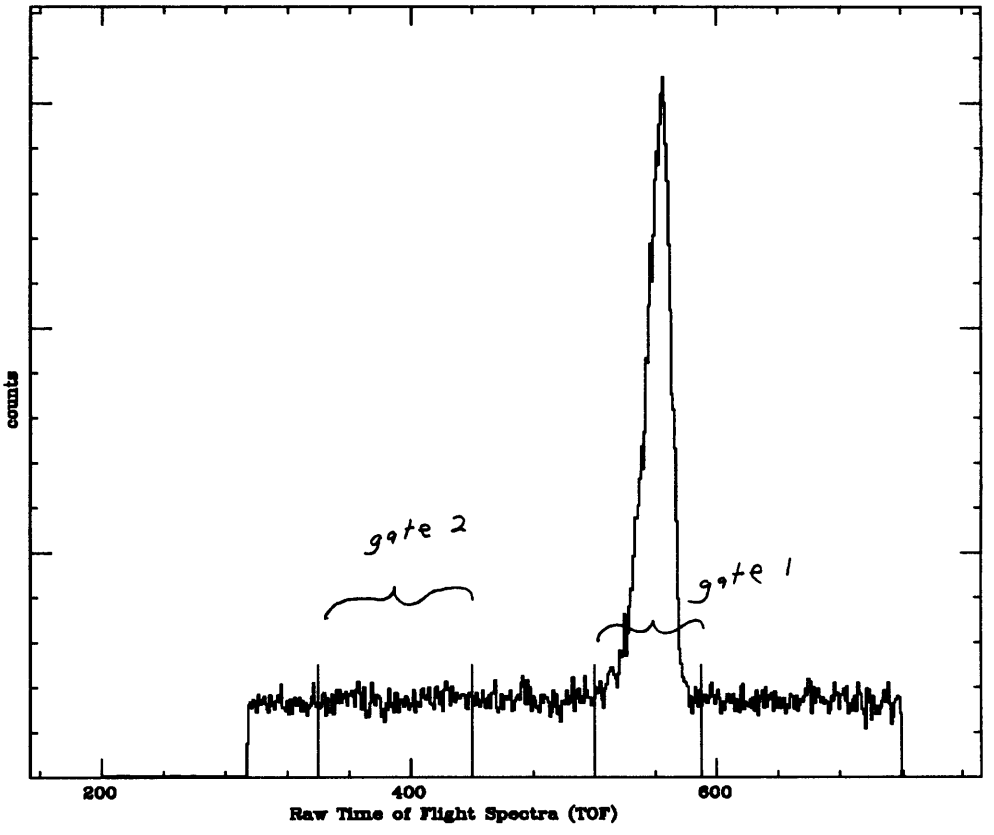
counts
gate 2
gate 1
200
400
600
Raw Time of Flight Spectra (TOF)

Figure 3-30:

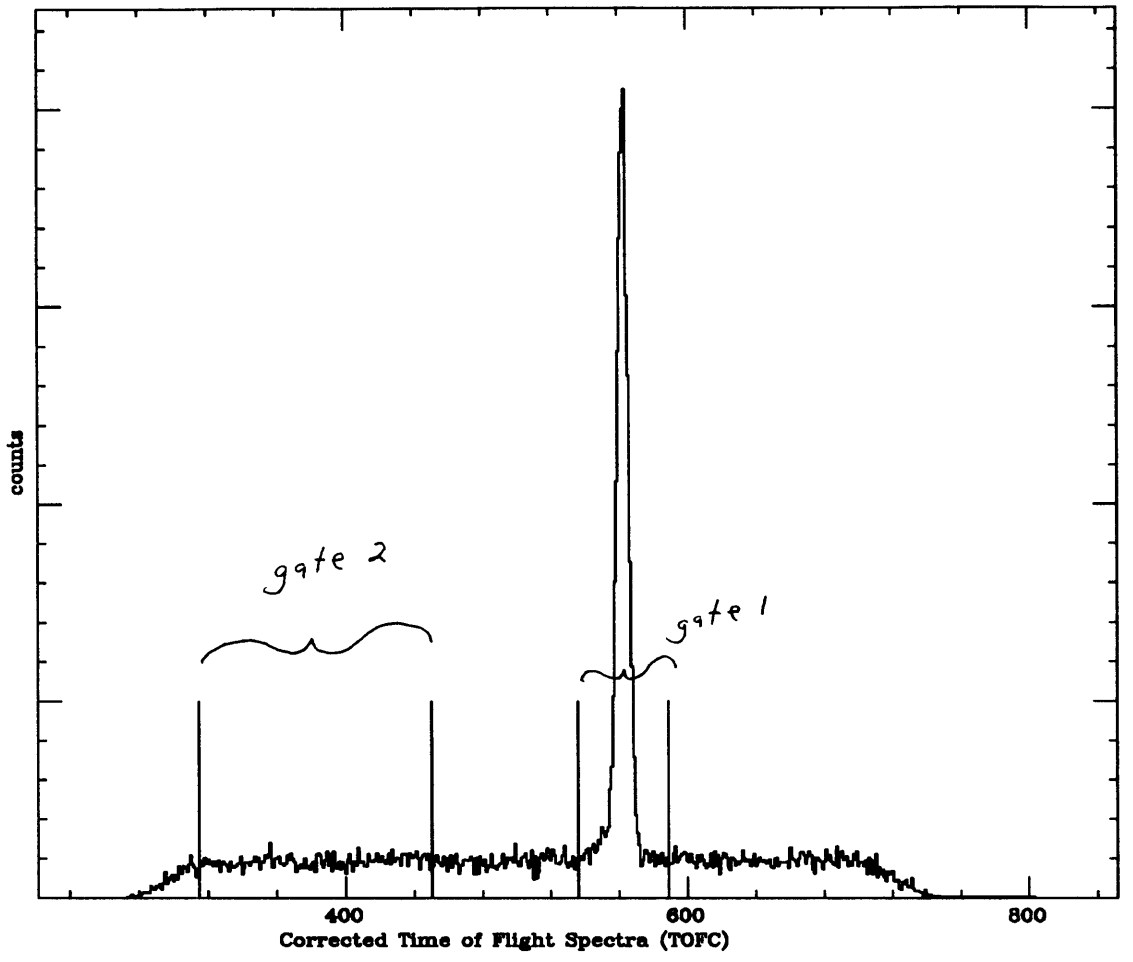
counts
gate 2
gate 1
400
600
800
Corrected Time of Flight Spectra (TOFC)

Figure 3-31:

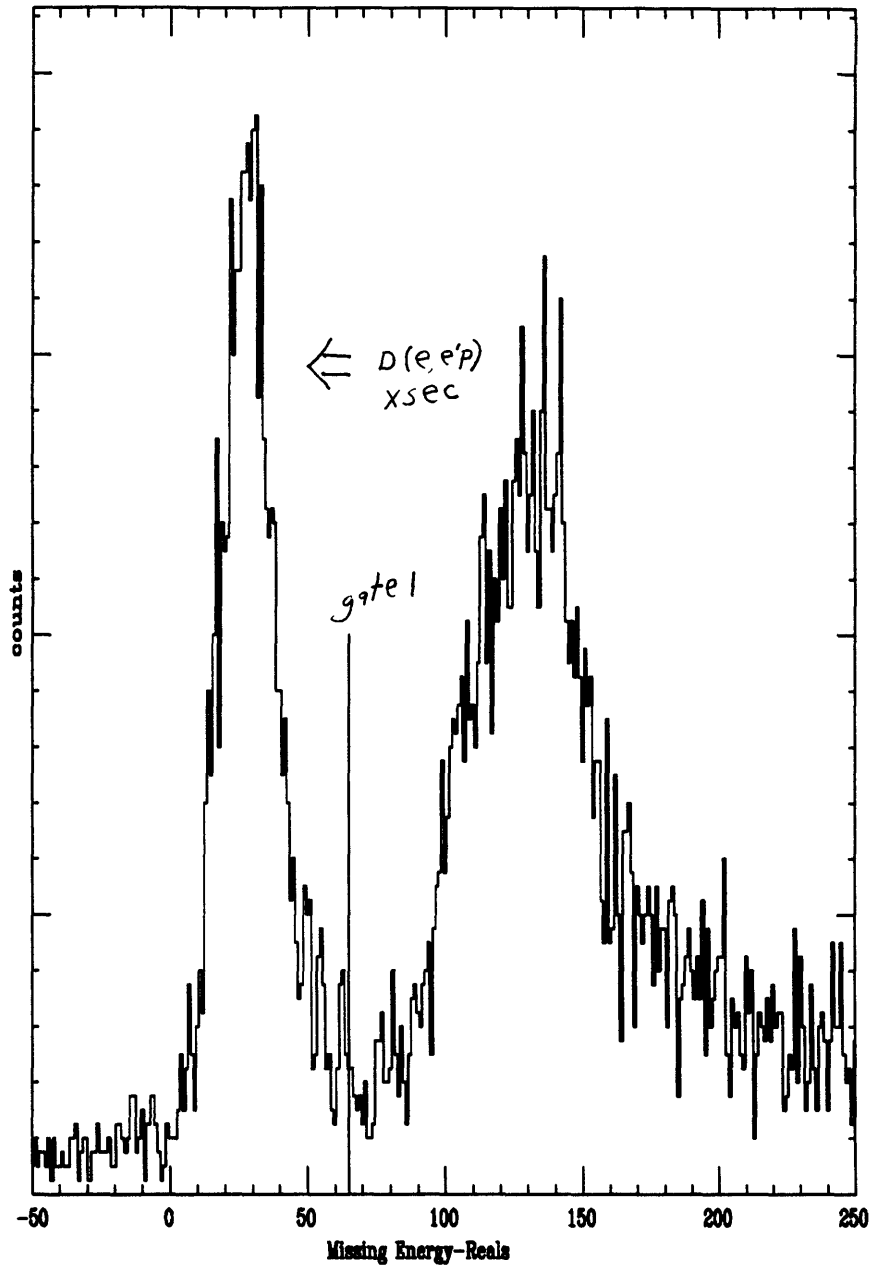
D(e,e'p)
xsec
gate 1
counts
-50
0
50
100
150
200
250
Missing Energy-Reals

Figure 3-32:

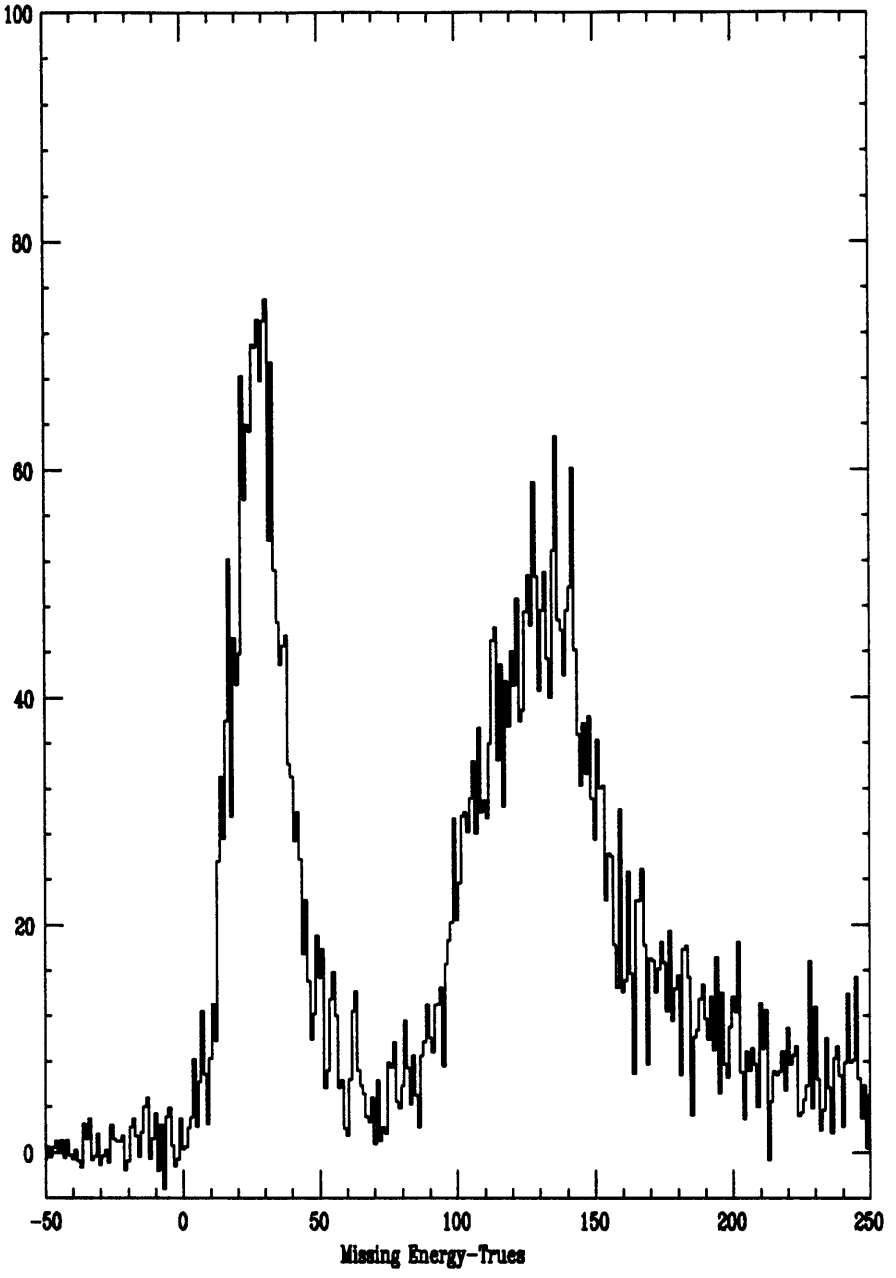

Figure 3-33:

3.7.4 The ELSSY-OOPS 'Good' Event

For the D(e,e'p) data obtained using both spectrometers, events are again divided into two classes:

1. noise events that were not produced by the D(e,e'p) reaction, and
2. 'real' events that were produced by the D(e,e'p) reaction.

Real events are further divided into two classes:

1. 'bad' events that do not have reconstructible trajectories in both spectrometers or are not fully analyzed for other reasons, and
2. 'good' events with fully reconstructible trajectories in both spectrometers that are fully analyzed.

Recalling the definition of our ELSSY 'good' event and of our OOPS 'good' event from sections 3.1.4 and 3.2.7 respectively, the ELSSY-OOPS or coincidence 'good' event is selected as follows:

1. it must be an ELSSY 'good' event
2. it must be an OOPS 'good' event
3. it must fall within the timing peak (gate 1 of figure 3.30), and
4. it must fall to the left of our missing energy cutoff for the Deuteron (gate 1 of figure 3.32).

'Noise' events are separated from 'real' events by assuming that all 'real' events fall within the TOF gate 1 of figure 3.30 and are 'trues', i.e., they are not part of the accidental coincidence background. Also, we assume no 'noise' event is counted as 'true' since these should all be part of the accidental background. We then find the efficiency of these reals by applying the tests of tables 3.6-3.7, seeing how many events are "tossed out" by the test from the TOF histogram, and then adding up all these 'bad' events from all the tests to compute an efficiency for the reals gate, ϵ_r.

test name (OOPS)	test description	typical % real events lost
PU, LAM	no pileup, good LAM (see chapter 2)	1.0
2/3 HDC	info good in at least 2 of 3 HDC's	4.0
Xf_p	x_f in range	0.5
PHI tgt	ϕ_T in range	0.2
THT tgt	θ_T in range	2.7

Table 3.6 OOPS–ELSSY Coincidence Efficiency Tests

We then perform this same procedure for a gate in the accidental region of TOF (fig. 3.30 gate 2). This gives the efficiency for our accidentals, ϵ_a. We then get our 'trues' efficiency using these two efficiencies, the ration of the gates, and the counts in the gates.

$$\begin{aligned} C_r\epsilon_r &= C_a\epsilon_a \cdot \left(\frac{r}{A}\right) + C_t\epsilon_t \\ C_t &= C_r - \left(\frac{r}{a}\right) C_a \end{aligned} \tag{3.42}$$

We then divide our cross section of 'good' events by this number to get the cross section for 'real' events.

$$\sigma_{\text{real}} = \frac{\sigma_{\text{good}}}{\epsilon_t} \tag{3.43}$$

3.7.5 Getting the Cross Section

Ideally, we would get a set of points for many values of missing momentum. We could then quote a cross section and an R_{LT} value for a range of missing momentum. However, for our case the statistics do not allow an accurate cross section measurement for several small bins in p_m. Instead, we must average the cross section over a large bin (25 MeV) in p_m to get a 3% error bar. We can then average Arenhoevel's calculations over the same interval to compare experiment to theory. Other steps include finding $d\Omega_e d\Omega_p d\omega$, the detection volume, as a function of p_m and E_m. Once we have this, we can simply divide the counts in each bin in p_m by this number, add these together, and correct for efficiencies, normalizations, etc. to get the cross section.

test name (ELSSY)	test description	typical % real events lost
PU, LAM	as in OOPS	0.8
TRIG ADC	all trigger ADC's good	0.6
VDC TDC	6 of 6 are good	< 0.1
DL WIRES	3 good wire numbers	< 0.1
LAST WIRE	no events involving last wire on low momentum end of VDC	1.5
GOOD Xf_p	x_f in range	4.0
1/2 TA	at least 1 of 2 TA's has good drift sum	1.5
PHI tgt	ϕ_T in range	0.3
THT tgt	θ_T in range	0.1

Table 3.7 OOPS–ELSSY Coincidence Efficieny Tests - continued

Finding the Detector Volume

I used the code DEEPMONTE [53] to find the detection volume as a function of p_m. This code follows the method of the authors [1]. Given our determined beam energy, DEEPMONTE randomly samples from the electron final energy, the electron target angles, and the proton target angles for each simulated event. Then, using momentum and energy conservation for the reaction, all other kinematic variables are determined. The relevant equations are:

$$\begin{array}{lll} \text{(energy conservation)} & \omega + \epsilon_b = T_p + T_n \\ T_p = \left(\sqrt{P_f^2 + m_p^2}\right) - m_p & T_n = \dfrac{1}{2}\dfrac{p^2 m}{m_n} \\ \text{(momentum conservation)} & \vec{q} + \vec{p}_m = \vec{p}_f \end{array} \tag{3.44}$$

So we input the beam energy, spectrometer momentum and angular acceptances, spectrometer central momentum settings, spectrometer angles, OOPS efficiency profile (some values of p_m being less likely due to the dependence seen in figures 3.17 and 3.19), and limits of p_m we wish to look at. The output is shown in figure 3.34. We also output the results to a lookup table for the cross section calculation. The table tells us the detector volume for each value of missing momentum, and is generated by dividing the counts in a particular p_m bin of figure 3.34 by all the counts in the figure.

Notice from fig. 3.34 that the p_m distribution is significantly broader on the $\phi = \pi$ side than on the $\phi = 0$ side of q. Though we sampled a different range in θ_{pq} on each side of $\vec{q}$, [3] this was not the reason for the different acceptance shapes seen in figure 3.34. The reason was that the $\phi = \pi$ setup and the $\phi = 0$ setup are not symmetric with respect to

[3] This occurred because, at the time of the experiment, we didn't have our most exact determination of the beam energy. Thus we were uncertain as to the exact direction of q, making the placement of OOPS on either side of q at the same value of θ_{pq} a somewhat inexact process. This resulted in a sampling of different values of θ_{pq} on each side. The difference in central value between the π side and the 0 side turned out to be about 0.7°. This accounts for the slight relative shift of the centroids of figure 3.34.

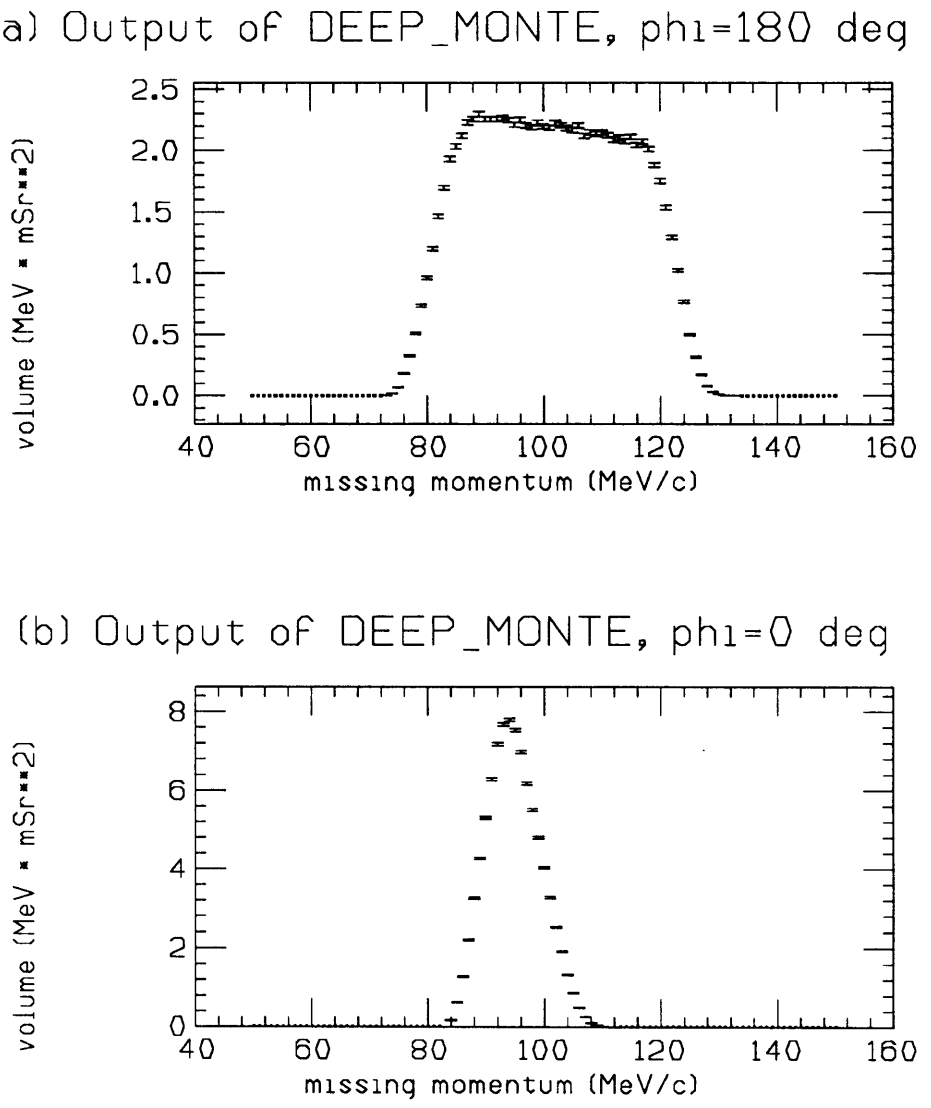

Figure 3-34: The detection volume as a function of p_m on both sides of $\vec{q}$.

the p_m acceptance due to the **asymmetric** behavior of the q vector magnitude. ELSSY's finite acceptance means that $\vec{q}$ will not only have a range of angles, but also a range of magnitudes, with the larger q magnitudes occurring at smaller values of θ_q. In fact, for a given energy transfer, a decrease in θ_q of 0.2^o corresponded to an increase of about 11 MeV/c in the magnitude of $\vec{q}$. This asymmetry led to an asymmetry in the p_m acceptances on either side of $\vec{q}$, which can be inferred from equation 3.44.

It should be noted for the above discussion that we've assumed that the detector volume is "flat" in our region of E_m. That is

$$\left.\frac{\partial}{\partial E_m}\right|_{E_b<E_m<E_b+4M_eV} \Delta\omega\Delta\Omega_e\Delta\Omega_p = 0 \tag{3.45}$$

Where E_b is 2.2 MeV, the Deuteron binding energy.

To check the above assumption we ran DEEPMONTE and randomly sampled different E_m values for each event. We output the results to the histogram shown in figure 3.35. Notice that the distribution is indeed flat throughout a large region, including the interval 2.2 MeV $< E_m <$ 6.2 MeV . Since we restricted our data to this interval in E_m for our cross section calculation, the assumption that the detector volume does not depend on E_m is valid.

Events that are analyzed, occur at $E_m > E_b$, and are unrelated to spectrometer resolution are due to radiative effects and are discussed in chapter 4.

Extracting the Final Cross Sections

Once we had the detector volume as a function of p_m on each side of q, we replayed the data on each side and histogrammed several quantities. One of the most important relationships is shown in figure 3.36. Here we can see that in order to extract a cross section for the same range in p_m on each side of q, we must cut the $\phi = \pi$ side at 81 MeV $< p_m <$ 106 MeV. In addition, we cut the histogram on the same intervals of ω and q on each side of $\vec{q}$ to ensure that all three relevant structure function variables are matched. This will enable us to subtract the two cross sections to find A_ϕ and R_{LT} for the specified range in p_m, ω,

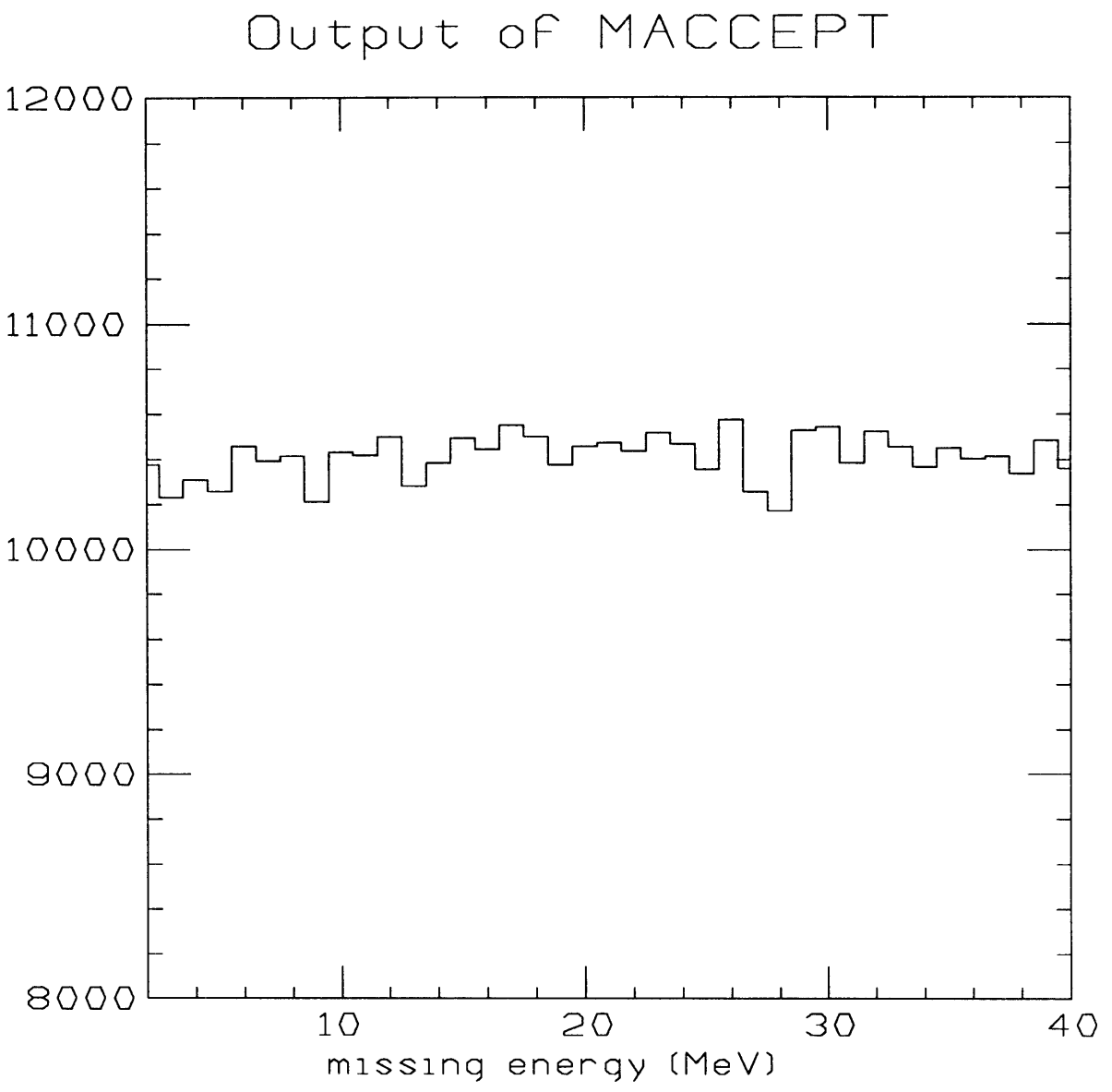

Figure 3-35: Dependence of the detection volume on E_m.

and q using equation 1.17.

kinematic variable	average value	range
q	404 MeV/c	397-410
ω	109 MeV	101-117
p_m	93.5 MeV/c (central value)	81-106

Table 3.8 The acceptances for the final cross sections.

Figure 3.36 is a 'trues' spectrum, i.e., all its points come from a real D(e,e'p) event and not from any accidental coincidence. It was obtained by cutting on the appropriate gates of figure 3.31 and subtracting the resulting histograms as outlined in section 3.7.3.

As mentioned in section 3.7.3, another important spectrum is the missing energy of figure 3.32. We formed one of these spectra on each side of q. We then put a gate at approximately 4 MeV past the Deuteron peak so as not to have our cross section data corrupted by any Carbon events. We then restricted the events in other important histograms, such as in figure 3.36, to have missing energy lower than the cutoff set by the gate. The location of this gate was then an important parameter in the computation of our radiative corrections to the measured D(e,e'p) cross sections (section 4.1).

Given the aforementioned restrictions, we then divided the counts in each bin of p_m by the detector volume for that bin and added these together bin by bin

$$\begin{aligned} \sum_{p_m=81}^{106} \frac{C_{pm}}{\mathrm{vol}_{pm}} &= \tilde{C}^{\mathrm{raw}} \\ \sigma^{\mathrm{raw}} &= \frac{\tilde{C}^{\mathrm{raw}}}{\mathrm{clicks} \cdot \tau \frac{N_0}{2A_D} \cdot (e - /\mathrm{coul}) \cdot \mathrm{tscale}} \end{aligned} \tag{3.46}$$

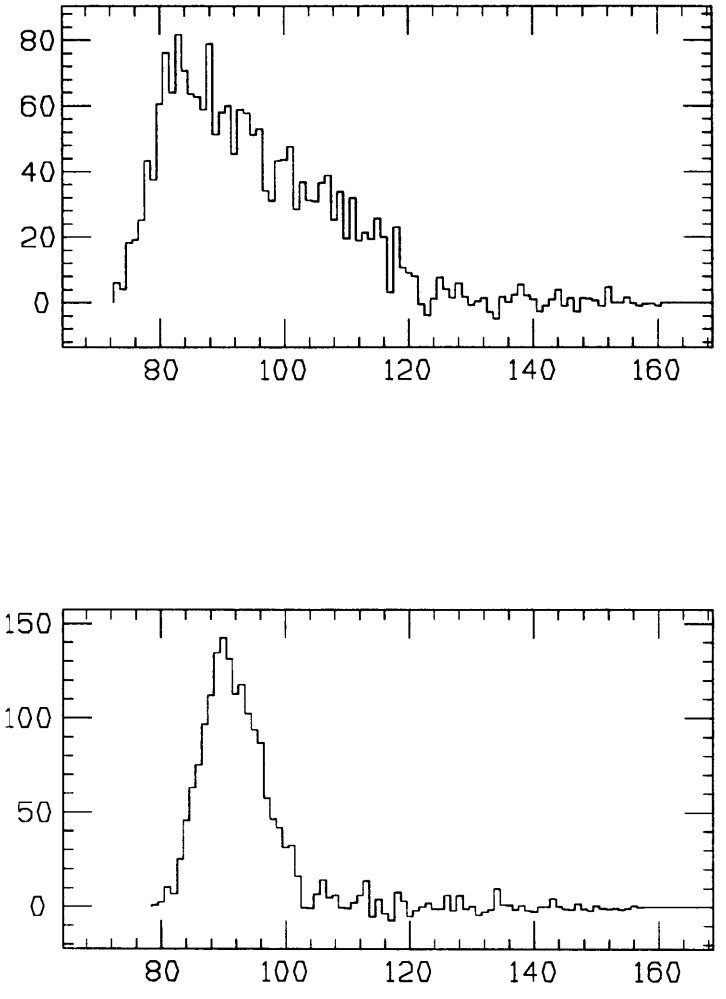

Figure 3-36: Counts vs. missing momentum (MeV/c). $\phi = \pi$ top, $\phi = 0$ bottom.

where

$$\left.\begin{aligned} \text{clicks} &\propto \text{number of coulombs on target} \\ A_D &= \text{atomic weight of Deuterium } \sim 2000 \text{ mg/mole} \\ \text{tscale} &= \text{toroid integrator scale} \\ e-/\text{coul} &= \text{electrons per coulomb } = 1.6 \cdot 10^{-19} \\ \tau &= \text{target thickness in mg/cm}^2 \\ N_0 &= \text{Avogadro's number} \end{aligned}\right\} \tag{3.47}$$

We did this for the data on each side of q giving two cross sections, $\sigma^{\text{raw}}_{\phi=\pi}$ and $\sigma^{\text{raw}}_{\phi=0}$. We then corrected these raw cross sections with the various efficiencies and normalizations defined and discussed in previous sections giving us $\sigma^{\text{corrected}}_{\phi=\pi}$ and $\sigma^{\text{corrected}}_{\phi=0}$.

$$\sigma^{\text{corrected}} = \sigma^{\text{raw}} \left(\frac{N_{\text{OOPS}} \cdot N_{\text{ELSSY}}}{C\_lt \cdot \epsilon_t} \right) \tag{3.48}$$

where

$$C\_lt = \text{ coincidence live time} \tag{3.49}$$

and the final cross sections $\sigma^{\text{final}}_{\phi=\pi}$, $\sigma^{\text{final}}_{\phi=0}$ are then obtained by applying radiative corrections to $\sigma^{\text{corrected}}_{\phi=\pi}$ and $\sigma^{\text{corrected}}_{\phi=\pi}$. The program DEEPCROSS performed most of these tasks dealing with the D(e,e'p) data [54].

Chapter 4

Results and Discussion

In this final chapter I will present the results of our measurements. These will include D(e,e'p) cross sections, the asymmetry, and the structure function R_{LT}. I will then compare these results with the calculations of Arenhoevel averaged over our spectrometer acceptances.

First however, I must discuss one final correction that needs to be made to our measured cross sections.

4.1 Radiative Corrections

$\sigma_{\phi=\pi}{}^{\text{corrected}}$ and $\sigma_{\phi=0}{}^{\text{corrected}}$ from the last chapter would be our final results if not for the fact that electrons radiate in the presence of electromagnetic fields. As alluded to in chapter 1, this fact complicates the analysis of electron scattering experiments. Thus, in order to compare data to theory, either the data must be corrected for these effects or the theory must have these effects added in. The usual procedure in our group is to do the former, i.e. we applied corrections to our data and compared these corrected cross sections to Arenhoevel's cross sections. Therefore, the resulting $\sigma_{\phi=\pi}^{\text{final}}$ and $\sigma_{\phi=0}^{\text{final}}$ were our 'measured' cross sections for the process depicted in figure 4.1, the process we're trying to understand and the one that Arenhoevel produces cross sections for. These radiative corrections are calculable within QED. Before I give the final results, the nature of these radiative corrections will be explained in more depth.

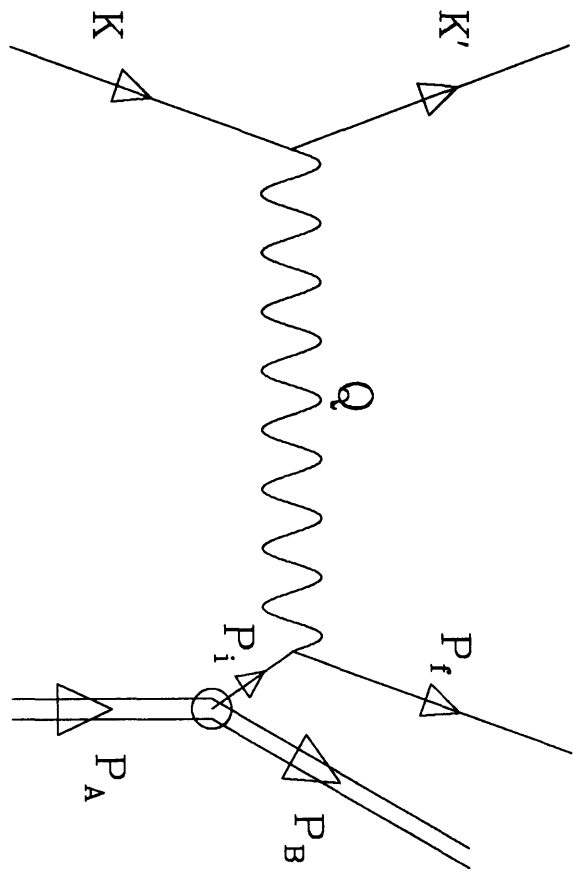

Figure 4-1:

4.1.1 Radiation in the Field of the Target Nucleus

Radiation in the electromagnetic field of the same nucleus that the electron scatters from is called internal bremsstrahlung radiation. We have two such types of radiative corrections. The first type is shown in figures 4.2a and 4.2b. Here, for events where the electron radiates a photon with energy k such that $k > \Delta E$, the experimental resolution (hard photon emission), the events will end up outside of the peak, thus creating a 'radiative tail.' Emission of soft photons, $k < \Delta E$, in diagrams 4.2a and b merely changes the distribution of strength within the peak and does not change the observed cross-section.

The second type of radiative correction includes emission and reabsorption of a virtual photon (see figure 4.2c, d, and e) as well as electron–positron pair creation by the exchanged virtual photon (figure 4.2f). These events will not leave the peak, but may change the observed cross section via renormalization of the electron–virtual photon interaction vertex (4.2e) or virtual photon propagator (4.2f). Note that figures 4.2c and 4.2d merely renormalize the electron mass. Thus, since the calculations utilize the known and measured value of the electron mass, these processes are already included in the cross sections calculated by Arenhoevel. Therefore, these two figures don't contribute to the total radiative correction. All the other processes that change the observed cross section from what we would expect from the two vertex process of figure 4.1, either by producing a radiative tail or by renormalization, can be accounted for by including a multiplicative correction to the observed cross-section. Applying this 'Schwinger correction' then will account for the effects of internal bremsstrahlung radiation on our measured cross section of figure 4.1 [55], [56], [57].

For internal bremsstrahlung radiation in parallel kinematics ($\theta_{pq} = 0$), we use corrections adapted from work by Mo and Tsai for electron scattering from the proton [58], [5]. The single virtual photon exchange D(e,e'p) cross section with internal bremsstrahlung effects corrected for, σ^{final} (what I have also called the two-vertex cross section or process of figure 4.1), and the cross section we measure, $\sigma^{\text{corrected}}$ of chapter 3, are related by

$$\sigma^{\text{final}} = e^{\delta(\Delta E)} \left(1 - \delta'\right)^{-1} \sigma^{\text{corrected}} , \tag{4.1}$$

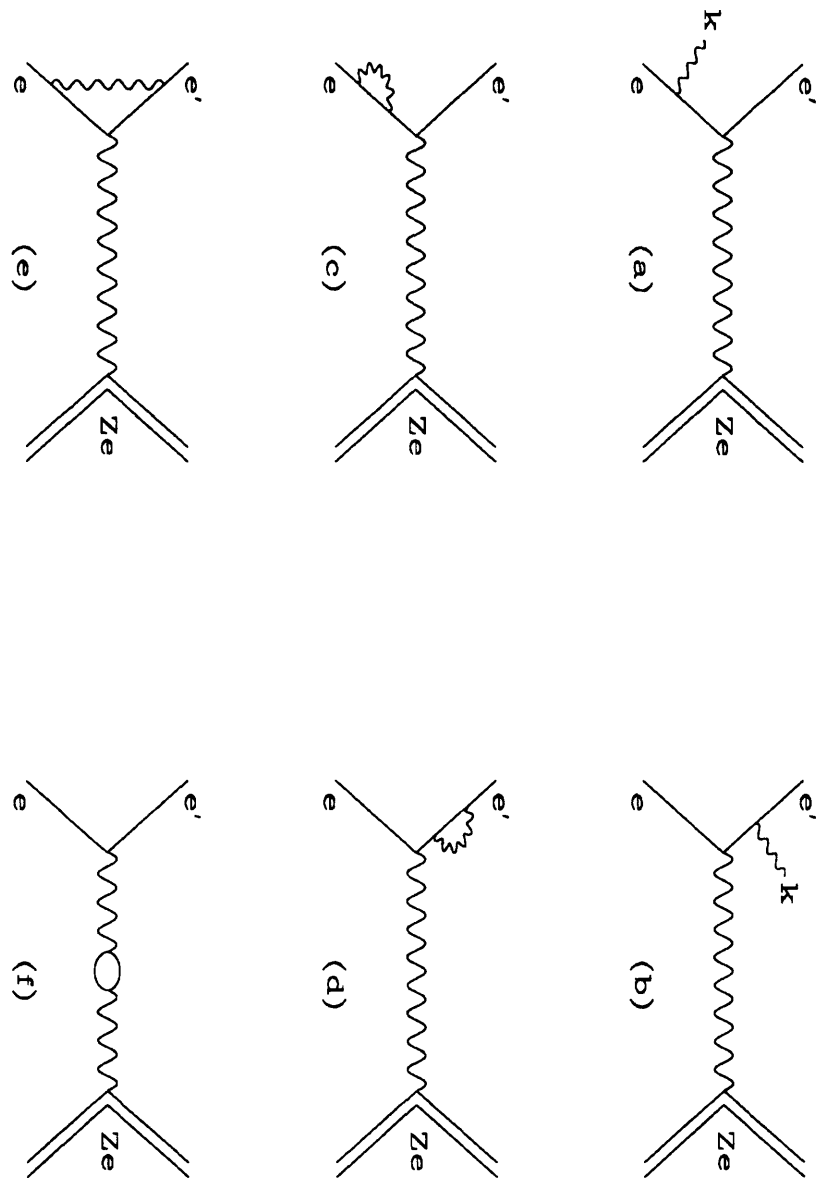

Figure 4-2: Diagrams depicting radiative processes of Internal bremsstrahlung.

where

$$\delta(\Delta E) = \frac{2\alpha}{\pi} \ln\left(\frac{\sqrt{E_0 E_f}}{\Delta E}\right)\left(2\ln\frac{q}{m_e} - 1\right) , \tag{4.2}$$

and

$$\delta' = \frac{2\alpha}{\pi}\left[-\frac{13}{12}\left(2\ln\frac{q}{m_e} - 1\right) + \frac{17}{36} + \frac{1}{4}\ln^2\frac{E_0}{E_f} + \frac{1}{2}\left(\frac{\pi^2}{6} - L_2\left(\cos^2\theta_e/2\right)\right)\right] \tag{4.3}$$

and the Spence function $L_2(x)$ is

$$L_2(x) = \int_0^x \frac{\ln(1-y)}{y} dy . \tag{4.4}$$

The exponential, $e^{\delta(\Delta E)}$, includes the emission of photons to all orders.

It should be pointed out that there is doubt as to whether the above formulas are adequate for our non-parallel kinematics. In fact, a simple geometrical argument would show that for each bin in p_m, the radiation of figures 4.2a-b is emitted with $\vec{q}$ **always** shifted towards the $\phi_{pq} = \pi$ side. This results in an asymmetrical strength in the radiative tail of the $\phi_{pq} = \pi$ side when compared to the $\phi_{pq} = 0$ side. Thus, we would expect a larger correction factor ($\frac{\sigma_{\text{unradiated}}}{\sigma_{\text{radiated}}}$) for the $\phi_{pq} = 0$ side than for the $\phi_{pq} = \pi$ side. Formulas 4.1-4.4 contain no ϕ_{pq} dependence. Therefore, equations 4.1-4.4 give an **incorrect** radaitive correction, especially at our value of $\theta_{pq} = 11°$.

So, rather than use the above formulas, we used corrections produced by the program SIMULATE [59]. SIMULATE took the kinematic and acceptance information specific to our analysis and produced radiated and unradiated missing energy and missing momentum spectra for each side of $\vec{q}$. Cross sections were produced as a function of E_m and p_m using a parameterized Deuteron momentum distribution; and, as in [58], assuming elastic H(e,e'p) inside the Deuteron. The spectra were filled event by event using a Monte Carlo routine. Our total correction factors, including the effects of internal bremsstrahlung, external bremsstrahlung, and Landau straggling (the second and third effects are described in the next section), were then the ratio of the unradiated and radiated strengths between the limits on these spectra that matched the analysis gates we put on the real data (i.e.

table 3.8 with $\Delta E_m = 4MeV$). Thus, the output of SIMULATE gave us two factors, one for the entire acceptance on each side of $\vec{q}$.

4.1.2 Other Radiative Effects

Two other processes reduce the cross-section of a peak. The first process is external bremsstrahlung, radiation in the field of a nucleus other than the one the (e,e'p)reaction took place on. The second process is Landau straggling, energy loss due to ionizing atomic electrons. These processes, since they are caused by external nuclei and atoms, have an effect on the cross-section proportional to the target thickness. Both processes transfer strength from peaks to the continuum. The correction for these effects are due to [60].

The correction factor for peak cross-section losses due to external bremsstrahlung is $e^{-\delta_B}$, where:

$$\delta_B = \frac{t}{x_0 \ln 2} \ln\left(\frac{\Delta E}{E_0}\right) , \tag{4.5}$$

ΔE is the energy bin over which the peak is integrated, E_0 is the incident energy, t is the target thickness in g/cm^2, and $x_0 = 51.2$ g/cm^2 is the radiation length of CD^2, a weighted average of x_0 for Carbon and Deuterium. This equation holds for $\frac{t}{x_0 \ln 2} \ll 1$.

The correction factor for peak cross-section losses due to Landau straggling is $1 - \delta_I$ where:

$$\delta_I = \frac{\lambda + 1}{\lambda(\lambda + \ln \lambda + C)} , \tag{4.6}$$

where C is the Euler-Mascheroni constant (=0.577 ...),

$$\lambda = \frac{\Delta E - e_0}{\xi} , \tag{4.7}$$

$$\xi\,(\text{MeV}) = \frac{0.154}{t\left(\text{g/cm}^2\right)} \cdot \frac{Z}{A} , \tag{4.8}$$

$$e_0 = \xi \left[\ln \frac{\xi}{e'} + 1 - C \right] \tag{4.9}$$

is the most probable energy loss,

$$e' = 2.718 \frac{(1-\beta^2)\, I^2}{2m_e} \tag{4.10}$$

and the average atomic ionization potential is $I = 13.5 \times 10^{-6} \cdot Z$ MeV. These losses, both those due to external bremsstrahlung and Landau straggling, are negligible when compared to those from internal bremsstrahlung. See table 4.1 for all the resulting radiative correction factors.

4.2 Results

We were not able to take enough data to bin at the level of a few Mev/c in p_m. Thus, we were unable to quote a number for the measured R_{LT} at one or several specific values of p_m, q, and ω. Because of this, we chose to integrate our measured cross sections, structure function, and asymmetry over a single p_m bin while doing the same with Arenhoevel's calculations. In this way, we can make a direct comparison to Arenhoevel's theory, though comparison to any other theory would require the same averaging of that theory over the same region in p_m, q, and ω. Likewise, since we integrate R_{LT} over such a large interval in p_m (an interval where the acceptance may vary rapidly), we cannot compare our results directly to those obtained at other labs, as we would need the details of their acceptances (as shown for us in figure 3.34). We don't have this information, so comparison between us and Arenhoevel is all that can be done at this date. We can compare to other labs indirectly by looking at how their data compare to the Arenhoevel calculations.

4.2.1 A_ϕ and R_{LT}

Once we've determined the cross section on both sides of $\vec{q}$, we can easily find R_{LT}. For convenience, I'll rewrite equation 1.17

$$\frac{d^5\sigma}{dw d\Omega_e d\Omega_p} = \frac{\sigma_M}{\eta}\left[v_L R_L(\vec{q},w,\theta_{pq}) + v_T R_T(\vec{q},w,\theta_{pq}) + v_{LT} R_{LT}(\vec{q},w,\theta_{pq})\cos(\phi_{pq}) + v_{TT} R_{TT}(\vec{q},w,\theta_{pq})\cos(2\phi_{pq})\right] \quad (4.11)$$

Then, for each side of $\vec{q}$ we write an equation as above:

$$\sigma_\pi = \frac{\sigma_M}{\eta}\left[v_L R_L(\vec{q},w,\theta_{pq}) + v_T R_T(\vec{q},w,\theta_{pq}) - v_{LT} R_{LT}(\vec{q},w,\theta_{pq}) + v_{TT} R_{TT}(\vec{q},w,\theta_{pq})\right] \quad (4.12)$$

and

$$\sigma_0 = \frac{\sigma_M}{\eta}\left[v_L R_L(\vec{q},w,\theta_{pq}) + v_T R_T(\vec{q},w,\theta_{pq}) + v_{LT} R_{LT}(\vec{q},w,\theta_{pq}) + v_{TT} R_{TT}(\vec{q},w,\theta_{pq})\right] \quad (4.13)$$

I now introduce the quantity $\sigma_{\rm diff}$:

$$\sigma_{\rm diff} = \sigma_\pi - \sigma_0$$

Subtracting equations 4.12 and 4.13 then yields

$$R_{LT} = \frac{-\eta(\sigma_{\rm diff})}{2\sigma_M v_{LT}} , \quad (4.14)$$

we can also define a quantity A_ϕ:

$$A_\phi = \frac{\sigma_0 - \sigma_\pi}{\sigma_0 + \sigma_\pi} . \quad (4.15)$$

Then we have

$$R_{LT} = \frac{\eta A_\phi(\sigma_0 + \sigma_\pi)}{2\sigma_M v_{LT}} . \quad (4.16)$$

A_ϕ is useful in that it may be much less sensitive to the many theoretical uncertainties inherent in describing the Deuteron initial state, np scattering final state, and nuclear current that arise when trying to predict the absolute cross section [61]. It can be seen from eq. 4.15 that if this uncertainty is almost the same (say, as a percentage of the final cross section) for both sides of $\vec{q}$, this uncertainty may nearly vanish for A_ϕ but will remain essentially undiminished for R_{LT}. Of course, this also means that A_ϕ contains less physics than R_{LT}. However, at this stage of theoretical sophistication, A_ϕ may be better able than R_{LT} to eliminate certain theories in favor of others. Table 4.1 shows our final results for A_ϕ and R_{LT}.

4.2.2 The Final Cross Sections

ϕ_{pq}	IB	EB and Landau	$\sigma^{\text{corrected}}$	σ^{final}	R_{LT}	$A_\phi(\%)$
π	1.259	1.009	498 ± 15	627 ± 19	0.97 ± 0.12	-20.7 ± 2.7
0	1.291	1.007	317 ± 15	412 ± 19		

Table 4.1: Final results for the R_{LT} extraction. **IB** and **EB** are, respectively, the internal and external bremsstrahlung corrections. Cross sections in the same units as in figures 4.3 and 4.4; R_{LT} in same units as figure 4.6. The errors shown are statistical only. See table 4.3 for the values of total uncertainty on our measurements

The final values of our measured cross sections on either side of $\vec{q}$ are listed in table 4.1. All the corrections detailed in chapter 3 have been made, as well as radiative corrections. The ratio $\frac{\mathrm{D(e,e'p)_{meas}}}{\mathrm{D(e,e'p)_{Arenhoevel(T)}}}$ (equivalent to the ratio DATA/N+MEC+IC of figures 4.3 and 4.4) that we determine (DATA/N+MEC+IC=0.67-0.75)is consistent with previous measurements in this range of p_m (see figure 1.12 and [19]).

4.3 Systematic Error

There are many sources of systematic error in these measurements. These are entered in table 4.2. The largest source of systematic error is uncertainty in the detection volume table entries when OOPS is at 64.7°. This is largely due to the 1 MeV uncertainty in the beam

energy. Of course, this same beam energy uncertainty leads to a very small systematic error in the volume table entries when OOPS is at 42.9°. This is probably due to the fact that at 42.9° the p_m distribution used to get the $\phi = 0$ cross section is peaked, while at 64.7° the distribution is 'flattened' because it is cut to match the p_m acceptance at 42.9°. An uncertainty in the beam energy will thus effect the two sides in different ways. Both acceptances will be broadened (squished) slightly when the beam energy is changed a little ($\pm$ 1MeV), but the 42.9° acceptance will have area added or subtracted at its tails while the **truncated** 64.7° acceptance will have its area change by a much greater proportion due to its steeper sides.

Table 4.2: Systematic Errors

Source	$\Delta\sigma_\pi$ (%)	$\Delta\sigma_0$ (%)	ΔR_{LT} (%)	ΔA_ϕ (%)
ELSSY norm(E_0)	0.5	0.5	0.5	0
ELSSY norm(θ_e)	0.3	0.3	0.3	0
$D(e,e')_{Platchkov}$	2	2	2	0
$D(e,e')_{Bates}$	1.6	2.2	0.4	1.4
$D(e,e')_{Targetpos}$	1.3	1.9	0	1.4
OOPS norm	1.5	1.5	1.5	0
Beam Current	0.5	0.5	0.5	0
Detection Volume	4.9	0.3	14	10.6
Total	5.9	3.9	14.2	10.8

Another significant source of error was the uncertainty in our target thickness. Since we normalized our D(e,e') cross sections to those of [51], we first had to include about a 2% error for their measured cross sections. We then included another 2% to account for uncertainties in our D(e,e') measurements and uncertainty in the fit shown in figure 3.26. We also included a systematic error having to do with whether we should have fit the points to a straight line, as is shown in figure 3.26, or whether we should have assumed some beam-on-target shift from one group of runs to the next. This latter assumption would mean that the points of figure 3.26 should be fit to a family of two or more lines

having different y-axis intercepts. The cross sections were computed both ways yielding a difference of about 1.5% between the two methods, resulting in the systematic error entries of the row $D(e,e')_{Targetpos}$ in table 4.2.

The other contributions to the overall systematic error were small, except for the error in the OOPS normalization of 1.5%. This error is a combination of uncertainties in the measured H(e,e'p) cross sections and in the output of REVMOC [45] (see discussion of OOPS normalization, chapter 3).

As seen from table 4.2, the total systematic error in A_ϕ was about 10.8%. Adding total systematic error and total statistical error (which was 12.8% for A_ϕ, table 4.1) in quadrature yields a total uncertainty in our value of A_ϕ of about 16.7%, still small enough for the Arenhoevel total non-relativistic calculation (N+MEC+IC) to lie 1.3 standard deviations above the measured A_ϕ. The total uncertainty on the other observables is displayed in table 4.3.

data(or calculation)	ϕ_{pq}	σ^{final}	R_{LT}	$A_\phi(\%)$
data	π	627 ± 42	0.97 ± 0.19	-20.7 ± 3.5
data	0	412 ± 25		
PWBA	π	1000	1.10	-13.8
PWBA	0	757		
N	π	806	1.00	-15.8
N	0	586		
N+MEC+IC	π	830	1.05	-16.2
N+MEC+IC	0	598		
N+MEC+IC+RC	π	821	1.27	-20.6
N+MEC+IC+RC	0	541		

Table 4.3: Final results including total uncertainties. The total uncertainties displayed were obtained by adding total statistical and total systematic errors in quadrature. Once again, cross sections in units of figures 4.3-4.4, R_{LT} in units of figure 4.6

4.4 Comparison to the Arenhoevel Calculation

Once we had the final results for the measured cross sections and structure function, we averaged Arenhoevel's calculations over the same ranges in p_m, q, and ω on each side of $\vec{q}$ (see table 3.8). We then had cross sections, an asymmetry, and a structure function that depended on which of the processes in figures 1.4-1.8 we included in the calculation. We calculated the following types of Arenhoevel cross sections and structure functions for comparison to data:

1. The PWBA non-relativistic,
2. those involving the normal (N) non-relativistic calculation,
3. the full non-relativistic calculation including meson-exchange and isobar contributions (N+MEC+IC), and,
4. the total calculation including meson-exchange, isobar configurations, and relativistic corrections (N+MEC+IC+RC).

The results are plotted and compared to our data in figures 4.5 and 4.6 for A_ϕ and R_{LT} respectively.

4.5 Discussion

We notice immediately that our results are consistent with those of Saclay. Our measured R_{LT} falls within error bars of the Arenhoevel non-relativistic theory. It is low compared to the theory with relativistic corrections by about the same amount that the Saclay results are low. This situation contrasts with the measurements taken at NIKHEF, where R_{LT} was found to lie above the non-relativistic theory and to fall within error bars of Tjon's fully relativistic theory. Of course, as was concluded in [22] the NIKHEF measurements do not rule out the non-relativistic theory. Figure 1.14 does show however that the NIKHEF data **prefer** the relativistic calculation of Tjon.

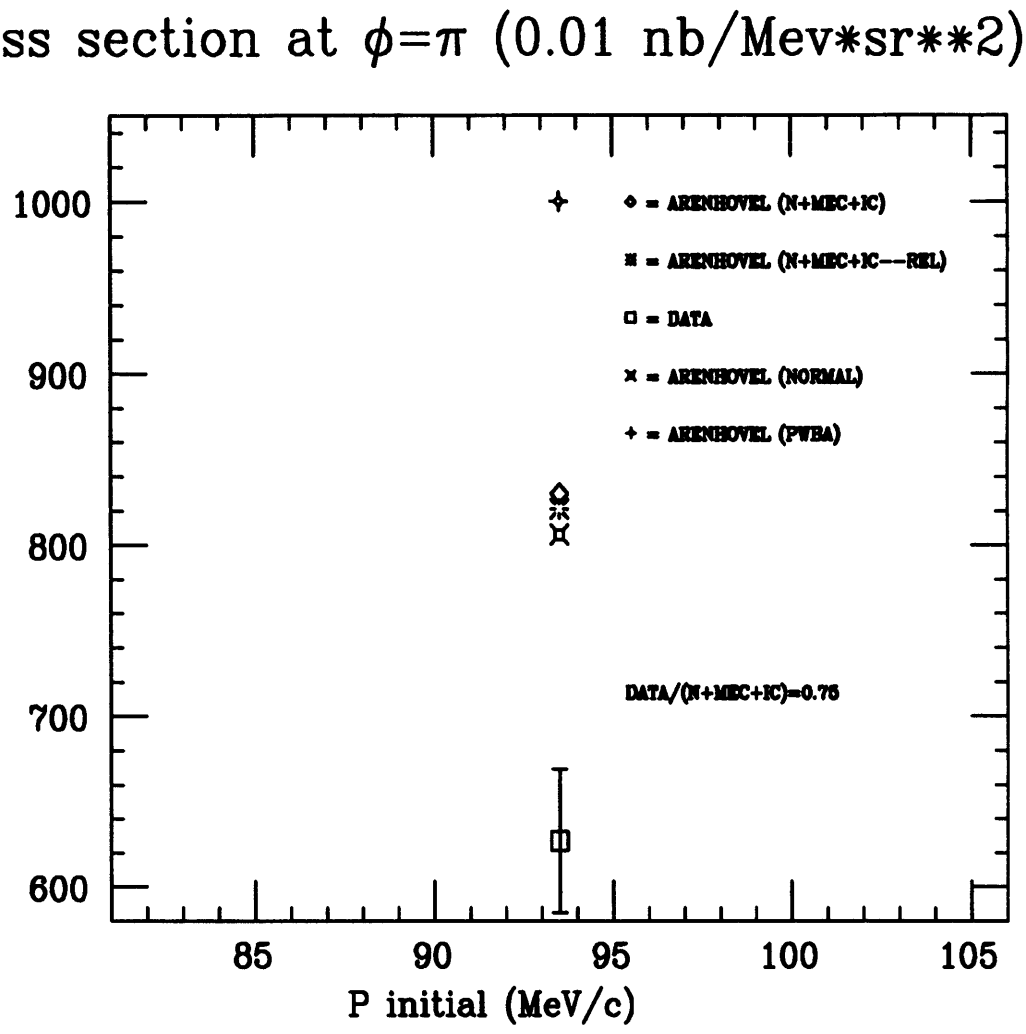

Figure 4-3: Note that figures 4.3-4.6 show results for one wide bin in $P_{initial}$ of 81-106 MeV/c, our p_m acceptance for our analysis. All results are then plotted at a value of 93.5 MeV/c, the center of the bin. Error bars in figures 4.3-4.6 are total uncertainty; statistical + systematic (table 4.3)

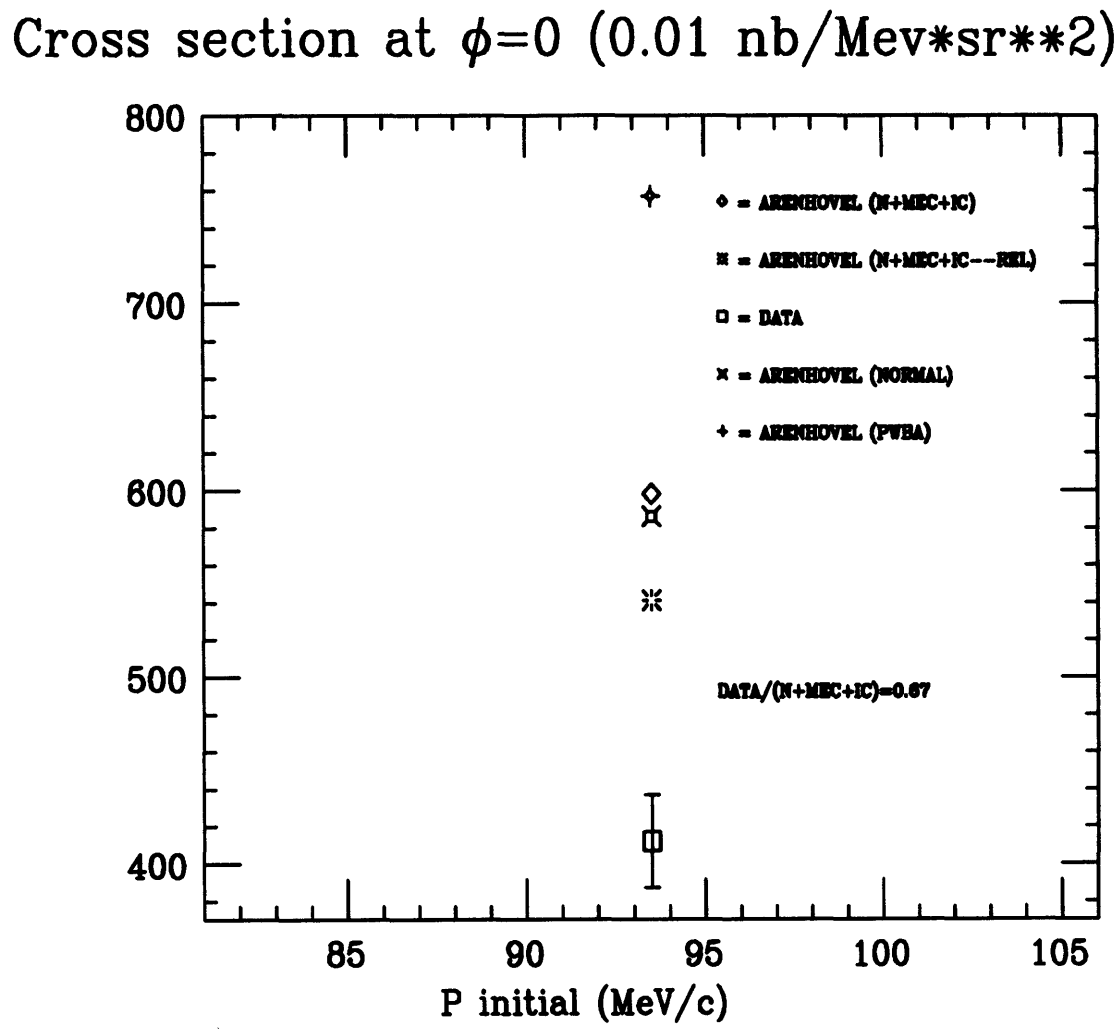
Cross section at ϕ=0 (0.01 nb/Mev*sr**2)
800
700
600
500
400
85
90
95
100
105
P initial (MeV/c)
◇ = ARENHOVEL (N+MEC+IC)
* = ARENHOVEL (N+MEC+IC--REL)
□ = DATA
× = ARENHOVEL (NORMAL)
+ = ARENHOVEL (PWBA)
DATA/(N+MEC+IC)=0.67

Figure 4-4:

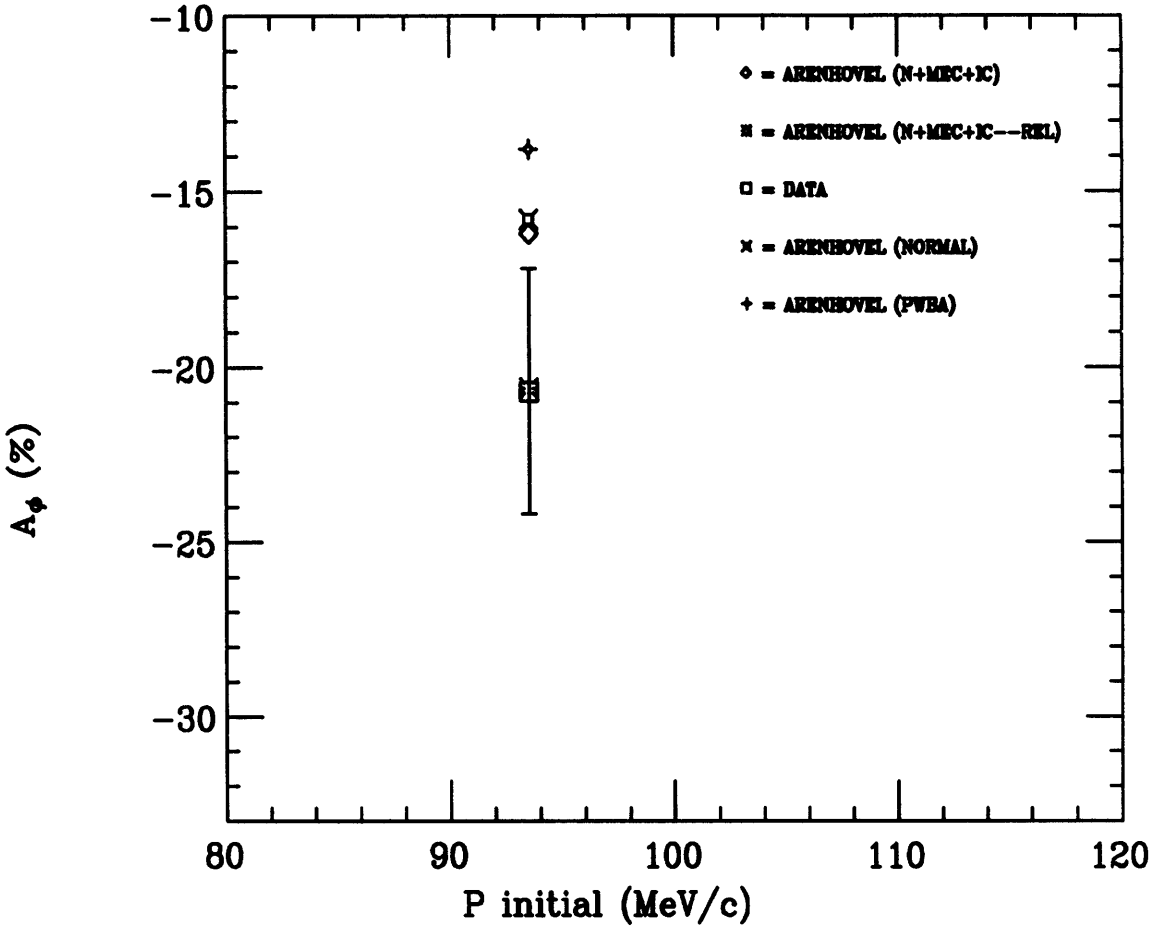

Figure 4-5: Our asymmetry measurement compared to the Arenhoevel calculation.

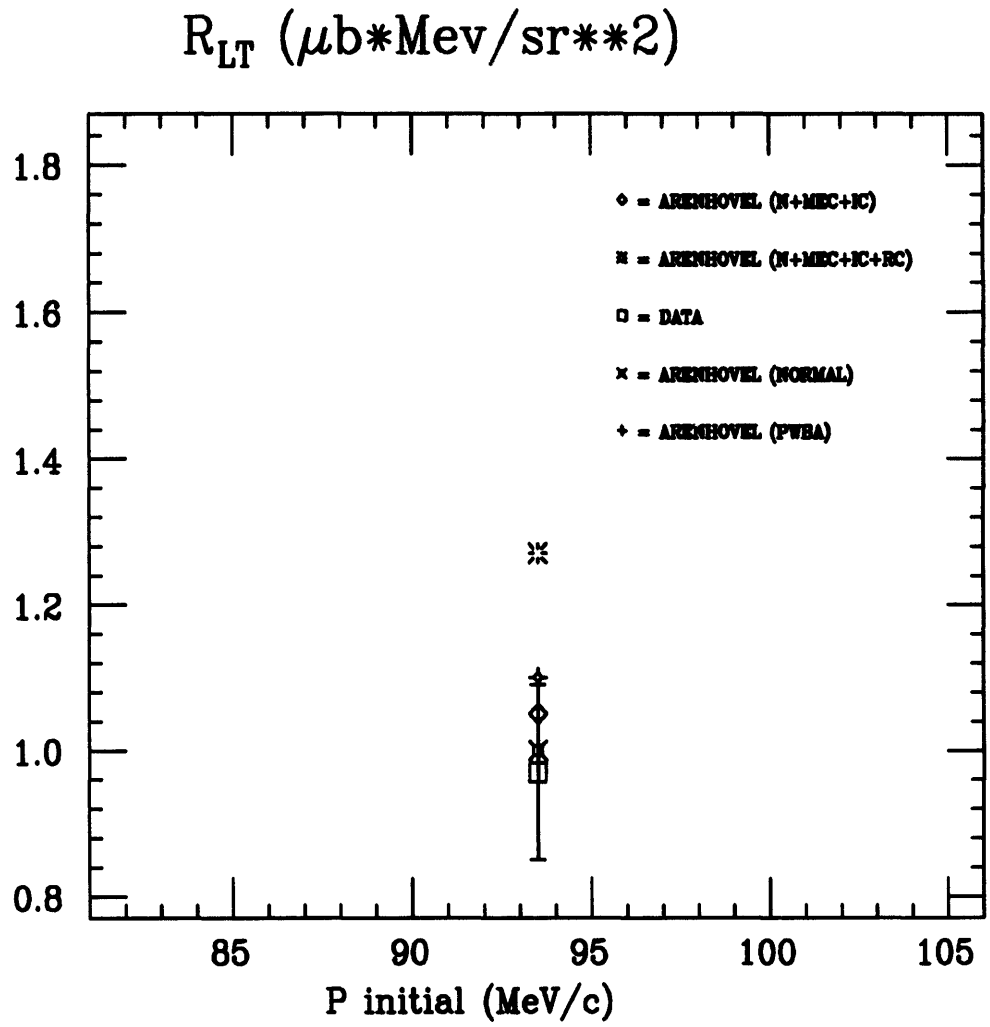

Figure 4-6: Our measurement of R_{LT} compared to the Arenhoevel calculation.

Looking at figures 4.3-4.6, we see that the multipole expansion technique that accounts for the final state interactions corrects the observable by 10 to 25%, and in the right direction, i.e. towards the data point. This is seen in the difference between the N and PWBA points in the plots. Also, again looking at figures 4.3-4.6, we see that the addition of MEC and IC to the normal theory N causes an insignificant change in the observables; no more than a couple percent at most. This is what we expect for our kinematics, as we sit on the quasi-elastic ridge. Clearly, the important factor in the R_{LT} and A_ϕ calculations is the inclusion of relativistic corrections. This is the only factor that produces a difference in the calculations that is bigger than the experimental uncertainty.

Regarding A_ϕ, we see a somewhat different situation than for R_{LT}. Our measurement of A_ϕ indicates a preference of this observable for the relativistic calculations. Which then should we believe, the R_{LT} results, or those for A_ϕ? Well, as previously alluded to, certain classes of theoretical uncertainties affect both σ_0 and σ_π in roughly the same amounts. Thus, at least these types of theoretical sensitivities will be diminished when looking at A_ϕ, while when looking at a cross section or structure function they will remain more or less undiminished. Such uncertainties include incorrect spinor normalizations due to the non-relativistic approximations used, as well as nucleon form factor uncertainties. In addition, choice of N-N potential, and inclusion of MEC, IC, and FSI should effect the cross section on both sides of $\vec{q}$ in roughly the same proportion. In contrast, looking at the expressions for the relativistic terms added to the current in RC [12], it can be seen that inclusion of these terms could very well produce an asymmetrical effect. This is what we observe (figures 4.3-4.5). Thus, even though the structure function R_{LT} is an important part of the Deuteron 'puzzle' (the fact remains that all structure functions must be measured to provide the most stringent constraint on theory), A_ϕ is less sensitive to several uncertainties in the calculations than either the cross sections or R_{LT}. Thus, considering the results of this measurement alone, the best observable for testing the validity of the relativistic contributions to the Arenhoevel calculations may very well be A_ϕ.

4.6 Conclusions

In summary, the following points may be asserted as a result of our measurement of the Deuteron R_{LT}:

1. Our measured cross sections are reasonable and consistent with previous measurements taken at Saclay, further evidencing that the first OOPS module is a well functioning spectrometer.

2. Our measurement shows an overestimation of the total cross section by Arenhoevel on both sides of $\vec{q}$. Our measurement is consistent with the measurements of Bernheim at these values of p_m.

3. Our measurement shows evidence that the Arenhoevel relativistic theory may be inadequate, as the measured R_{LT} seems to **prefer** the non-relativistic calculation. This is not a strong preference.

4. Our measurement shows evidence that the Arenhoevel non-relativistic theory may be inadequate, as the measured A_ϕ seems to **prefer** the relativistic calculation. Once again, this is not a strong preference, as the non-relativistic point lies only 1.3 standard deviations in total uncertainty above the data point. Thus, no definite conclusion regarding a comparison between the non-relativistic calculation and the relativistic calculation can be drawn based on this experiment alone. A reasonable conjecture is that since A_ϕ is likely to be less sensitive to theoretical ambiguities that R_{LT}, the measured A_ϕ is a better test for the current generation of Deuteron models than R_{LT}. Thus, we may **conjecture** that our data show a preference for the relativistic calculations.

5. Our measurement demonstrates the importance of the multipole expansion technique for the accurate accounting of final state interactions for the cross sections, asymmetry, and structure function. The expansion corrects the prediction by 10 to 25% **in the right direction**.

4.7 The Future

Theorists may take direction from the fact that three recent experiments (Saclay, NIKHEF, and MIT) have shown that A_ϕ prefers a relativistic Deuteron description, be it fully relativistic (Tjon) or a corrected nonrelativistic theory (Arenhoevel). Tjon's theory could be averaged over our acceptances to see how it compares with the Arenhoevel relativistic calculation. Tjon and Arenhoevel could also directly compare their results and both could compare to measurements taken at other kinematics to see how the current operator expansion method (Arenhoevel) compares to a solution of the Bethe-Salpeter equation(Tjon) over a wide kinematic range. Many expect the expansion to fail at higher missing momenta and especially at higher momentum transfers, since these are the variables that the current is expanded in [62].

On the experimental side, and as previously stated in chapter 1, this experiment is only a small part of a much more ambitious program to measure all Deuterium structure functions in various kinematics. Included in these measurements, along with those of the four unpolarized structure functions, will be many measurements of the 'fifth' and other polarization structure functions. A focal plane polarimeter has been built to measure some of the 18 structure functions that compose the polarized electron (incoming) and polarized outgoing proton coincidence cross section.

In addition, Construction of more OOPS modules will enable reduction in systematic error and required luminosity by using 2-4 OOPS modules at a time to simultaneously measure coincidence cross sections at different θ_{pq} and ϕ_{pq} (figure 4.7). It is clear that these future developments, when incorporated in an experiment performed with a much higher duty factor beam (e.g. such as will exist at Bates very soon or at the Continuous Electron Beam Accelerator Facility-CEBAF, which will be completed in the next year or two). The new stretcher ring at Bates will provide duty factors of as high as 80% while CEBAF will provide a 100% duty factor beam. We ran at a duty factor of about 1%. Since the accidentals to reals ratio scales inversely with the duty factor, future experiments

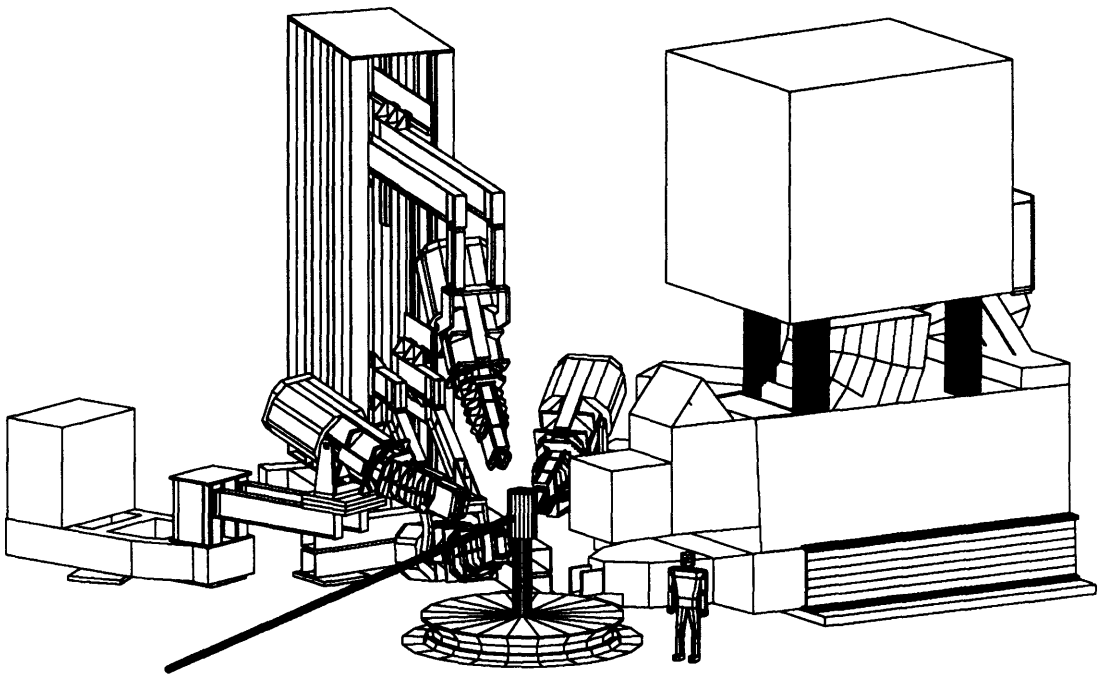

Figure 4-7: Drawing of a multi-OOPS system.

could run with much lower accidental count rate. [1] This experimental capability, combined with the opportunity to run for a several weeks instead of a few days, will enable future experimenters to measure cross sections to less than 1% in statistical uncertainty at a bin size of a couple of MeV/c in p_m. This will result in structure function and asymmetry measurements having statistical error of a few % or less. Such measurements will then have a total uncertainty driven by the total systematic error much more than the statistical. In particular, The beam energy uncertainty will fall by a factor of at least 100 for experiments performed at CEBAF [63]. [2] Notice from table 4.2 that virtually all of the total systematic error in A_ϕ and in R_{LT} is incurred by the acceptance volume uncertainty, which is directly related to our beam energy uncertainty of 1 MeV. A beam energy that is much better known, combined with an experimental technique that matches the p_m acceptances better on either side of $\vec{q}$, could result in a **total measurement precision of 1%** or less. When this point is reached, which could be in a few years, the uncertainties in comparison between theory and experiment in this field will be much more a question of theoretical technique than measurement precision. In other words, many calculations will be able to be ruled out completely by precise measurements; the theorist seeing much more clearly which calculational methods are more accurate than others.

The results of these experiments will hopefully be able to place many more constraints on the Deuteron model and its currents. This in turn will render significant information on the interaction responsible for nuclear structure in general.

[1] Our accidentals/reals ratio was 0.2-0.4 depending on which side of $\vec{q}$ we were at, i.e. the corresponding CEBAF experiment would run at 0.02-0.04 accidentals/reals ratio.

[2] CEBAF will run mainly at momentum transfers much greater than ours of 400 MeV/c; but the laboratory at Mainz is currently measuring D(e,e'p) and can measure the beam energy to within 0.02-0.03 %.

Bibliography

[1] S. Frullani and J. Mougey, *Advances in Nuclear Physics*, vol. 14, ed. by J.W. Negele and E. Vogt, Plenum Press, New York (1984).

[2] T. de Forest Jr. and J.D. Walecka, *Adv Phys* **15**, 1 (1966).

[3] T.W. Donnelly, "Electromagnetic and Weak Currents in Nuclei," in **Symmetries in Nuclear Structure**, ed K. Abrahams *et alia*, Plenum Publishing Corp. (1983).

[4] T. DeForest, *Annals of Physics* **45**, 365 (1967).

[5] L. Weinstein, Ph.D. Thesis M.I.T. (1988), unpublished.

[6] T. de Forest, *Nucl Phys* **A392**, 232 (1983).

[7] W. Fabian and H. Arenhoevel, *Nucl Phys* **A314**, 253 (1979).

[8] H. Arenhoevel, *Nucl Phys* **A384**, 287 (1982).

[9] J. M. Laget, *Phys Lett B* **199**, 493 (1987).

[10] F. M. Renard *et alia*, *Nuovo Cimento* **38**, 1688 (1965).

[11] J. Tjon, *Nucl Phys* **A543**, 243c (1992).

[12] G. Beck and H. Arenhoevel, *Few Body Systems* **13**, 165 (1992).

[13] J. M. Blatt and L. C. Biedenharn, *Phys Rev* **86**, 399 (1952).

[14] A. J. F. Siegert, *Phys Rev* **52**, 787 (1937).

[15] H. Arenhoevel, *Chinese Journal of Phys* **30(No.1)**, 17 (1992).

[16] S. Aufret, *et alia Phys Rev Lett* **55**, 1362 (1986).

[17] W. Schmitt, Ph.D. Thesis M.I.T. (1993), unpublished.

[18] N. Makins *et alia*, *Phys Rev Lett* **March** (1994).

[19] M. Bernheim, *et alia Nucl Phys* **A365**, 349 (1981).

[20] S. Turck-Chieze, *et alia Phys Lett* **142B**, 145 (1984).

[21] M. van der Schaar, *et alia Phys Rev Lett* **68**, 776 (1992).

[22] M. van der Schaar, Ph.D. Thesis, Utrecht (1991).

[23] B. Mosconi and P. Ricci, *Nucl Phys* **A517**, 483 (1990).

[24] M. van der Schaar, *et alia Phys Rev Lett* **66**, 2855 (1991).

[25] D. Jordan, Ph.D. Thesis, MIT (1993), unpublished.

[26] Jean-Eric Ducret, Ph.D. Thesis, University of Paris-Orsay (1992), unpublished.

[27] Jean-Eric Ducret, *et alia Nucl Phys* **A553**, 697c (1993).

[28] L. Lakehal-Ayat, *et alia Nucl Phys* **A553**, 693c (1993).

[29] W. Bertozzi *et alia*, *Nucl Inst Meth* **162**, 211 (1979).

[30] W. Bertozzi *et alia*, *Nucl Inst Meth* **141**, 457 (1977).

[31] N. Nayestanaki, Ph.D. Thesis M.I.T. (1986), unpublished.

[32] V. Bhushan, S.M. Thesis M.I.T. (1992), unpublished.

[33] S. Dolfini, J. Mandeville, *OOPS Design Report*, Illinois Internal Report.

[34] D. Jordan *et alia*, *Nucl Inst Meth* in preparation.

[35] L. G. Atencio *et alia*, *Nucl Inst Meth* **187**, 381 (1981).

[36] A. H. Walenta, *Nucl Inst Meth* **151**, 461 (1978).

[37] LAMPF MP-1 documents on VAX VMS Q system.

[38] The on–line analyzer was written by M. Holtrop.

[39] D. Jordan, S. Gilad, M. Holtrop, T. Mcilvain, W. Schmitt, L. Weinstein, *Understanding the ELSSY VDC*, Bates Internal Report.

[40] D. Beck, Ph.D. Thesis, MIT (1986).

[41] K. Dow, Ph.D. Thesis, MIT (1987).

[42] J.J. Kelly, Ph.D. Thesis, MIT (1981).

[43] G.G. Simon *et alia*, *Nucl Phys* **A333**, 381 (1980).

[44] DRT, a LAMPF MP-10 routine

[45] C. Kost and P. Reeve, REVMOC, *A Monte Carlo Beam Transport Program*, TRI-UMF(1985), TRI-DN-82-28.

[46] L. Weinstein, *private communication*, RELEFF originally written by H. Baghaei.

[47] J. Mandeville and S. Dolfini, *private communication.*

[48] D. C. Carey, K. L. Brown, and Ch. Iselin, Decay TURTLE, *A Computer program for Simulating Charged Particle Beam Transport Systems, Including Decay Calculations*, Fermilab(1982), PM-31.

[49] M. Holtrop, D. Jordan, T. Mcilvain, V. Bhushan, L. Weinstein, *The ELSSY Matrix Elements*, Bates Internal Report.

[50] J. Mandeville *et alia*, *Measured Properties of the OOPS Spectrometer*, Illinois Internal Report.

[51] S. Platchkov *et alia*, *Nucl Phys A* **510**, 740 (1990).

[52] R.W.Lourie, Ph.D. Thesis, MIT (1986); P.E. Ulmer, Ph.D. Thesis, MIT (1987); and L. Weinstein, Ph.D. Thesis, MIT (1988).

[53] DEEPMONTE, written by D. Jordan (1992).

[54] DEEPCROSS, written by D. Jordan (1993).

[55] E. Borie and D. Drechsel, *Nucl Phys* **A167**, 369, (1971).

[56] C. De Calan and G. Fuchs, *IL NUOVO CIMENTO* **vol. 38**, 1594, (1965).

[57] L. Maximon, *Rev Mod Phys*, **41**, 193, (1969).

[58] L. W. Mo and Y. S. Tsai, *Rev Mod Phys* **41**, 205, (1969).

[59] N. Makins, Ph.D. Thesis, MIT, in preparation.

[60] J. Bergstrom, *Medium Energy Nuclear Physics with Electron linear Accelerators*, MIT Summer Study, (1967).

[61] T. Donnelly, *private communication.*

[62] T. Donnelly, *private communication*

[63] S. Gilad, *private communication*

Acknowledgments

I hardly know where to start. I don't want to be overly effusive in my display of gratitude, it's frowned on by my people. I owe debts of both friendship and apprenticeship, sometimes both to the same person.

I'd like to thank Bill Bertozzi for his support. Bill possesses uncanny physical insight. This is one major reason why his research group is so productive. He also hires good staff members to carry out the group's research agenda. A few of these 'post-docs' and other staff have been especially helpful to me during my stay in the group. Larry Weinstein was an especially good teacher in everything from experimental techniques to helping me prepare for my oral. I certainly missed his constant input during the last 18 months. Shalev Gilad was also a great help to me during the experiment and during data analysis. I'd like to thank him for his help with my thesis. Bill Donnelly provided me with invaluable theoretical insight, insight I could only get from our long discussions in his office during the last 8 months. John Morrison could usually answer any generic theoretical question. Maurik Holtrop and Steve Penn were also a great help with all aspects of my education and progress in this group. They were good people to grab to answer any question, especially those concerning experimental technique and data analysis. I should also thank Steve, Maurik, and Adam Sarty for helping me get a good nights sleep on ocassion. Here I'm being vague, but its an inside joke (and not a very funny one). J. Chen, June Matthews, Dan Dale, Steve Dolfini, Joe Mandeville, Werner Boeglin, and George Sechen have all given me advice and assistance spanning every activity I've been involved with at LNS. I'd also like to thank the staff at Bates for their hard work, especially during my experiment. Likewise for the LNS computer staff. The MIT facilities were top notch. Speaking of computing, I'd like to thank Vipul Bhushan for his help with LaTeX. He made the use of these programs less painful. Lastly, I'd like to thank Dave Jordan. The data analysis, in particular, would have been much more difficult without his efforts. Our collaboration on the Deuterium data was very helpful to me.

Now let's consider the friends I've made. As has been written before at the end of theses, "the pursuit of physics is done most effectively in a group situation", or something like that. There may be exceptions to this platitude. Such as if the group is comprised of inanimate objects. Oh, there I go again trying to be so damn 'exact'. Sorry; after all, I can relax now that I've finished my Ph.D. I can go back to my 'fuzzy' mode of thinking.

Larry Weinstein was often good for interesting discussions of history, economics, religion and various other topics. The same was true for for Steve Penn. My conversations with Vipul and Bill Schmitt were usually less substantive, but always important (I guess). My conversations with Dave Jordan were memorable in a sort of "please don't eavesdrop, we're not making any sense" way. Dave is a talented writer of silly stories. I'll miss our daily bantering on everything from serial killers and horror movies to why if someone today is named Jesus, they're required to pronounce their name HAY-ZOOSE, even if they're not hispanic. Dave's mind is active, playful, and inventive, as well as wanting to marry. Speaking of wanting to marry, I should say more about Vipul and Bill who, along with Dave, have been my closest friends at MIT. I experienced many enjoyable dinners, movies, cultural events, aerobics classes (low impact), and cock fights with one or more of these three. I'd like to wish every good fortune to each of them. To Dave, who may one day write a horror novel; to Bill, who I think wants to become a nurse after his post-doc is completed; and finally to Vipul, who will work as a financial analyst until he saves enough money to accomplish his real dream, to walk/jet-skii around the world.

I hope I haven't neglected to mention anyone. In case I have, if that person could send e-mail to MCILVAIN@MITLNS.MIT.EDU, I will petition the graduate school that I may submit an updated acknowledgements section of this thesis. The same goes for anyone I included who would rather have been left out.